

Dipartimento di Scienza e Alta Tecnologia
UNIVERSITÀ DEGLI STUDI DELL'INSUBRIA

Hawking radiation and mode conversion at optically induced horizons



Eleonora Rubino

Thesis submitted in partial fulfillment of the requirements
for the degree of *Philosophiæ Doctor* in Physics
XXV Ciclo

March 28, 2013

Supervisor: Prof. Daniele Faccio*

*Current position: Heriot-Watt University, Edinburgh (UK)

A mia nonna Fernanda

Imagination is more important than knowledge. For knowledge is limited, whereas imagination embraces the entire world, stimulating progress, giving birth to evolution. It is, strictly speaking, a real factor in scientific research.

Albert Einstein

Acknowledgements

In this work I have reported part of the scientific results I dealt with during my PhD studies. Most of the achievements presented here would not have been reached without the intense and fruitful collaboration among the experimental and theoretical research groups I have had the honor of working with.

I want to thank above all my supervisor, Prof. Daniele Faccio, for his guidance, support and endless enthusiasm. He motivated me through the entire doctoral period and he inspired me with the passion for his work, physics and Science in general. I also want to thank him and his family (Silvia and Cesare) for their hospitality during the period I spent at the Heriot-Watt University of Edinburgh.

I am grateful for having had the opportunity of working with many brilliant scientists from very different research areas. I want to thank each of them for having teaching me so much during the last three years. I wish to thank Prof. Paolo Di Trapani for letting me work in his laser laboratory at the University of Insubria, during the first period of my PhD and for the opportunity to participate to three editions of the STELLA School. I thank Dr. Sergio Cacciatori, Dr. Francesco Belgiorno and Prof. Vittorio Gorini for the patience they have shown in introducing me to the basic concepts of general relativity and theoretical physics. I wish to thank Prof. Arnaud Couairon from École Polytechnique (Paris), Prof. Miroslav Kolesik from the University of Arizona (Tucson), together with my friend and colleague Dr. Antonio Lotti, for the needful numerical support. I want to thank Prof. Ulf Leonhardt, Dr. Friedrich König, and all the people of the crew at the University of St. Andrews.

I thank also Dr. David Townsend for having host me in his laboratory at the Heriot-Watt University.

I am also grateful to Prof. Audrius Dubietis, Prof. Gintaras Valiulis, Prof. Gintaras Tamošauskas, Dr. Julius Darginavičius and Dr. Vytautas Jukna for the time spent at the Vilnius University during many LaserLab Projects. I thank Prof. Stelios Tzortzakis, Prof. Dimitris Papazoglou and the entire UNIS group at the IELS-FORTH research center in Heraklion, Greece. I want to thank also Prof. Jens Biegert from the ICFO institute in Barcelona, Spain, and all the guys of his group.

I wish to thank Prof. Roberto Morandotti for giving me the opportunity to work in his group at the EMT-INRS research center of Montreal, Canada. I thank also all the people of the UOP group and the staff of the ALLS facility. I especially thank Dr. Matteo Clerici and Dr. Lucia Caspani, not only for the experiments we performed together, but also for always being good friends of mine and for welcoming me into their home during my first canadian days. I wish them the happiest time with their child Andrea.

A special thanks goes to all the people here in Como: Marta Pigazzini, Antonio Lotti, Francesco Dalla Piazza, Matteo Bina, Chiara Cappellini and Ottavia Jedrkiewicz. I thank you all for sharing the microwave and for the good moments we spent together.

Finally, I thank my parents and my love Fabio, for their truthful confidence in my abilities. They, more than any other, have encouraged me during these years.

Contents

Introduction	1
1 Ultrashort pulse propagation in isotropic media	5
1.1 Dispersion	5
1.1.1 The Sellmeier dispersion formula	8
1.2 Kerr nonlinearity	11
1.2.1 Self-action effects	13
1.2.2 Plasma effects	14
1.2.3 Cross-phase modulation and Four-Wave mixing	15
1.3 Ultrashort laser pulse filamentation	16
1.3.1 Space-time effects	17
1.3.2 Conical X-waves	20
1.4 Solitons	22
1.4.1 Dispersive waves: phenomenology	24
2 Scattering theory of SC and RR	27
2.1 Akhmediev theory of Resonant Radiation	27
2.1.1 Relation to Cherenkov radiation	29
2.2 First Born approximation	30
2.3 UPPE derivation	32
2.3.1 Numerical model	33
3 Negative frequencies	37
3.1 Negative frequencies in optics and other systems	37

3.1.1	Lab and comoving frame description	40
3.2	The first Born approximation revisited	44
3.3	The Manley-Rowe relation and amplification	47
4	Linear and nonlinear moving inhomogeneity	49
4.1	Toy-model DP	50
4.1.1	Photon number amplification	53
4.1.2	Propagation cross-correlation	53
4.2	Soliton-induced DP	54
4.2.1	Probe scattering from a soliton-induced DP	55
4.3	Two-dimensional scattering numerics	57
4.4	Gain	58
5	Experiments: Negative Resonant Radiation	61
5.1	Creating an effective moving medium with light pulses	61
5.1.1	Soliton in photonic crystal fibers	63
5.1.2	Spontaneous filaments	63
5.1.3	Bessel filament	63
5.2	NRR in bulk calcium fluoride	65
5.2.1	Experimental setup	66
5.2.2	Experimental data and numerics	67
5.2.3	Far-field spectra	70
5.3	NRR in photonic crystal fiber	72
5.4	NRR seeded with THz	73
5.4.1	Experimental setup	74
5.4.2	Experimental results	75
5.4.3	Numerics	77
6	Implications: optical analogue for gravity	81
6.1	Analogue gravity in moving media	82
6.1.1	Dielectric metrics and white hole horizons	85
6.1.2	A comment on the horizon condition	86
6.1.3	Analogue Hawking temperature	90

6.2	Stimulated Hawking emission and amplification	92
6.2.1	Numerical results: thermality	94
6.3	Experiments: analogue Hawking radiation	98
6.3.1	Experimental setup	98
6.3.2	Experimental results	100
6.3.3	“Superluminal” dispersion: numerics	102
7	Conclusions	107
A	Publications and conferences	109
A.1	Publications	109
A.2	Contributions at international conferences	111
	List of Figures	113
	List of Tables	115
	References	117

Introduction

The scattering of electromagnetic radiation is an essential and fundamental tool by which we may study light-matter interaction. In usual conditions, the medium is considered as stationary and scattering is characterized by a change in the wave-vector spectrum of the light beam. The frequency of the beam is not affected. On the other hand, when the medium is *moving* the scattering leaves the light beam wave-vector unaffected and changes its frequency. The basics of scattering from a time-changing boundary were discussed in detail by Mendonça and co-workers (see e.g. [1] and references therein) in terms of a refraction from a “time-boundary”. Examples of “time refraction” have been predicted and observed from a moving plasma front [1, 2, 3] and in waveguide structures [4, 5, 6].

In this thesis we study the scattering from a moving dielectric perturbation (DP) induced through the nonlinear Kerr effect. Light is scattered and resonantly transferred to two output modes identified by distinct frequencies, one *positive* and the other *negative* in the reference frame comoving with the DP. We first describe the process in terms of linear scattering in the first Born approximation, where we predict photon number *amplification* (at the expense of the DP) as arising by the mixing of positive and negative modes. Our predictions have been verified numerically [7] and, only partly, experimentally [8]. This implies that DPs, generated for example by soliton-like pulses in dielectric media, may be used to excite quantum vacuum fluctuations and provides an experimental link to quantum field studies in curved space-times.

The laser pulse induced DP is therefore described, using the tools of transformation optics and general relativity, in terms of a flowing medium which curves the effective space-time metric as seen by the light rays. Figure 1 shows a sketch of the two different visions presented in this thesis. The

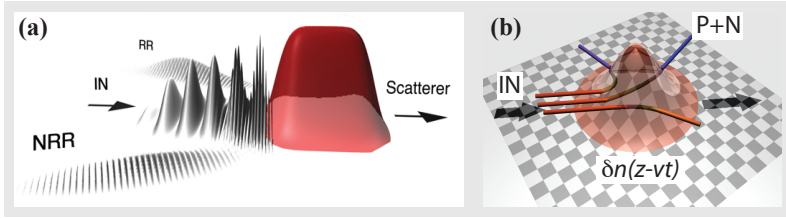


Figure 1: Different visions for the resonant transfer of energy mediated by a moving DP. (a) refers to the *scattering* interpretation in the first Born approximation; while (b) refers to the *analogue gravity* point of view and portrays the curved space-time metric which is actually seen by light rays in the vicinity of an event horizon.

analogue of an *event horizon* associated with the space-time curvature is then predicted to excite spontaneous emission of photons in a process similar to *Hawking radiation* from a gravitational black hole [9, 10, 11, 12, 13].

The thesis is not organized in a chronological order, but rather we decide to present the results from the most recent [7, 8] to the oldest ones [12, 13]. The reason for that is essentially the sake of clarity. The tools we developed during the years allowed us to realize the intimate analogy with the gravitational Hawking-like emission and thus describe it with terms and tools that are more suitable (and understandable) for the nonlinear optics community.

The thesis is organized as follows. Chapter 1 is devoted to a general overview of the ultrashort laser pulse propagation effects in dispersive isotropic media, both in the linear and nonlinear regime. In Chapter 2 we introduce the terminology and the analytical tools which are generally used to describe the resonant radiation as a scattering event. The numerical model adopted in this thesis is also described here. Negative frequencies in optics and other systems are presented in Chapter 3, where we provide a physical interpretation of the existence of the negative resonant radiation (NRR) based on: (i) the comoving frame description of the dispersion relation; (ii) the revisited first Born approximation and (iii) a Manley-Rowe relation generalized to the case of moving perturbations. In Chapter 4 we report on the numerical results of NRR generation and photon number amplification, while in Chapter 5 we present the experimental results of seeded and self-seeded NRR generation in Kerr media. Finally, in Chapter 6 we describe the optical analogue for gravity and we reinterpret the

previous results with the tools of transformation optics and general relativity. In Chapter 6 we also derive the thermality for the stimulated Hawking emission and we present experimental evidences of spontaneous emission of photons from ultrashort laser pulse filamentation in Kerr media, that are in quantitative agreement with the Hawking model. Chapter 7 is devoted to the conclusions.

Chapter 1

Ultrashort pulse propagation in isotropic media

In this Chapter we shall introduce the role of dispersion in linear and non-linear propagation of ultrashort laser pulses in isotropic dielectric media. In particular we shall describe the main features characterizing propagation of intense ultrashort pulses in presence of a third-order Kerr nonlinearity. We will give a brief overview of phenomena such as supercontinuum generation, soliton and dispersive-wave regime in optical fibers. We will also describe some space-time effects allowing the formation of filaments and conical X-waves in bulk Kerr media.

1.1 Dispersion

All optical materials own the fundamental property of dispersion, which manifests itself as a dependence of the *phase* velocity of a wave on its frequency, or wavelength. Optical dispersion is also called *chromatic* dispersion to emphasize its wavelength-dependent nature. For example, it is responsible for separation of colors in a prism, or for the formation of rainbows.

For transparent dielectric media, the wave phase velocity, v_ϕ , is simply defined as the ratio between the velocity of light in vacuum, $c = 299792458$

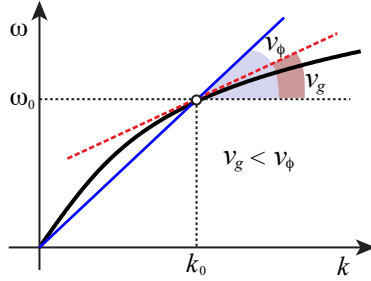


Figure 1.1: Schematic representation of phase, $v_\phi = \omega/k$, and group velocity, $v_g = (dk/d\omega)^{-1}$, at $\omega = \omega_0$, in the normal dispersion region of a transparent dielectric medium.

m/s, and the refractive index of the material, n ,

$$v_\phi = \frac{c}{n}. \quad (1.1)$$

For light pulses, the velocity at which energy, or information, is conveyed along the wave is the *group* velocity, defined as,

$$v_g = 1/k'(\omega) = \left(\frac{dk}{d\omega} \right)^{-1}, \quad (1.2)$$

where $k(\omega) = \omega n(\omega)/c$ is the modulus of the wavevector at frequency ω ; the corresponding wavelength (in vacuum) is $\lambda = 2\pi c/\omega$. Evaluating Eq. (1.2), we obtain,

$$k'(\omega) = \frac{dk}{d\omega} = \frac{1}{c} \left[n(\omega) + \omega \frac{dn}{d\omega} \right], \quad (1.3)$$

and thus [14],

$$v_g = \frac{c}{n_g}, \quad \text{with} \quad n_g(\omega) = n(\omega) + \omega \frac{dn}{d\omega}. \quad (1.4)$$

As we see, the group refractive index, n_g , depends itself on frequency via the relation (1.4). Figure 1.1 shows the schematic relationship between the phase and the group velocity, evaluated at the same frequency, ω_0 , in an ordinary transparent medium. The phase velocity, $v_\phi(\omega_0) = \omega_0/k_0$, measures the propagation speed of the single plane-wave component of the pulse in the medium; where $k_0 = k(\omega_0)$. This plane-wave component does not carry any information, because of its infinite duration. On the other hand, the group velocity, $v_g(\omega_0) = (d\omega/dk)_{\omega_0}$, is the slope of the

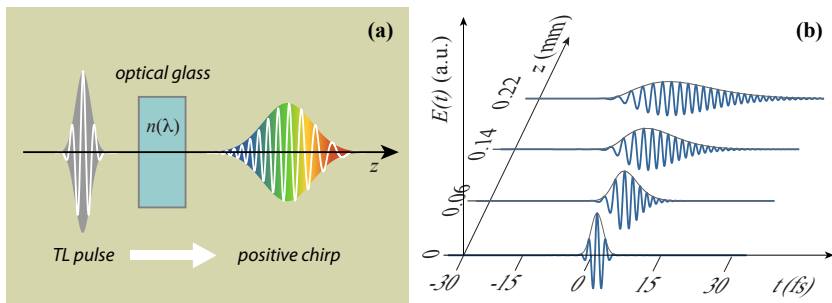


Figure 1.2: Optical pulse dispersion: cartoon (a) and numerical simulation (b) of linear propagation in $\sim 250 \mu\text{m}$ of fused silica glass. Input pulse carrier wavelength at 600 nm and input pulse duration 2 fs.

line tangential to the dispersion curve at $\omega = \omega_0$, and is the rate at which changes in pulse amplitude (known as the *envelope*) will propagate. In ordinary matter, $v_g < v_\phi$ (normal dispersion).

Due to the dependence of the group velocity on frequency, a short pulse, because of its wide spectral width, undergoes a phase distortion inducing an increase of its duration as it propagates through the material [15, 16]. The parameter which measures this frequency-dependent variation of the group velocity is the second order derivative of the propagation factor,

$$k''(\omega) = \frac{d^2k}{d\omega^2} = \frac{d}{d\omega} \left(\frac{1}{v_g} \right) = \frac{\lambda^3}{2\pi c^2} \frac{d^2n}{d\lambda^2}. \quad (1.5)$$

This term is called *group velocity dispersion* (GVD) and is responsible for progressive *chirp* of optical pulses during propagation. This means that the instantaneous frequency, $\omega(t)$, defined as the time derivative of the phase φ acquired by the pulse in propagation, $\varphi(\omega, z) = k(\omega)z$, varies linearly with time, i.e.,

$$\omega(t) = \frac{\partial\varphi}{\partial t} = \omega_0 + \alpha t, \quad (1.6)$$

where α is a real parameter, function of the input pulse duration, propagation distance and $k_0'' = k''(\omega_0)$. For example, an initially *transform limited* pulse in the *normal* GVD spectral region ($k_0'' > 0$), acquires in propagation a *positive* chirp, where lower frequencies (red) concentrate in the leading part while higher frequencies (blue) concentrate in the trailing part of the pulse. As a consequence, the pulse envelope is distorted during propagation and undergoes a duration broadening. For a Gaussian pulse, with input

pulse duration τ_p , the pulse duration at propagation distance z reads [16]:

$$\tau(z) = \tau_p \sqrt{1 + \left(\frac{2k_0''z}{\tau_p^2} \right)^2}. \quad (1.7)$$

Figure 1.2 shows the numerically evaluated behavior of an ultrashort Gaussian pulse (input pulse duration $\tau_p = 2$ fs, centered at 600 nm) propagating in a linear, dispersive medium. After propagation over ~ 250 μm of common fused silica glass, the pulse spreading in time is evident, as well as the growth of a positive frequency chirp.

For completeness, we define also the *group delay dispersion* (GDD) of an optical element, which is the second derivative, with respect to the angular frequency, of the change in the spectral phase:

$$\text{GDD} = \frac{\partial^2 \varphi}{\partial \omega^2}. \quad (1.8)$$

It always refers to some optical element or to some given length of a medium (e.g. an optical fiber) and is measured in fs^2 or ps^2 . Positive (negative) values correspond to normal (anomalous) GVD, which is the GDD per unit length (in units of s^2/m).

1.1.1 The Sellmeier dispersion formula

Before moving to the nonlinear propagation effects, it is worth spending few words to introduce the Sellmeier dispersion relation. This is an empirical relation for the refractive index $n = n(\lambda)$ of a material, derived by Sellmeier in 1871, that relies on the classical Lorentz model¹ and provides a very good approach for estimating the optical behavior of insulators (or dielectrics).

The Lorentz Oscillator theory describes the polarization of dielectrics as arising from the motion of simple harmonic oscillators and this is based on the fact that the potential energy of an electron at the bottom of the potential well (in equilibrium) may be approximated by a quadratic function which simplifies to the simple harmonic oscillator function. The refractive index of a dielectric is thus expressed, combining the Clausius-Mosotti and Lorentz equations, as a summation of the contributions of j -oscillators of

¹The problem may also be treated quantum-mechanically [15].

strength f_j and damping constant γ_j , related to the resonance ω_j , of any atom/molecule of the medium (see, e.g., [15] for a complete treatment):

$$\frac{n^2 - 1}{n^2 + 2} = \frac{4\pi N e^2}{3\epsilon_0 m_e} \sum_j \frac{f_j}{\omega_j^2 - \omega^2 + i\gamma_j \omega},$$

where N is the number of molecules per unit volume, ϵ_0 the vacuum permittivity, e and m_e the electron charge and mass, respectively. Colorless, transparent media have their characteristic resonances outside the visible spectrum: the electronic polarization frequencies are in the UV, where they induce a strong *absorption* (related to the imaginary part of the refractive index), while the molecular polarization frequencies lie in the infrared spectral region. In between, the refractive index has a weak frequency dependence, decreasing with increasing wavelength (normal chromatic dispersion).

Far from resonances, the refractive index is well described by the Sellmeier relation, i.e. an expansion of $n(\lambda)$ in the form of a series of single-dipole oscillator terms each of which has the usual $\lambda^2/(\lambda^2 - \lambda_j^2)$ dependence as in [17],

$$n(\lambda)^2 = 1 + \frac{A_1 \lambda^2}{\lambda^2 - \lambda_1^2} + \frac{A_2 \lambda^2}{\lambda^2 - \lambda_2^2} + \frac{A_3 \lambda^2}{\lambda^2 - \lambda_3^2} + \dots, \quad (1.9)$$

where λ_i and A_i are called Sellmeier coefficients, which are determined by fitting this expression to the experimental data. The λ_i are the *effective resonance wavelengths* corresponding to the centre of gravity of the absorption band in the relevant spectral range. It can be shown that all dispersion curves of optical glasses may be expressed by using two effective resonance wavelengths in the UV (e.g between 50 and 150 nm) and one in the IR spectral region (typically from 7 to 10 μm).

In Table 1.1 we report the Sellmeier coefficients for three optical materials (i.e., fused silica [18], calcium fluoride [19] and diamond [20]) used for

Materials	A_1	A_2	A_3	λ_1 (μm)	λ_2 (μm)	λ_3 (μm)
SiO ₂	0.6961663	0.4079426	0.8974794	0.0684043	0.1162414	9.896161
CaF ₂	0.5675888	0.4710914	3.8484723	0.050263605	0.1003909	34.649040
Diamond	4.3356	0.3306		0.1060	0.1750	

Table 1.1: Sellmeier coefficients for various materials adopted for the experimental and numerical results of this thesis. Refs. [18, 19, 20].

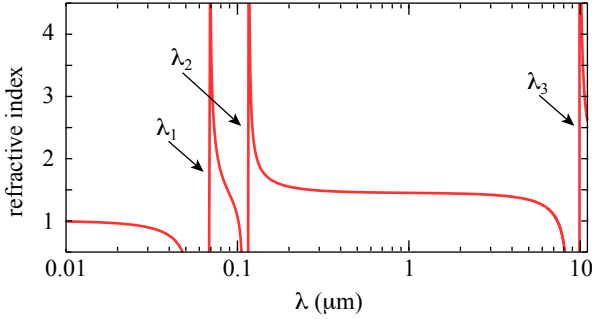


Figure 1.3: Sellmeier dispersion curve for SiO_2 (silica) glass, according to the Sellmeier coefficients of Table 1.1.

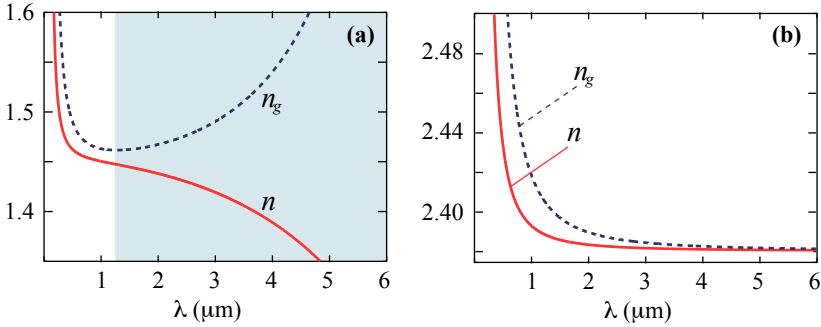


Figure 1.4: Refractive index, n (solid red) and group index, n_g (dashed blue) for SiO_2 (silica) glass (a) and diamond (b), over the $0.2 \div 6 \mu\text{m}$ wavelength range. The shaded area in (a) indicates the *anomalous* GVD region for fused silica ($k'' < 0$).

the experimental and numerical results presented in this thesis. The Sellmeier dispersion curve, $n(\lambda)$, for fused silica is also shown in Figure 1.3 in the spectral range between 10 nm and 11 μm , with highlighted the position of the three effective resonance wavelengths, $\lambda_1, \lambda_2, \lambda_3$. Finally, in Figure 1.4 we compare the dispersion curves for fused silica (a) and diamond (b), over the spectral region $0.2 \div 6 \mu\text{m}$, which is free of resonances. In both Figs. 1.4(a)-(b) the refractive index, n (solid red curve), is over-imposed to the group index, n_g (dashed blue curve), evaluated from relation (1.4). We immediately note that, while in diamond (which, according to Table 1.1, is transparent from the ultraviolet region to less than one THz) the GVD is always normal ($k''_0 > 0$); in fused silica the GVD parameter k''_0 is positive for visible light, but becomes negative for wavelength longer than approximately 1.3 μm [shaded area in Fig. 1.4(a)]. This fact makes a huge

difference in the interplay between linear and nonlinear effects suffered by ultrashort optical pulses propagating in the two media. In particular, as we will see in Section 1.4, the anomalous GVD region is a primary ingredient for the formation of optical solitons in Kerr media.

1.2 Kerr nonlinearity

When the intensity of the light pulse is high enough, it is no longer possible to consider the polarization of the medium as linearly proportional to the electric field and nonlinear effects should be taken into account. In isotropic media, such as a liquid or amorphous solid, the propagation of high intensity laser pulses induces a local variation of the refractive index which depends on the laser pulse intensity and which is at the basis of many *third-order*, $\chi^{(3)}$, phenomena: e.g. self- and cross-phase modulation, self-focusing, self-steepening, supercontinuum generation and conical emission.

In this Section we shall describe the origin of these effects, starting to consider the general equation for the electric field \mathbf{E} in a dielectric medium:

$$\nabla \times (\nabla \times \mathbf{E}) + \mu_0 \frac{\partial^2 \mathbf{P}}{\partial t^2} + \frac{1}{c^2} \frac{\partial^2 \mathbf{E}}{\partial t^2} = 0, \quad (1.10)$$

where μ_0 is the permeability of free space and \mathbf{P} is the polarization density. Using $\nabla \times (\nabla \times \mathbf{E}) \simeq -\nabla^2 \mathbf{E}$, we obtain,

$$\nabla^2 \mathbf{E} - \frac{1}{c^2} \frac{\partial^2 \mathbf{E}}{\partial t^2} = \mu_0 \frac{\partial^2 \mathbf{P}}{\partial t^2}, \quad (1.11)$$

where the Laplacian operator $\nabla^2 = \partial_{zz}^2 + \nabla_{\perp}^2$, being $\nabla_{\perp}^2 = \partial_{xx}^2 + \partial_{yy}^2$. We now write the material polarization response, excited by a sufficiently intense laser pulse propagating in an isotropic medium (i.e., $\chi^{(2)} = 0$ for symmetry constraints), as [21]:

$$\mathbf{P} = \epsilon_0 \left(\chi^{(1)} \mathbf{E} + \chi^{(3)} \mathbf{E} \mathbf{E} \mathbf{E} \right), \quad (1.12)$$

where ϵ_0 is the vacuum permittivity, $\chi^{(1)}$ is the linear susceptibility that is related to the (background) linear refractive index $n_0 = \sqrt{1 + \chi^{(1)}}$, and $\chi^{(3)}$ is the third-order nonlinear susceptibility (also known as the Kerr nonlinearity). In a scalar theory, we can write the linearly polarized electric

Materials	Wavelength (nm)	n_2 (cm ² /W)	Ref.
SiO ₂	1064	3.2×10^{-16}	[22, 23]
CaF ₂	1064	2.0×10^{-16}	[24, 23]
Diamond	545	12.6×10^{-16}	[25, 23]

Table 1.2: Nonlinear Kerr coefficient, n_2 , for various materials adopted for the experimental and numerical results of this thesis.

field as $E = \frac{1}{2}A \exp[i(kz - \omega t)] + c.c.$, and the third-order nonlinear polarization term $P_{\text{NL}} = \epsilon_0 \chi^{(3)} E^3$, becomes:

$$P_{\text{NL}} = \epsilon_0 \frac{\chi^{(3)}}{8} \left[A^3 e^{i(3kz - 3\omega t)} + 3|A|^2 A e^{i(kz - \omega t)} + c.c. \right]. \quad (1.13)$$

The first term oscillates at 3ω , which means that it acts as a source for *third harmonic generation*, and in general it may be neglected (unless the beam or the medium are specifically engineered so as to enhance this process). The second term oscillates at the input frequency ω and may be interpreted as an effective linear polarization term in which the refractive index is proportional to the intensity of the electric field $I = |A|^2/2$ (measured in W/cm²). This effect is called *Kerr effect* and is usually written, introducing an effective refractive index, as:

$$n = n_0 + n_2 I, \quad (1.14)$$

where n_2 is the nonlinear Kerr coefficient and I , in the most general case, has a spatio-temporal distribution $I = I(r, t)$. From Eq. (1.13) we have,

$$n = \sqrt{1 + \chi^{(1)} + \frac{3}{8} \chi^{(3)} |A|^2} = n_0 \sqrt{1 + \frac{3}{8} \frac{\chi^{(3)} |A|^2}{n_0^2}} \simeq n_0 + \frac{3\chi^{(3)} |A|^2}{16n_0}, \quad (1.15)$$

and by comparison of Eq. (1.15) with (1.14), we obtain an expression for the nonlinear index,

$$n_2 = \frac{3\chi^{(3)}}{8n_0}, \quad (1.16)$$

which depends on the specific medium. In Table 1.2 are reported the nonlinear Kerr coefficients (measured in units of cm²/W) for the materials used for the experimental and numerical results of this thesis.

We note that the intensity profile of a laser pulse usually has a Gaussian-like form, i.e. $I = I(z - vt) = \exp[-(z - vt)/\sigma]^2$, where the pulse speed is given by the group velocity of light in the medium, $v = v_g$. In other words,

in virtue of the almost *instantaneous* response of the Kerr nonlinearity, an intense laser pulse propagating in a nonlinear Kerr medium will create a *dielectric perturbation* (DP) of the refractive index,

$$\delta n(z - vt) = n_2 I(z - vt), \quad (1.17)$$

that travels with exactly the same features, e.g. speed and amplitude evolution, of the pump laser pulse.

This Kerr-induced moving perturbation (which *travels close to the speed of light*) is one of the principal actors of this thesis work and is responsible for all the phenomena presented in the next chapters. For the moment, we put aside the surprising implications related to the existence of a “relativistically” moving DP, to describe in more detail the state-of-the-art of the self-action effects in Kerr media.

1.2.1 Self-action effects

The intensity-dependent variation of n occurs in a very short time (of the order of the electronic cloud response time $\sim 10^{-16}$ s), so the response of the Kerr nonlinearity is, to all extents, instantaneous over the time scale of the input pulse duration (typically tens, or hundreds, of femtoseconds). Light itself is affected by this local modification of the refractive index, in the form of a self-modulation of the temporal, or spatial phase.

A plane wave traveling along the z axis for a length L suffers a phase variation:

$$\delta\varphi = \delta\varphi_0 + \frac{\omega_0}{c} n_2 I L, \quad (1.18)$$

where $\delta\varphi_0$ is the phase variation in the absence of nonlinear effects. The third-order nonlinearity thus induces a phase delay proportional to the instantaneous intensity of the wave, which determines the phenomena of *self-phase modulation* and *self-focusing*.

Self-phase modulation

In the case of a light pulse centered at frequency ω_0 , it is possible to consider the instantaneous frequency along the pulse as the first derivative of the phase $\delta\varphi(t)$ with respect to time. For a propagation along a distance L the

instantaneous frequency in the presence of the Kerr nonlinearity is given by:

$$\omega_{ist} = \frac{\partial}{\partial t}(\omega_0 t - \delta\varphi) = \omega_0 + n_2 L \frac{\omega_0}{c} \frac{\partial I(r, t)}{\partial t}. \quad (1.19)$$

Since the intensity of a light pulse has a temporal profile, Eq. (1.19) determines the generation of new frequencies: this process is called self-phase modulation (SPM). In particular, since n_2 is usually positive, the leading edge ($\partial_t I > 0$) generates lower frequencies, while higher frequencies are generated in the trailing part of the pulse.

Self-focusing

If one considers a Gaussian transverse intensity profile in Eq. (1.14), the refractive index in the center of the beam, where the intensity is higher, is greater than the index seen by the tails of the beam: the material acts as a focusing lens. This spatial self-phase modulation leads to so-called self-focusing for $n_2 > 0$ and self-defocusing for $n_2 < 0$. An intense collimated beam traveling through a Kerr medium starts to contract because of self-focusing; this determines an increase of the peak intensity and the effect becomes stronger and stronger (the focal length of the “effective” lens becomes smaller).

In real experiments, the collapse of the beam is avoided by the onset of defocusing effects, originating by saturation mechanisms, which lower the total energy (and therefore limit the intensity) of the beam and/or defocus the beam itself.

1.2.2 Plasma effects

Nonlinear Kerr-induced phase distortions lead to frequency broadening and self-focusing. These are “cumulative” effects in the sense that they require propagation (i.e., dispersion and diffraction) in order for the Kerr-induced phase-distortions to accumulate and thus dramatically modify the pulse and beam profile. Alongside nonlinear propagation effects on the pulse, important modifications occur also within the medium itself, namely *plasma generation* via *multi-photon ionization*. Close to the collapse point the intensity of the pulse becomes high enough to trigger ionization of the medium by means of nonlinear (*multi-photon*) absorption. The plasma of free electrons generated by the high intensity peak contributes to the arrest of the

collapse by two main processes: (i) it locally reduces the refractive index; and (ii) it can be further accelerated by means of an inverse Bremsstrahlung effect, thus lowering the intensity.

The sum of all these linear (dispersion and diffraction) and nonlinear (Kerr-induced self-phase modulation and self-focusing, multiphoton absorption and ionization) effects can lead to a dramatic reshaping of the laser beam itself that may either breakup under the effect of the modulation instability or form a *filament* [26]. In Section 1.3 we shall describe the complicated spatio-temporal dynamics of ultrashort laser pulse filamentation, also with the help of numerical simulations based on the solution of the extended nonlinear Schrödinger equation [26].

1.2.3 Cross-phase modulation and Four-Wave mixing

Until now we have considered only the self-action effects of the Kerr nonlinearity, i.e., the effects that the nonlinearity has on a single input pulse. Nevertheless, in the presence of fields at different frequencies, the Kerr nonlinearity can lead also to a strong interaction resulting in strong inter-pulse phase effects and frequency conversion. The former is referred to as *cross-phase modulation* (XPM) and the latter as *four-wave mixing* (FWM).

The XPM refers to the nonlinear interaction between a strong pump field E_p , that excites the nonlinearity, and a weaker seed field E_s , oscillating at frequency ω_p and ω_s , respectively. In this case, the total electric field becomes, $E = \frac{1}{2} \{A_p \exp [i(k_p z - \omega_p t)] + A_s \exp [i(k_s z - \omega_s t)] + c.c.\}$. By substituting this relation into the relation for the nonlinear polarization (1.12) and retaining only the terms oscillating at frequency ω_s , we obtain,

$$P_{\text{NL}} \propto \chi^{(3)} (A_s^2 + 2A_p^2) E_s. \quad (1.20)$$

The first term describes the SPM of the seed and may thus be neglected, being the seed indeed weak; the second term describes the XPM induced upon the weak seed wave by the intense pump wave. The strong pump of peak intensity I_p , thus induces a change in the refractive index for the weaker seed pulse which is twice as large as that self-induced Kerr effect of Eq. (1.17), i.e.,

$$\delta n = 2n_2 I_p. \quad (1.21)$$

Under similar working conditions as for XPM, it is also possible to observe generation of new frequencies and parametric amplification. These processes fall within the so called FWM, in which the Kerr nonlinearity mixes energy between four different fields. FWM is commonly described within a context in which the interacting waves are treated as plane waves of frequency ω_j and wave vectors $k_j = \omega_j n(\omega_j)/c$. The total electric field reads:

$$E = \frac{1}{2} \sum_{j=1}^4 A_j \exp [i(k_j z - \omega_j t)] + c.c., \quad (1.22)$$

and the total nonlinear polarization (1.13) will also be composed of four terms. In order to have efficient transfer of energy among different fields, the four waves involved must obey to strict energy and momentum constraints, namely they should satisfy the so-called frequency-matching ($\Delta\omega = 0$) and phase-matching ($\Delta k = 0$) relations [21]. For example, the phase-matching condition below,

$$\begin{aligned} \Delta\omega &= 2\omega_1 - \omega_3 - \omega_4 = 0 \\ \Delta k &= 2k_1 - k_3 - k_4 = 0, \end{aligned}$$

refers to a degenerate (same frequency, $\omega_2 = \omega_1$) FWM interaction, in which a strong input pump at frequency ω_1 generates two new difference frequency fields, at frequencies ω_3 and ω_4 .

1.3 Ultrashort laser pulse filamentation

Ultrashort laser pulse filamentation refers to the spontaneous formation of a *dynamic* optical pulse structure with an intense core that is able to propagate over extended distances, much larger than the typical diffraction length (Rayleigh range), while keeping a narrow beam size without the help of any external guiding mechanism [26].

The underlying mechanism for the formation of a spontaneous filament is the interaction between the intense laser pulse and the medium Kerr nonlinearity which induces a reshaping of the pulse along both the transverse (x, y) and longitudinal (z) coordinates. In the transverse plane, the input pulse will start to shrink under the so-called self-focusing effect and in the longitudinal coordinate self-phase-modulation and dispersion will

create new frequencies and distort the pulse. These effects occur concomitantly and the input pulse focuses to a so-called *nonlinear focus* point at which the highest intensity is reached. This intensity is typically “clamped” to a maximum value that depends mainly on the material properties (e.g. dispersion, nonlinear absorption and ionization) and will vary only slightly with the laser pulse input energy. After the nonlinear focus, a filament will emerge, i.e. in the transverse plane a tightly focused intensity spike ($\sim \text{TW}/\text{cm}^2$ in condensed media) is observed that propagates apparently without diffraction over long distances. This intensity is surrounded by a much weaker photon reservoir which co-propagates with the intensity spike and continues to refuel it [26].

1.3.1 Space-time effects

It is important to note that the interplay of the various linear (dispersion and diffraction) and nonlinear (self-phase modulation, self-steepening, multiphoton absorption and ionization, plasma creation) effects lead to very complicated dynamics that may be collectively described only qualitatively by analytical models. A quantitative prediction of the full spontaneous filament evolution relies on numerical simulations. These are usually based on the numerical solution of the extended nonlinear Schrödinger equation (NLSE) [26]. This equation is used also in this work to model filament propagation and gives, as an example, the results shown in Figures 1.5 and 1.6.

Pulse-splitting

After the nonlinear focus, the intensity of the central spike will typically start to decay, concomitantly with the formation of two split *daughter pulses*, one travelling faster and the other slower with respect to the input laser pulse. Figure 1.5(a) shows the pulse evolution in fused silica at $x = y = 0$ (i.e. at the pulse centre in the transverse dimensions) along the comoving longitudinal coordinate $\tau = t - z/v$, where v is the input Gaussian pulse group velocity v_g . The evolution is shown just after the nonlinear focus as the pulse clearly splits into two daughter pulses with the trailing (leading) pulse travelling slower (faster) than the input pulse. Moreover, the *self-compression* of the longitudinal dimension of each of these pulses is also evident: for example, the trailing pulse reaches a pulse duration of few

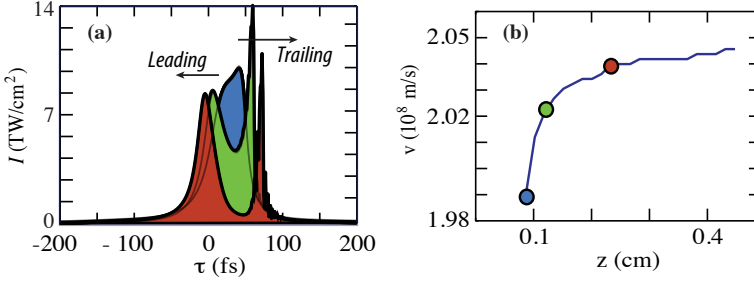


Figure 1.5: Pulse-splitting and self-steepening. (a) Numerically calculated temporal profile of the filament: close to the nonlinear focus the pulse splits into a faster, *leading* and a slower, *trailing* pulse. (b) Variation of the trailing peak velocity with propagation distance.

fs (starting from an input pulse duration of ~ 1 ps). Fig. 1.5(b) shows in more detail the evolution along propagation of the velocity v of the trailing daughter pulse: the colored points (blue, green and red) indicate the propagation distances at which the longitudinal profiles are sampled and shown in Fig. 1.5(a) (with the same colors). As can be seen, the pulse velocity at the nonlinear focus is significantly lower than $v_g \sim 2.05 \times 10^8$ m/s (in fused silica) and accelerates during propagation, asymptotically reaching v_g . This behavior is qualitatively reproduced in all spontaneous filaments and the details, e.g. the precise values of the pulse velocities, depend on the specific experimental settings and mainly on input wavelength, input pulse duration and on the Kerr medium.

Self-steepening

The process of self-steepening occurs because of the intensity-dependent refractive index: the velocity of the intensity peak of the pulse is smaller than the velocity of the wings. This causes a steep edge in the trailing edge because the back part of the pulse catches up the peak [27]; a *shock front* is formed in correspondence of this edge, which is responsible, in the Fourier temporal spectrum, of the generation of higher (blue) frequencies. Fig. 1.6 shows the details of the trailing daughter pulse. The white dashed line highlights the trailing edge of the pulse where a steep shock front forms and which clearly shows a relatively flat profile that does not vary significantly along the transverse coordinate ρ . The weaker features at longer delay times are ripples resulting from the formation of the shock

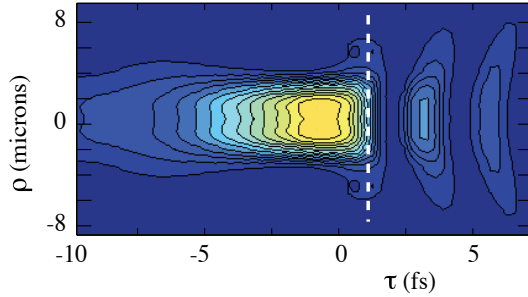


Figure 1.6: Near field intensity profile of the filament after the nonlinear focus. The trailing daughter pulse develops a steep shock front, highlighted by the vertical dashed white line.

front.

The input parameters used for the simulation in Figures 1.5 and 1.6 were chosen to reproduce those of the experiments presented in Chapter 6, i.e. 1 ps pulse duration, 1055 nm laser wavelength, 0.3 mJ input energy and $w_0 = 0.5$ mm input width at $1/e^2$. The pulse was loosely focused with a 20 cm focal length lens into a 2 cm long sample of fused silica. These input conditions lead to the pulse shapes shown in Fig. 1.5(a). The transverse profile in Fig. 1.6 is characterized by a localized central peak that has a diameter of $\sim 5 \mu\text{m}$.

Supercontinuum and Conical Emission

Filamentation is accompanied by a strong broadening of the initial spectrum of the pulse, called *super-continuum*. In particular, with the term “supercontinuum generation” we indicate the generation of an extremely broadband (it may span more than 1 octave), coherent emission with a low angular divergence. Nevertheless, the white light beam generated during filamentation generally does not consist only of a white central (axial) core, but is surrounded by a structure of colored rings (see Fig. 1.7). This second phenomenon is called *conical emission* (CE) and is commonly accepted to arise from the interplay of diffraction, dispersion, and nonlinear response. The emission angle increases with the frequency shift with respect to the pump frequency. Usually, in filamentation in gases, higher frequencies are observed in the external rings of this structure, while redder frequencies constitute the internal rings. The phenomenon of CE depicts a strong space-time coupling dynamics during the process of filamentation

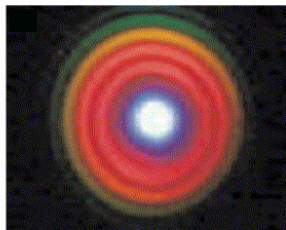


Figure 1.7: Supercontinuum (central white spot) and conical emission measured at 25 m from a 5 mJ, 45 fs, 800 nm laser pulse. Image from Ref. [28].

because every new generated frequency corresponds to a specific angle of emission, i.e. $\theta = \theta(\lambda)$, an effect known as *angular dispersion*.

Several mechanisms have been proposed to explain this phenomenon: Cerenkov radiation [29], self-phase modulation, four-wave mixing [30] and X-waves [31, 32, 33, 34], which we shall introduce in the next Section 1.3.2.

1.3.2 Conical X-waves

Filament dynamics in condensed media with *normal* group velocity dispersion ($k'' > 0$) may be well understood in terms of spontaneous formation and successive interaction of nonlinear X-waves [33, 34]. X-waves, or more generically, conical waves, are particular solutions of the propagation equation with the notable feature of being *stationary*, i.e. non-dispersive and non-diffractive, in both the *(i)*-linear (low intensity) [35, 36] and *(ii)*-nonlinear (high intensity) [31] regimes.

(i)- In the linear regime, to counteract material (intrinsic) GVD, one can exploit the angular dispersion (i.e., the dependence of propagation angle on frequency). The prototype of such conical wave packet (CWP) is indeed the linear X-wave [37, 38]: a non-monochromatic, yet nondispersive, superposition of non-diffracting cylindrically symmetric Bessel -“Durnin”- beams [39], with different colors propagating at different angles, i.e. $\theta = \theta(\lambda)$. Importantly, in the case of wave packets with relatively narrow spectral content, both temporally and spatially, X-waves requires *normally* dispersive media ($k'' > 0$). X-waves show an intense central peak surrounded by an energy reservoir storing the major amount of their energy. This wave packet exhibits a biconical structure (or an “X” structure, if only one spatial dimension is considered) both in the near field (r, t) and in the far field

(k, ω) . In the case of conical X-waves the relation between angles of propagation and frequencies induces an *effective dispersion* which compensates for the dispersion of the medium. The non-dispersive behavior of polychromatic conical waves is described by imposing a linear dependence of the longitudinal component of the wave-vector, k_z , on the angular frequency ω , thus ensuring a constant group velocity in the z direction. In the reference system centered around the pulse carrier frequency ω_0 , the conical wave dispersion relation may be written as,

$$k_{\perp} = \sqrt{k^2 - k_z^2} \quad \text{with} \quad k_z(\omega) = \beta + \frac{\omega - \omega_0}{v} \quad (1.23)$$

and thus the ‘‘X-wave relation’’ reads:

$$k_{\perp}(\omega)^2 = k^2(\omega) - \left(\beta + \frac{\omega - \omega_0}{v} \right)^2, \quad (1.24)$$

with $v = 1/k'_0$ the group velocity of the X-wave and β the longitudinal wavevector, linked to the angular aperture θ_0 of the beam at the carrier frequency ω_0 , as $\beta = k_0 \cos \theta_0$.

(ii)- The spontaneous formation of X-waves in the presence of nonlinearity was first demonstrated in a second-order nonlinear crystal [31] and afterwards in Kerr media [33, 34, 40]. The concept of X-waves was then used to explain the properties of the propagation of laser pulse filaments in transparent media. The interpretation is that, regardless the way of its formation, the evolution of the filament is governed by the interactions of one or more stationary non-diffractive and non-dispersive spatio-temporal profiles in the form of CWPs, so that the central high intensity core is the result of an interference effect, continuously refilled by the surrounding low-intensity energy reservoir. Kolesik et al. demonstrated by means of numerical simulations [33] that filamentation in condensed media may be interpreted as a dynamical interaction of these spontaneous nonlinear X-waves.

The X-wave model therefore considers these non-diffractive and non-dispersive solutions as attractors for the filamentation process and the filament itself may be interpreted and effectively described as an X-wave, justifying most of the properties of the filamentation regime common to CWPs. Each of the daughter peaks generated during the filamentation regime is then regarded as corresponding to an effective X-wave solution. In particular, these X-wave profiles related to the leading and the trailing

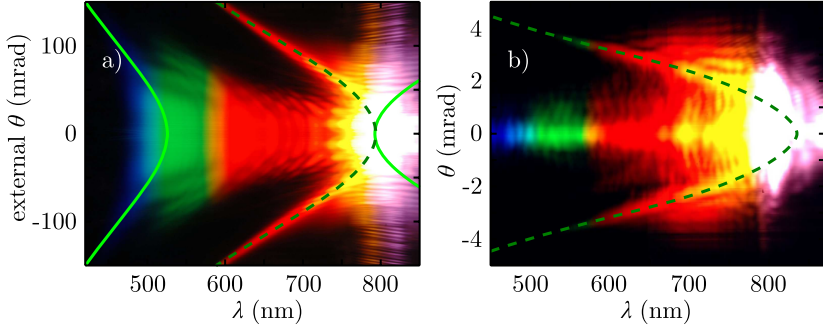


Figure 1.8: Farfield (θ, λ) spectra from filamentation regimes of 800 nm laser pulses in (a) sapphire and (b) air. Superimposed to the spectra, best fitting curves with the X-wave relation (1.24), for $v < v_g$ (solid curve) and $v > v_g$ (dashed curves). Courtesy of A. Lotti [41].

peak exhibit an envelope velocity larger and smaller than the group velocity of the initial Gaussian pulse, respectively. This interpretation is supported by experimental spectra and numerical simulations. Typical experimental filamentation angular spectra (θ, λ) are shown in Figure 1.8, with the corresponding fit with the X-wave spectral relation, Eq. (1.24), for the cases: (a) filamentation in sapphire (external angles, measured in air) and (b) filamentation in air. In both cases the initial laser pulse was centered at 800 nm. In Fig. 1.8(a) two curves are visible: one corresponding to the X-wave with envelope velocity $v < v_g$ (trailing pulse, solid curve) and one with velocity $v > v_g$ (leading pulse, dashed curve). In Fig. 1.8(b) only the curve with $v > v_g$ is visible.

1.4 Solitons

In much the same way that X-waves form spontaneously in (bulk) Kerr media, at high enough powers, solitons may form spontaneously in a fiber. Under certain circumstances, the effects of Kerr nonlinearity and dispersion can exactly cancel each other, apart from a constant phase delay per unit propagation distance, so that the temporal and spectral shape of the pulses is preserved even over long propagation distances. The stationary 3-dimensional X-wave is thus replaced by the stationary 1-dimensional fiber soliton [42, 43, 44]. In strong contrast with nonlinear X-waves, the basic condition for (fundamental) soliton pulse propagation in a lossless medium is the *anomalous* ($k'' < 0$) GVD, for a positive value of the nonlinear Kerr

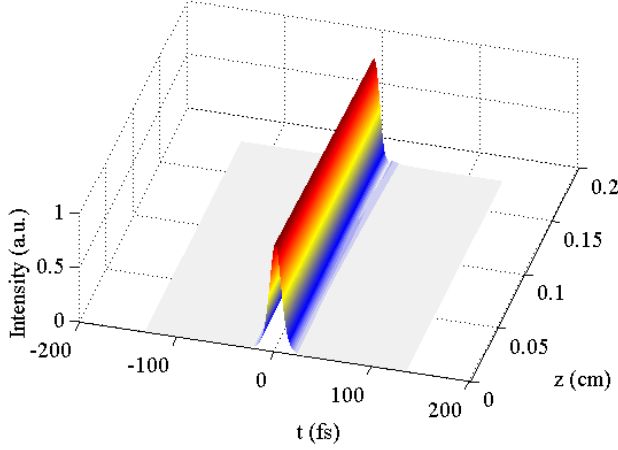


Figure 1.9: Numerics: 1D propagation of a sech^2 -soliton.

coefficient n_2 (as occur for most media). Moreover, the temporal shape of the pulse has to be that of a Fourier transform limited sech^2 -pulse (assuming that the group delay dispersion is constant, i.e. there is no higher-order dispersion). We may appreciate this, considering the equation that describes the propagation of optical pulses through the dispersive nonlinear optical medium, which in this case is the 1-dimensional NLSE [21]:

$$\frac{\partial A_S}{\partial z} + i \frac{k_0''}{2} \frac{\partial^2 A_S}{\partial \tau^2} = i\gamma |A_S|^2 A_S, \quad (1.25)$$

where $\tau = t - z/v_g$ is the retarded time and the term on the right-hand side is the nonlinear Kerr contribution to the propagation constant, i.e.,

$$\Delta k_{\text{NL}} = n_2 \frac{\omega_0}{c} I = 2n_0 \epsilon_0 n_2 \omega_0 |A_S|^2 := \gamma |A_S|^2. \quad (1.26)$$

Equation (1.25) is solved identically by a pulse whose amplitude is of the form:

$$A_S(z, \tau) = A_S^0 \text{sech}(\tau/\tau_0) e^{ik_{\text{sol}}z}, \quad (1.27)$$

where τ_0 is the soliton pulse duration, related to the input pulse amplitude as $|A_S^0|^2 = -k_0''/(\gamma\tau_0^2)$, and where $k_{\text{sol}} = -k_0''/(2\tau_0^2) = \gamma|A_S^0|^2/2$ represents the nonlinear phase shift experienced by the pulse upon propagation. These conditions also imply that k_0'' and n_2 must have opposite signs in order for Eq. (1.27) to represent a physical quantity and this manifests also from Eq. (1.25), where k_0'' and γ must have opposite signs in order for

the GVD to compensate for self-phase modulation. As an example, Figure 1.9 shows the numerically evaluated 1D propagation of a sech^2 soliton-like pulse, launched in the anomalous dispersion region of fused silica [shaded area in Fig. 1.4(a)], where the nonlinearity and GVD are balanced over a distance of ~ 1.8 mm.

The most remarkable fact is actually not the possibility of the mentioned balance of dispersion and nonlinearity, but rather that soliton solutions of the nonlinear wave equation are very stable: even for substantial deviations of the initial pulse from the exact soliton solution, the pulse automatically “finds” the correct soliton shape while shedding some of its energy into a so-called *dispersive wave* [43, 44, 45, 46], which is also known as *resonant radiation*, or Cherenkov radiation [47].

1.4.1 Dispersive waves: phenomenology

When an optical pulse is launched into a fiber with anomalous chromatic dispersion so that the pulse parameters do not exactly match those of a soliton, the pulse will evolve (within some propagation distance in the fiber) into a soliton pulse and some temporally spreading background. The latter is called a “dispersive wave”, because it is spreading due to the effect of GVD ($k'' > 0$), and this is not compensated by the fiber nonlinearity [44]. The closer the parameters of the initial pulse are to the parameters of a soliton, the higher is the percentage of the pulse energy which ends up in the soliton rather than in the dispersive wave.

Dispersive waves emitted by fiber solitons in presence of higher order dispersions have been known for a long time. In 1987 Wai et al. [45] theoretically predicted that, if launched close to the region of minimum dispersion, solitons would emerge from pulses of any arbitrary shape and amplitude, provided that, with increasing input amplitude, the soliton automatically “recoils” and shifts toward redder frequencies, while the frequency of the dispersive wave component would correspondingly increase (blue-shift). This theoretical prediction was then experimentally verified by Gouveia-Neto et al. in 1988 [48]. Figure 1.10 shows the numerically evaluated propagation of a soliton launched at the zero dispersion wavelength (ZDW) in fused silica ($\sim 1.3 \mu\text{m}$). The top row (a)-(b) refers to an almost stationary propagation thanks to the balance of GVD and nonlinearity (low intensity regime). By changing only one parameter, i.e. by

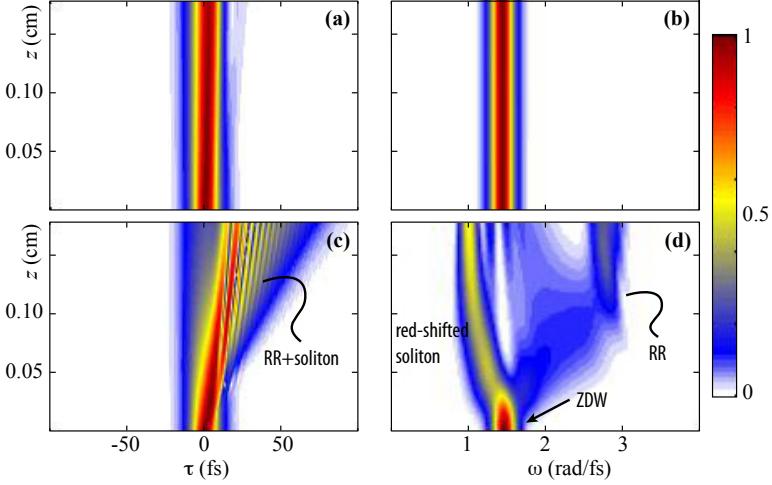


Figure 1.10: Numerics: Soliton and resonant dispersive wave (indicated with RR) at the ZDW in fused silica (input carrier wavelength $\lambda_0 = 1.3 \mu\text{m}$; input pulse duration $\tau_0 = 8 \text{ fs}$). Envelope (right-hand side) and spectrum (left-hand) for two different input intensity conditions: $I_0 \cong 10^9 \text{ W/cm}^2$ (a)-(b) and $I_0 = 10 \text{ TW/cm}^2$ (c)-(d).

increasing the input intensity, the spectrum splits into two peaks at the either sides of the ZDW [Figure 1.10(d)]: the Kerr nonlinearity downshifts the frequency, moving the soliton further into the anomalous dispersion region, which simultaneously transfers energy into a blue-shifted dispersive wave, or resonant radiation (RR), in the normal dispersion region.

The self-frequency shift of the soliton is also known as *spectral recoil* effect and has been reported to arise in photonic crystal fiber (PCF) [49, 50], and explained in terms of an overall photon energy conservation. In microstructured fibers, Tartara et al. [46] show evidence of spectral broadening based upon the fission of higher-order solitons into red-shifted fundamental solitons and blue-shifted dispersive waves. They tentatively propose an explanation of this effect by invoking pulse-trapping phenomena controlled by the group-velocity matching of infrared and visible pulses. Moreover energy exchange between the soliton and the resonant dispersive wave is expected to reach its maximum close to the zero GVD wavelengths, since energy is fed into the wave from the most intense central part of the soliton spectrum. This is because the amplitude of the emitted radiation is primarily determined by the spectral amplitude of the soliton at the radiation frequency ω_{RR} [47].

Kolesik et al. re-interpreted the soliton shedding of light towards the RR frequency as a linear scattering event in the *first Born approximation* [51]. In Section 2.2 we shall recall this powerful picture, comprising many spectral broadening phenomena, from supercontinuum generation to RR, induced by the nonlinear propagation of both solitons in 1D optical fibers [51] and X-waves in 3D bulk Kerr media [33, 52, 53, 54, 55].

Chapter 2

Scattering theory of SC and RR

In this Chapter we shall treat the phenomenon of resonant radiation (RR) analytically, by means of two different approaches: i.e., the theory of Akhmediev and Karlsson [47], and the *effective three-wave mixing* (ETWM) picture of Kolesik et al. [51], which describes the process as a linear scattering event in the context of the *first Born approximation*. This picture has been shown to provide an accurate analytic description of supercontinuum (SC) spectral properties in both 3D bulk media and 1D optical fibers. In the last Section we shall derive the Unidirectional Pulse Propagation Equation (UPPE) which will be numerically solved in the next chapters to investigate the scattering mechanism inducing RR.

2.1 Akhmediev theory of Resonant Radiation

In 1995, Akhmediev and Karlsson developed an analytic, although approximate, method of calculating the amount of radiation emitted by solitons perturbed by higher-order dispersion effects in fibers [47]. Following their perturbative analysis, we rewrite the NLS Equation (1.25) as,

$$i \frac{\partial A_S}{\partial z} + \frac{1}{2} \frac{\partial^2 A_S}{\partial t^2} + |A_S|^2 A_S = \varepsilon \hat{P}(A_S), \quad (2.1)$$

where we have included a perturbative operator \hat{P} in the right-hand side, which, e.g. in the case of *third-order dispersion* (TOD), is $\hat{P} = i\partial^3/\partial t^3$.

The parameter ε is assumed to be sufficiently small for the soliton to exist. The unperturbed ($\varepsilon = 0$) soliton solution is again, as Eq. (1.27),

$$A_S(z, t) = A_0 \operatorname{sech}(A_0 t) e^{ik_{\text{sol}} z}, \quad \text{where} \quad k_{\text{sol}} = \frac{A_0^2}{2}. \quad (2.2)$$

The basis of Akhmediev's reasoning is that the soliton wave number k_{sol} lies in a range that is forbidden for linear dispersive waves, and thus energy cannot be transferred from the soliton to the linear waves. For the same reason, solitons are sensitive to perturbations having the soliton wave number. The resonance condition for the radiation frequency is thus found by imposing:

$$k_{\text{lin}}(\omega) = k_{\text{sol}}, \quad (2.3)$$

where the linear dispersion relation corresponding to Eq. (2.1) is obtained by substituting $\exp[i(k_{\text{lin}} z + \omega t)]$ into Eq. (2.1) and neglecting the nonlinear term. For example, in the case of TOD we have,

$$k_{\text{lin}}(\omega) = -\frac{1}{2}\omega^2 - \varepsilon\omega^3, \quad (2.4)$$

and thus the soliton is in resonance with the dispersive wave at the resonant frequency ω_{RR} , defined by Eqs. (2.3)+(2.4):

$$\frac{A_0^2}{2} = -\frac{1}{2}\omega_{\text{RR}}^2 - \varepsilon\omega_{\text{RR}}^3, \quad (2.5)$$

which is the phase-matching condition for instability. To lowest orders in ε , the frequency of the resonant radiation (with respect to the soliton frequency) reads,

$$\omega_{\text{RR}} = -\frac{1}{\varepsilon} \left[\frac{1}{2} + 2(\varepsilon A_0)^2 + O(\varepsilon A_0)^4 \right], \quad (2.6)$$

which is proportional to the soliton amplitude A_0 .

It is also possible to find a fully analytical expression for the radiation intensity $f(z, t)$, considering the general solution of Eq. (2.1) as,

$$A(z, t) = A_S(z, t) + f(z, t), \quad \text{with} \quad |f(z, t)| \ll |A_S(z, t)|,$$

over the body of the soliton. By linearizing Eq. (2.1) in f , it is found that the radiated energy is mostly governed by a source term given by $\varepsilon \hat{P}(A_S)$. The modulus of the Fourier amplitude of the radiation is thus characterized

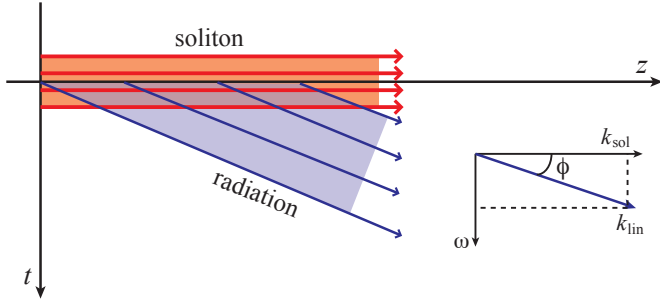


Figure 2.1: Resonant radiation can be viewed as a Cherenkov process, where the “Cherenkov angle” ϕ , is defined by Eq. (2.8). Figure adapted from Ref. [47].

by a dominant factor equal to the spectral value of the source term at the resonant frequency, i.e., $P(\omega_{RR})$, where,

$$P(\omega) = \int_{-\infty}^{+\infty} \hat{P}\{A_S(t)\}e^{-i\omega t} dt. \quad (2.7)$$

This confirms that resonant generation of the emitted radiation is proportional to the spectral content of the soliton at the radiation frequency. It is the spectral tail of the soliton in the normal GVD regime that boosts the radiation. Moreover a conservation of momentum holds, which explains the *spectral recoil* effect. Indeed the spectral center of mass is an invariant of Eq. (2.1). Thus, if a soliton loses energy by emitting linear waves in the normal dispersion region, it will “recoil” into the anomalous regime.

2.1.1 Relation to Cherenkov radiation

Classical Cherenkov radiation appears when a small object (particle) moves in a medium with a velocity exceeding the phase velocity of the waves in the given medium [56]. The source of the radiation may be either a real particle, or e.g., a polarization wave induced by some nonlinear interaction in a dielectric medium. If the size of the source is comparable with the wavelength at least in one direction, then the radiation is defined in this direction by the “Cherenkov conditions” rather than full phase-matching conditions. The concept of Cherenkov radiation in nonlinear optics was introduced by Tien et al. in 1970 to describe the “tilted” second harmonic generation from a thin-film waveguide [57].

The radiation emitted by solitons in optical fibers can be interpreted as a *Cherenkov-like radiation*, if the retarded time t is interpreted as a “transverse” coordinate, as in Fig. 2.1. Then the emitted radiation can be considered as phase-matched along the z direction, but not phase-matched along the “transverse” t axis. Moreover the phase velocity of the soliton in the z direction is higher than the phase velocities of linear waves outside the soliton. The physical consequence of this fact is that radiation is emitted at the “Cherenkov angle” ϕ , with respect to the soliton propagation direction z , defined by the longitudinal phase-matching condition $k_{\text{lin}} = k_{\text{sol}}$, i.e.,

$$\sin \phi = \frac{\omega_{\text{RR}}}{\sqrt{k_{\text{sol}}^2 + \omega_{\text{RR}}^2}}, \quad (2.8)$$

in a reference frame centered on the soliton frequency ($\omega_S = 0$). As shown in [47], the intensity of this radiation is proportional to the square of the spectral component of the source. It decreases when the width of the source increases, but becomes higher for small soliton widths, as would be expected for Cherenkov radiation.

2.2 First Born approximation

The soliton shedding of light towards the resonant peak can be described as a linear *scattering* event in an *effective three-wave mixing* (ETWM) picture, developed by Kolesik et al. to describe the supercontinuum spectral properties and revealing the dynamics within the high-intensity core of a collapsing filament. Kolesik demonstrates that in one- [51], two- [58] or three- [33, 52] dimensions, the physical interpretation of the process is the same: the input (soliton or pump) pulse is self-scattered by the nonlinearly modified refractive index, induced through the Kerr effect (1.17), i.e., $\delta n = n_2 I$ (I is the peak intensity and n_2 the nonlinear Kerr coefficient). This moving DP (or inhomogeneity), effectively acts as a “scattering potential” which may be described within the context of the *first Born approximation*. This means that the involved waves interact only once before detaching apart and no further “cascading” effects take place due to the low scattering amplitude of higher orders terms [21].

As in all the scattering processes, the input and output scattered mode should obey precise momentum conservation laws, which define the precise spectral location of the scattered frequency, ω_{RR} . A phase-matching

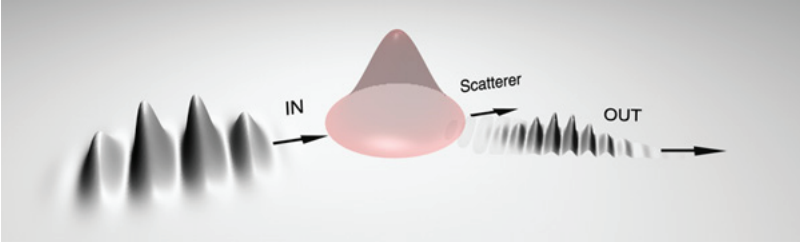


Figure 2.2: Scattering from a moving scatterer in the first Born approximation.

condition holds between the soliton and the resonant “scattered” mode wave-vectors [51, 59]:

$$k(\omega_{\text{RR}}) = k(\omega_S) + \frac{\omega_{\text{RR}} - \omega_S}{v} + \Delta k_{\text{NL}}, \quad (2.9)$$

where $k = \omega n(\omega)/c$ is the material (or fiber) dispersion, v is the soliton velocity and the last term on the right is the nonlinear correction term that for a soliton is $\Delta k_{\text{NL}} = \omega_S n_2 I / (2c)$, that may be small or even negligible at low intensity, I [43]. We note that Eq. (2.9) is a momentum conservation law among three “waves” as long as the term $(\omega_{\text{RR}} - \omega_S)/v$ is interpreted as the momentum associated to the moving dielectric perturbation. Moreover, Eq. (2.9) is the optical fiber counterpart of the X-wave relation (1.24). In bulk media, a stationary 3D X-wave sheds light, in a fashion similar to the 1D soliton, towards a blue-shifted peak which will form one of the two X-wave tails [54, 55]. Hence the dispersion relations (1.24)-(2.9) describe essentially the same scattering processes.

Kolesik et al. slightly modified the first Born approximation for the supercontinuum, in order to take into account that at each z , the velocity and the central frequency of the “incident” IN-wave changes due to the soliton self-frequency shift, i.e., $\omega_S = \omega_S(z)$. Then the first Born approximation for the spectral amplitude $S(L, \omega)$ (at propagation distance L) reads,

$$S(L, \omega) \approx \int dt \int_{-\infty}^L dz e^{i[\omega t - k(\omega)z]} R(z, t) e^{-i[\omega_S(z)t - k(\omega_S(z))z]}. \quad (2.10)$$

Reading right to left, the first term is the IN-wave contained within the solitonic pulse, followed by the “scattering potential” R , given by the nonlinear local change in the index of refraction, $\delta n(z, t) = n_2 I(z, t)$ and, finally, the

resulting, “scattered” wave at ω . Making a few approximations it is possible to derive a simple analytic formula which well describes the dispersive peak in the supercontinuum spectrum [51].

We note that Eq. (2.10) is very general since it may describe the scattering process between an input IN-mode which has being scattered by an “arbitrarily” generated moving perturbation δn , towards a frequency-shifted *resonant* output mode (see e.g. Fig. 2.2). With this in mind, in Section 3.2 we will generalize the ETWM picture so to model the scattering potential $R(z, t)$ as a *linear* moving DP.

2.3 UPPE derivation

The numerical results presented in Chapter 4 are based on the numerical solution of a “Unidirectional Pulse Propagation Equation” (UPPE) code [60]. These numerics shall provide an accurate description of the scattering mechanism inducing RR which, together with the scattering approach, allow us to explain new spectral features ascribable to a new kind of resonant radiation, excited on the *negative* frequency dispersion branch [8, 7]. In the following we derive an expression for the UPPE and we describe in detail our numerical model.

We consider the temporal Fourier domain of the wave equation (1.11) in the *scalar wave approximation*, which holds for loosely focused linearly polarized electric fields ($\hat{\mathbf{E}} = \hat{E}\mathbf{e}_x$, $\hat{\mathbf{P}}_{\text{NL}} = \hat{P}_{\text{NL}}\mathbf{e}_x$):

$$(\partial_{zz}^2 + \nabla_{\perp}^2)\hat{E} + k^2(\omega)\hat{E} = -\mu_0\omega^2\hat{P}_{\text{NL}}, \quad (2.11)$$

where $\partial_{zz}^2 = \partial^2/\partial z^2$ and $\nabla_{\perp}^2 = \partial_{xx}^2 + \partial_{yy}^2$. The *real* fields E, P may be written as the real parts of the corresponding complex fields \mathcal{E}, \mathcal{P} .

By performing a Fourier transform over the transverse coordinate x, y , Eq. (2.11) for the complex fields becomes:

$$(\partial_{zz}^2 + k_z^2)\tilde{\mathcal{E}}(k_x, k_y, z, \omega) = -\mu_0\omega^2\tilde{\mathcal{P}}_{\text{NL}}(k_x, k_y, z, \omega), \quad (2.12)$$

where the longitudinal wave vector is linked to the transverse components as $k_z = [k^2(\omega) - k_x^2 - k_y^2]^{1/2}$. In the linear case, when the left-hand side of Eq. (2.11) is zero, the general solution is a superposition of two solutions, which represent waves propagating in the *forward* and *backward* directions,

$$\tilde{\mathcal{E}} = \tilde{\mathcal{E}}^{(+)} + \tilde{\mathcal{E}}^{(-)} = f^{(+)}(k_x, k_y, \omega)e^{+ik_z z} + f^{(-)}(k_x, k_y, \omega)e^{-ik_z z}.$$

In the nonlinear case, the polarization density acts as a coupling between the forward and backward propagating components. To avoid this we make the “unidirectional propagation approximation”, which consists in considering, in the nonlinear term, only the contribution given by the forward propagating electric field. We can safely neglect the backward propagating component since we are interested in processes that requires long propagation distances compared to the typical laser-matter interaction length. This approximation translates in the requirement that $|\tilde{\mathcal{E}}^{(-)}| \ll |\tilde{\mathcal{E}}^{(+)}|$. If we formally decompose the operator in the left hand side of Eq. (2.12) into,

$$(\partial_z + ik_z)(\partial_z - ik_z)\tilde{\mathcal{E}}(k_x, k_y, z, \omega) = -\mu_0\omega^2\tilde{\mathcal{P}}_{\text{NL}}(k_x, k_y, z, \omega), \quad (2.13)$$

the unidirectional approximation implies that $(\partial_z + ik_z) = 2ik_z$, where $\tilde{\mathcal{E}}$ now represents only the forward propagating component and we are assuming $\tilde{\mathcal{P}}_{\text{NL}}$ as a function of this forward component only.

We can apply a similar procedure to the Equation (2.11) for the complex fields, assuming $[\partial_z + ik(\omega)] \sim 2ik(\omega)$, which implies a further approximation: the “paraxial approximation” that is equivalent to have small transverse propagation angles, i.e. $(k_x^2 + k_y^2) \ll k(\omega)$. We thus obtain the *forward Maxwell equation*:

$$\partial_z \hat{\mathcal{E}} = i \left(\frac{1}{2k(\omega)} \nabla_{\perp}^2 + k(\omega) \right) \hat{\mathcal{E}} + i \frac{\mu_0\omega^2}{2k(\omega)} \hat{\mathcal{P}}_{\text{NL}}. \quad (2.14)$$

It is useful to solve the propagation equation in the reference frame comoving with the pulse, by using a new set of coordinates:

$$\begin{aligned} \zeta &= z \\ \tau &= t - z/v, \end{aligned}$$

where v is the velocity at which the new reference frame is moving. This transformation implies $\partial_z = \partial_{\zeta} - 1/v\partial_{\tau}$ and $\partial_{\tau} = \partial_t$. Equation (2.14) becomes:

$$\partial_{\zeta} \hat{\mathcal{E}} = i \left(\frac{1}{2k(\omega)} \nabla_{\perp}^2 + k(\omega) - \frac{\omega}{v} \right) \hat{\mathcal{E}} + i \frac{\mu_0\omega^2}{2k(\omega)} \hat{\mathcal{P}}_{\text{NL}}. \quad (2.15)$$

2.3.1 Numerical model

The code adopted for the numerical results presented in this thesis is a 1D UPPE solver [60] for the spectral components, $E_{\omega}(z) = \hat{E}(z, \omega)$ of the *real*

field $E(z, t)$. The model equation in the pulse, or dielectric inhomogeneity, frame reads [7],

$$\partial_z E_\omega - i[k_z(\omega) - \omega/v]E_\omega = i \frac{\omega^2}{2\epsilon_0 c^2 k_z(\omega)} P_\omega, \quad (2.16)$$

being ϵ_0 the vacuum permittivity, c the speed of light in vacuum and P_ω the spectral component at frequency ω of the real-valued *nonlinear* polarization, that refers to the Kerr nonlinearity,

$$P(z, t) = \epsilon_0 n_0 n_2 |\mathcal{E}(z, t)|^2 E(z, t), \quad (2.17)$$

where \mathcal{E} is the complex valued analytical signal and $(1/2)n_2|\mathcal{E}(z, t)|^2$ gives the dimensionless refractive index variation.

For the *linear* “toy-model” case presented in Chapter 4, the polarization source term $P(z, t)$ has been implemented as a linear DP, travelling at velocity v along the z direction, i.e.,

$$P(z, t) = \epsilon_0 \{ [n_0 + \delta n(t - z/v)]^2 - n_0^2 \} E(z, t), \quad (2.18)$$

where the background term, n_0 , is the refractive index at the input carrier frequency and $\tau = t - z/v$ is the local time coordinate. The “artificial” DP (δn) has a super-Gaussian longitudinal profile of amplitude δn_0 and thickness σ :

$$\delta n(\tau) = \delta n_0 \exp[-(\tau - t_0)^m / \sigma^m], \quad (2.19)$$

being m a positive even number identifying the Gaussian order and t_0 the initial temporal position.

Moreover, we extend the model in order to include also the more general case of a *cross-scattering* event, between a soliton-induced inhomogeneity and a weaker probe pulse. We thus added in the UPPE solver a second equation for the real field of the probe pulse, $E_2(z, t)$, coupled to the equation for the soliton (2.16):

$$\partial_z E_{2,\omega} - i[k_z(\omega) - \omega/v]E_{2,\omega} = i \frac{\omega^2}{2\epsilon_0 c^2 k_z(\omega)} P_{2,\omega}. \quad (2.20)$$

The coupling is indeed given by the “cross-phase modulation” term of the nonlinear polarization (see Section 1.2.3),

$$P_2(z, t) = 2\epsilon_0 n_0 n_2 |\mathcal{E}(z, t)|^2 E_2(z, t), \quad (2.21)$$

where \mathcal{E} is the complex valued analytical signal of the pump (soliton), as in Eq. (2.17). We intentionally neglect all the other nonlinear terms, e.g. third harmonic generation, four-wave mixing and Raman scattering, in order to highlight the generation of the resonant modes.

The numerical results reported in this thesis are mostly obtain with the UPPE code described above. Nevertheless, we perform simulations using also: (i) the Finite-Difference-Time-Domain (FDTD) technique applied to the discretized Maxwell equations [61]; and (ii) the Pseudo-Spectral-Space-Domain (PSSD) technique [62] that is a variation of the more common FDTD technique. With both the FDTD and the PSSD codes we obtain essentially the same results, as reported in [13] and [63].

Chapter 3

Negative frequencies

Resonant radiation frequency-conversion describes an energy transfer between specific modes identified by Eq. (2.9). In this Chapter we will show that, in the presence of a moving DP, coupling among *positive* and *negative* frequency branches of the dispersion relation allows excitation of a new resonant mode which lies on the negative-frequency branch, and hence called *negative resonant radiation* (NRR) [8, 7]. We shall provide a physical interpretation of the existence of negative frequencies and, in Section 3.2, we propose a mathematical description of the NRR mode, based on the framework of the first Born approximation. In Sec. 3.3 we shall derive a “generalized” Manley-Rowe relation for the photon numbers of the modes involved in the scattering process. We predict photon number amplification mediated by the moving scatter (or DP) every time that negative frequencies are being generated.

3.1 Negative frequencies in optics and other systems

Light always oscillates with both positive and negative frequencies. This is a simple mathematical consequence of Fourier analysis: a light wave E is made of its frequency spectrum \tilde{E} by Fourier transformation,

$$E = \int_{-\infty}^{+\infty} \tilde{E}(\omega) e^{-i\omega t} d\omega,$$

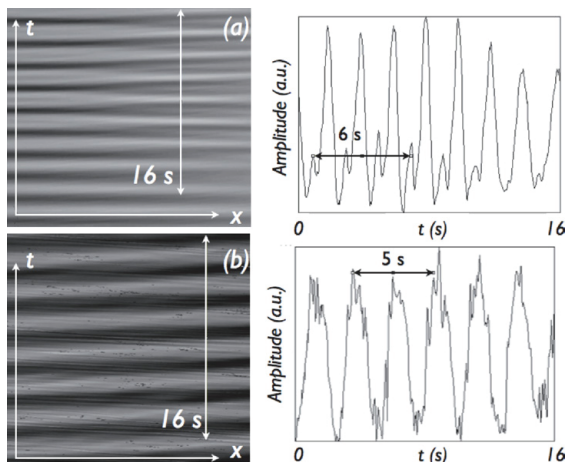


Figure 3.1: Negative-frequency waves in water. Space-time diagrams of a positive-frequency wave (a) and a negative-frequency (negative phase slope) wave (b). Figure from Ref. [66].

where the (angular) frequency ω runs over all real numbers, including negative ones. As the electromagnetic field E is a *real-valued* quantity, the complex conjugate E^* equals E and hence

$$\tilde{E}(-\omega) = \tilde{E}^*(\omega).$$

The positive spectrum of light is always “shadowed” by a negative spectrum that is the complex conjugate. Since the negative-frequency part is directly related to its positive-frequency counterpart it has always been considered redundant for light waves [64]. On the other hand, light particles (photons) have positive energies, $\mathcal{E} = \hbar\omega$, and are associated with positive frequencies only [65]. A process which mixes positive and negative frequencies is thus expected to change the number of photons, leading to *amplification* or even particle creation from the quantum vacuum [68, 69].

The negative-frequency dispersion branch is usually neglected, while in reality, it may host mode conversion to new frequencies. In Sec. 2.2 we saw that a soliton interacts with the self-induced refractive index variation and scatters light to the RR mode through a process that is well known and usually referred to as resonant or dispersive-wave radiation. More recently, we have demonstrated that this same process may generate a second, negative-frequency mode [8, 7], the NRR mode, which finds an explanation in terms of scattering from a *moving* DP (see Sec. 3.2).

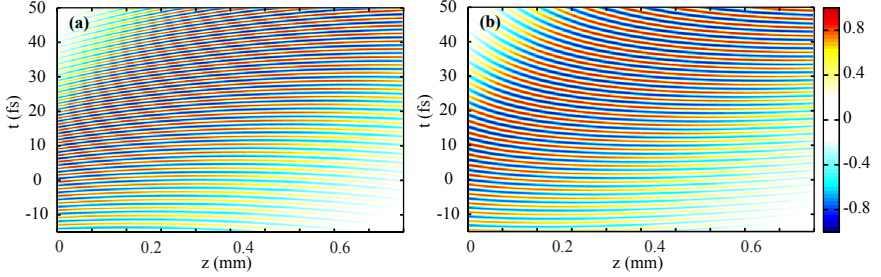


Figure 3.2: Negative frequencies in a type-I seeded OPA process. Signal (a) and idler (b) phase-fronts in the pump pulse phase velocity reference frame. The phase modulation in both fields is due to the chirp of the input seed pulse. Figure adapted from Ref. [67].

These results are not limited only to nonlinear optics, but are a general property of wave propagation in a dispersive medium: if the dispersion relation allows coupling between the positive and negative dispersion branches, then a similar excitation of negative modes may be expected. Relevant examples of *experimentally* realizable systems are gravity waves in water [66, 70] or acoustic oscillations in Bose-Einstein condensates (BECs) [71]. In [66], Rousseaux et al. report on the first direct observation of negative-frequency waves converted from positive-frequency waves in a moving medium (water). Positive- (*negative*-) frequency water waves have been shown to have phase-fronts with positive (*negative*) slopes, corresponding to positive (*negative*) phase velocity in the reference frame of the moving water flow. Figure 3.1(a)-(b) show the space-time diagrams of positive- and negative-frequency water waves, respectively.

We see that the scattering picture from a moving medium is very general and, in principle, we may apply the “first Born approximation” approach also to second-order, $\chi^{(2)}$, nonlinear processes such as, e.g., the optical *parametric down conversion* (PDC) [21]. The input pump pulse at frequency ω_p is converted into a “signal” and an “idler” field, at frequencies ω_s and ω_i respectively, following energy and momentum conservation constraints: i.e., $\omega_p = \omega_s + \omega_i$ and $\mathbf{k}_p = \mathbf{k}_s + \mathbf{k}_i$, with $k = |\mathbf{k}| = \omega n(\omega)/c$. If plotted in the reference frame comoving with the *phase* velocity of the pump, the phase-fronts of signal and idler present positive and negative slopes, respectively. Figure 3.2 (adapted from Ref. [67]) shows the space-time diagrams for signal (a) and idler (b) respectively, plotted in the reference frame of the pump pulse phase velocity. The process can thus be inter-

preted within the first Born approximation theory (Sec. 2.2), in which the “scattering potential”, or “polarization wave”, is now proportional to the *electric field* (and not to the envelope) of the pump wave and is moving with the pump phase velocity. Moreover, if seeded by an external coherent field, PDC supports *optical parametric amplification* (OPA) of the signal.

3.1.1 Lab and comoving frame description

In the presence of a moving medium negative frequencies are not just a mathematical artifact, but they allow true energy transfer, in the sense of an increase in the photon number, towards a different resonant mode. To better understand this, we first look at the dispersion curve in the laboratory frame and in the reference frame comoving with the moving scatterer (Figure 3.3). These curves are obtained from the original dispersion relation by transforming via a Doppler shift to the dielectric perturbation (or soliton) comoving coordinate system:

$$\omega' = \gamma(\omega - vk) \quad (3.1)$$

$$k' = \gamma\left(k - \frac{\omega v}{c^2}\right), \quad (3.2)$$

where $\gamma = 1/\sqrt{1 - (v/c)^2}$, c is the speed of light in vacuum and v is the velocity of the moving DP. Figure 3.3 shows diamond (left-hand side) and fused silica (right-hand side) dispersion curves in the laboratory (ω, k) and in the comoving (ω', k') reference frame, as described in the caption. For fused silica glass only optical dispersion branches are considered, while phononic branches are neglected. Dashed curves indicate the (laboratory frame) negative frequency branches, also known as the complex conjugate (*c.c.*) domains. Grey shaded areas indicate the domains of the backward propagating modes (namely, the 2nd and 4th quadrants), which are not considered in this work. In Fig. 3.3(f) we present the dispersion relation for fused silica in a format that has been used when describing optical solitons [72]. $D(\omega)$ is a Taylor expansion of the dispersion $k(\omega)$ around the input frequency ω_{IN} ,

$$D(\omega) = \sum_n (k_n)|_{\omega_{\text{IN}}} \frac{(\omega - \omega_{\text{IN}})^n}{n!}, \quad \text{with} \quad k_n = \frac{d^n k(\omega)}{d\omega^n}. \quad (3.3)$$

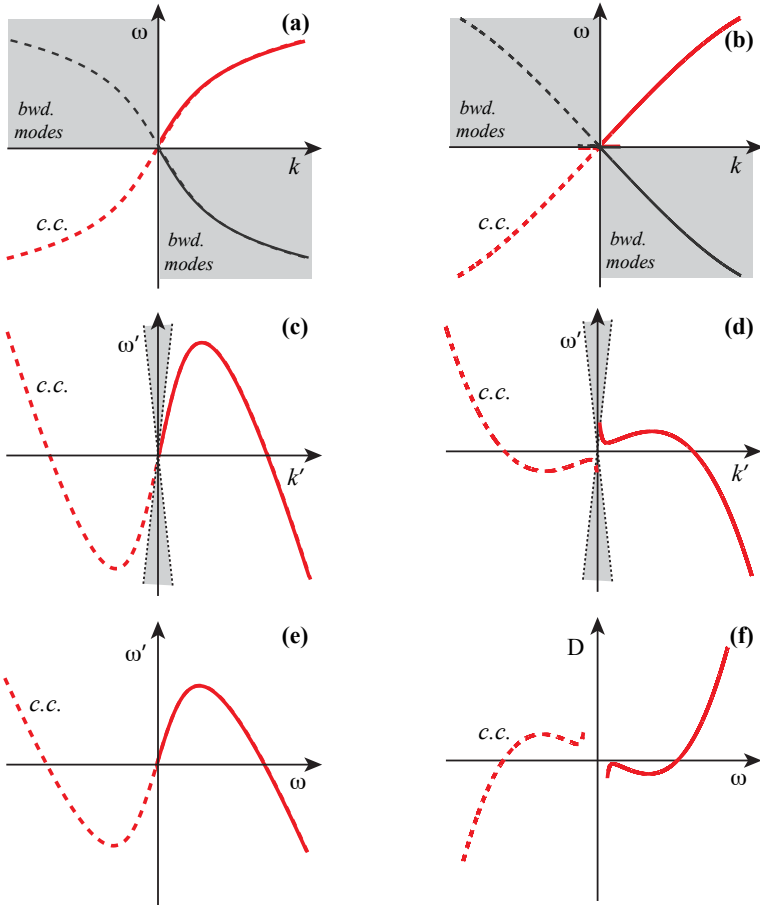


Figure 3.3: Dispersion curves $k = k(\omega)$ for diamond (left-hand side) and fused silica (right-hand side). The curves are plotted in the laboratory reference frame (a)-(b) and in the comoving reference frames (ω', k') (c)-(d) and (ω, ω') (e) for diamond only. For fused silica we plot also the dispersion $D = D(\omega)$ as described in the text (f), for $n \geq 2$. Dashed curves indicate the complex conjugate (c.c.) domain, while grey shaded areas indicate the regions of the backward propagating modes.

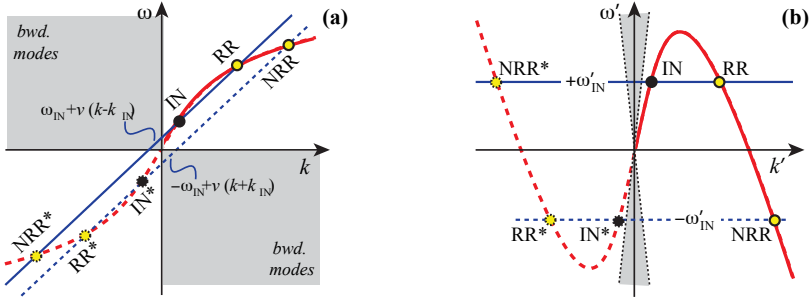


Figure 3.4: (a) Dispersion relation of diamond in the lab. frame (ω, k) and (b) in the reference frame (ω', k') moving at velocity v . Solid (dashed) red curves correspond to positive (negative) dispersion branch in the lab. frame. Straight blue lines indicate the momentum conservation condition, Eq. (3.4) (solid blue), and its “phase-conjugate” counterpart (dashed blue). Grey shaded areas indicate the domains of backward propagating modes in the lab. frame, which are not excited by a forward propagating input pulse and are not considered in this work.

In order to understand the origin of the negative RR mode, it is useful to find its coordinates on the dispersion curve $k(\omega)$ by graphically solving Eq. (2.9), where for simplicity we take the nonlinear correction term $\Delta k_{\text{NL}} = \omega_{\text{IN}} n_2 I / (2c) = 0$,

$$k(\omega_{\text{RR}}) = k(\omega_{\text{IN}}) + \frac{\omega_{\text{RR}} - \omega_{\text{IN}}}{v}, \quad (3.4)$$

where v is the DP velocity, and ω_{IN} the input carrier frequency. We recall that the last term in Eq. (3.4), $(\omega_{\text{RR}} - \omega_{\text{IN}})/v$, is related to the momentum transferred to the incoming pulse from the DP. We note that by Taylor expanding the output wave vector $k(\omega_{\text{RR}})$ as defined by (3.3), the first two lowest-order terms cancel out in Eq. (3.4), which therefore reduces to $D(\omega) = 0$, with $n \geq 2$ [Figure 3.3(f)].

Without any loss of generality, in Figure 3.4 we now consider a simple dispersion relation such as that of diamond, which does not exhibit any resonances over a very broad bandwidth (from less than one Terahertz through to ultraviolet wavelengths). Equation (3.4) is a straight line when represented in (ω, k) coordinates, as in Fig. 3.4(a) (blue solid line). The frequency and wave-vector values of the propagating modes are thus determined by the overlap of this line with the actually allowed modes in the medium, i.e. by the intersection with the medium dispersion relation (red solid curve). Red dashed curves indicate the negative frequency branch (in the lab. frame) of the dispersion relation as in Fig. 3.3.

A first intersection is identified as the incoming mode IN. A second mode can be found, RR to which light may be resonantly scattered. Although the generation of resonant radiation is typically considered to be a property of self-scattering from intense nonlinear soliton pulses, we note that actually it is a more general process that only requires the existence of some kind of inhomogeneity in a *linear* medium, as discussed here. A third intersection is found on the negative frequency branch of the dispersion curve: this is the negative frequency resonant radiation mode, NRR*. Light may be resonantly transferred to this mode too, alongside the RR mode, as we have observed in recent experiments [8]. We stress that the existence of a solution at negative frequencies is not unphysical, being the electromagnetic field a *real*-valued quantity, that naturally oscillates at positive and negative frequencies. Indeed, the mode that is actually measured in an experiment is obtained by adding the three modes described above with their complex conjugate counterparts. These are found from the intersections of the dispersion curve with the straight dashed line in Fig. 3.4(a), obtained from Eq. (3.4) by substituting ω with $-\omega$ and using the fact that the dispersion relation is an odd function, i.e., $k(-\omega) = -k(\omega)$, and thus,

$$k(\omega_{\text{NRR}}) = -k(\omega_{\text{IN}}) + \frac{\omega_{\text{NRR}} + \omega_{\text{IN}}}{v}, \quad (3.5)$$

Physically, this describes the momentum conservation condition in which the complex conjugate of the IN mode, IN*, is being scattered towards RR* and NRR. In Fig. 3.4(b) we then consider the same dispersion relation in the reference frame that is comoving with the DP, i.e. in (ω', k') given by the Doppler transformations (3.1)-(3.2). In this reference frame the momentum conservation relation (3.4) transforms into a condition on the comoving frequencies, $\omega' = \omega'_{\text{IN}}$, and therefore represented as a horizontal line in the graph. Specifically, we find that the conditions for the RR (3.4) and NRR (3.5) become:

$$\omega'_{\text{RR}} = +\omega'_{\text{IN}} \quad (3.6)$$

$$\omega'_{\text{NRR}} = -\omega'_{\text{IN}}, \quad (3.7)$$

since $\omega'_{\text{NRR}^*} = +\omega'_{\text{IN}}$. The RR (NRR) mode is thus naturally described by a *positive (negative)* frequency in the comoving reference frame, reflecting the fact that RR (NRR) builds from frequencies with positive (negative) local phase velocities. Following the recipe of Rousseaux et al. [66], we

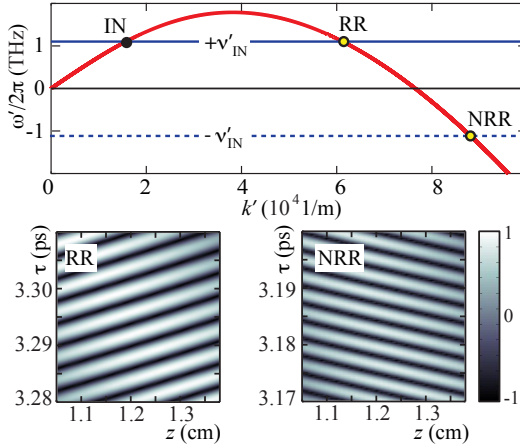


Figure 3.5: Diamond-like comoving dispersion curve with the numerically evaluated phase-fronts of the RR and NRR modes space-time diagram (z, τ) , comoving with the inhomogeneity DP.

indeed verified that the RR (NRR) space-time diagrams present positive (negative) slopes. Figure 3.5 shows the numerically evaluated conversion to the RR and NRR mode on a “diamond-like” dispersion curve, together with the corresponding phase-fronts in the (z, τ) domain, being $\tau = t - z/v$ the retarded time.

3.2 The first Born approximation revisited

In scattering theory the *linear* relation involving input and output modes may be modeled with the scattering matrix \mathbf{S} , which is a unitary matrix connecting asymptotic states and which describes all the scattering channels of the process. Physically the square moduli $|S_{j,i}|^2$ of the \mathbf{S} -matrix elements represent the number of photons for the j -output mode, which is being scattered by the i -input mode. Following Kolesik et al. [51], we evaluate the elements of the \mathbf{S} -matrix in the first Born approximation (presented in Section 2.2), giving an analytical formulation for the spectral amplitude of the scattered wave. We also generalize the treatment in order to include the possibility of a third output scattered mode, i.e. the NRR mode that, as argued above may also be generated during the scattering process. The role of the “scattering potential”, $R(z, t)$, is played by the moving DP, which for simplicity we assume to be stationary along

propagation, i.e.,

$$R(z, t) = R(t - z/v) = \delta n(t - z/v), \quad (3.8)$$

where v is the DP velocity. With this approximation Eq. (2.10) would become:

$$S(L, \omega) \approx \iint dt dz R(t - z/v) e^{i(\omega - \omega_{\text{IN}})t} e^{-i[k(\omega) - k_{\text{IN}}]z}. \quad (3.9)$$

For our “revisited first Born approximation” we now want to derive Eq. (3.9) starting directly from our model equation for the laser pulse evolution, i.e. the UPPE Eq. (2.16), in the laboratory reference frame:

$$\partial_z E_\omega - ik_z(\omega)E_\omega = i \frac{\omega^2}{2\epsilon_0 c^2 k_z(\omega)} P_\omega, \quad (3.10)$$

where the polarization source term $P(z, t)$ has been implemented as a *linear* dielectric perturbation, moving at v , as (2.18),

$$\begin{aligned} P(z, t) &= \epsilon_0 \{ [n_0 + \delta n(t - z/v)]^2 - n_0^2 \} E(z, t) \\ &\simeq 2\epsilon_0 n_0 \delta n(t - z/v) E(z, t), \end{aligned} \quad (3.11)$$

so that the spectral component reads,

$$P_\omega = \frac{1}{2\pi} \int dt 2\epsilon_0 n_0 \delta n(t - z/v) E(z, t) e^{i\omega t}. \quad (3.12)$$

We now want to solve Eq. (3.10) perturbatively by writing,

$$E_\omega(z) = E_\omega^{(0)}(z) + E_\omega^{(1)}(z) + E_\omega^{(2)}(z) + \dots,$$

where $E_\omega^{(l)}(z)$ is of order $(\delta n)^l$. We then get the equations,

$$\partial_z E_\omega^{(0)} - ik_z(\omega)E_\omega^{(0)} = 0, \quad (3.13)$$

$$\partial_z E_\omega^{(1)} - ik_z(\omega)E_\omega^{(1)} = i \frac{\omega^2 n_0}{c^2 k_z(\omega)} \frac{1}{2\pi} \int dt \left[\delta n(t - z/v) e^{i\omega t} \int e^{-i\omega' t} E_\omega^{(0)}(z) d\omega' \right], \quad (3.14)$$

⋮

From (3.13) we get $E_\omega^{(0)}(z) = e^{ik_z(\omega)z} E_\omega^0$, where E_ω^0 is constant. We solve up to the *first*-order Eq. (3.14) and, assuming that for $z \rightarrow -\infty$ there is

only the unperturbed solution, we find,

$$E_{\omega}^{(1)}(z) = i \frac{\omega^2 n_0}{2\pi c^2 k_z(\omega)} e^{ik_z(\omega)z} \int_{-\infty}^z d\xi e^{-ik_z(\omega)\xi} \times \\ \times \left\{ \int \delta n(t - \xi/v) e^{i\omega t} \int e^{-i\omega' t + ik_z(\omega')\xi} E_{\omega'}^0 dt d\omega' \right\}.$$

We can rewrite this as,

$$E_{\omega}^{(1)}(z) = \int d\omega' \sigma(z, \omega, \omega') E_{\omega'}^{(0)}(z), \quad (3.15)$$

where σ is the **S**-matrix density:

$$\sigma(z, \omega, \omega_{\text{IN}}) = i \frac{\omega^2 n_0}{2\pi c^2 k_z(\omega)} e^{i[k_z(\omega) - k_z(\omega_{\text{IN}})]z} \times \\ \times \int dt \int_{-\infty}^z d\xi e^{i[\omega t - k_z(\omega)\xi]} \delta n(t - \xi/v) e^{-i[\omega_{\text{IN}} t - k_z(\omega_{\text{IN}})\xi]}.$$

By using the new set of variables, $u = t - \xi/v$ and $w = t + \xi/v$, we can evaluate the integrals in the last expression, to obtain:

$$\sigma(z, \omega, \omega_{\text{IN}}) \approx i \frac{v\omega^2 n_0}{2c^2 k_z(\omega)} e^{i[k_z(\omega) - k_z(\omega_{\text{IN}})]z} \delta \left\{ \omega - \omega_{\text{IN}} - v \cdot [k_z(\omega) - k_z(\omega_{\text{IN}})] \right\} \\ \times \hat{R} \left\{ \frac{1}{2} \left[\omega - \omega_{\text{IN}} + v \cdot \left(k_z(\omega) - k_z(\omega_{\text{IN}}) \right) \right] \right\}, \quad (3.16)$$

where $\delta\{\cdot\}$ is the Dirac delta function, which is nonzero only for,

$$\omega - \omega_{\text{IN}} - v [k_z(\omega) - k_z(\omega_{\text{IN}})] = 0, \quad (3.17)$$

and $\hat{R}(\omega)$ is the Fourier transform of the scattering potential $\delta n(u)$,

$$\hat{R}(\omega) := \int du \delta n(u) e^{i\omega u}. \quad (3.18)$$

We can now substitute (3.16) in Eq. (3.15) and by performing the integration, using the delta function condition (3.17), we finally obtain:

$$E_{\omega}^{(1)}(z) = S(z, \omega, \omega_{\text{IN}}) E_{\omega_{\text{IN}}}^{(0)}(z), \quad (3.19)$$

where the **S**-matrix element is:

$$S(z, \omega, \omega_{\text{IN}}) = i \frac{v\omega^2 n_0}{2c^2 k_z(\omega)} e^{iz(\omega - \omega_{\text{IN}})/v} \hat{R}(\omega - \omega_{\text{IN}}). \quad (3.20)$$

Summarizing, the scattering matrix elements that describe the scattering of a laser pulse from a DP may be explicitly evaluated from Eq. (3.20): the amplitude of the scattered wave is directly proportional to the Fourier transform of the scattering potential, i.e. of the moving DP, $\hat{R}(\omega)$. Moreover, Eq. (3.4) is equivalent to the Dirac delta function condition Eq. (3.17), and therefore emerges as natural condition that has to be satisfied in order for the scattering process to occur. This provides a firm grounding for the fundamental momentum conservation relation used in this work, Eq. (3.4).

Including also the possibility of scattering to the NRR mode [by substituting ω with $-\omega$ and using the fact that the dispersion relation is an odd function of ω , namely $k(-\omega) = -k(\omega)$, as we did to derived Eq. (3.5)] we finally find that the amplitude of each *resonant* scattering channel (RR or NRR) is proportional to the amplitude of the corresponding Fourier component of the DP, $\hat{R}(\omega)$:

$$S(z, \omega_{\text{RR}}) \approx \frac{v}{2} \hat{R}(\omega_{\text{RR}} - \omega_{\text{IN}}) \quad (3.21)$$

and, accounting also for the negative frequency branch,

$$S(z, \omega_{\text{NRR}}) \approx \frac{v}{2} \hat{R}(\omega_{\text{NRR}} + \omega_{\text{IN}}), \quad (3.22)$$

These relations (3.21) and (3.22) state that energy may be transferred to *two* modes, RR and NRR, and in order to do so the spectrum of the scattering potential must have non-zero Fourier components at frequencies equal to the relative distances between ω_{IN} and the resonant frequencies. Physically, this means that the DP must present a sufficiently steep gradient (its temporal profile should exhibit a fast transient intensity) so as to effectively excite the desired output modes. Experimentally, since the scattering potential $R(t - z/v)$ is the moving dielectric perturbation induced by the soliton (or pump) through the nonlinear Kerr effect, $\delta n(t - z/v) = n_2 I(t - z/v)$, this condition is reasonably satisfied for a suitable choice of input parameters, namely intensity and pulse duration.

3.3 The Manley-Rowe relation and amplification

We now observe that we may derive a photon number balance equation by generalizing the Manley-Rowe relation, adopted e.g. in nonlinear optics [21], to the case of a *moving* scatterer [73, 74, 75].

For the scattering process under study, starting from an input pulse at frequency ω_{IN} , the photon number of the output waves is linked to the photon number of the input mode, $|\text{IN}|^2$, by

$$\text{sign}(\gamma_{\text{RR}})|\text{RR}|^2 + \text{sign}(\gamma_{\text{NRR}})|\text{NRR}|^2 = \text{sign}(\gamma_{\text{IN}}), \quad (3.23)$$

where $|\text{RR}|^2$ and $|\text{NRR}|^2$ are the photon numbers of the RR and NRR modes normalized to the input photon number, $|\text{IN}|^2$, and $\gamma_i = (v_\phi^2 - vv_\phi)_i$, where v_ϕ is the phase velocity of the i -mode. We note that,

$$\text{sign}(\gamma_i) = \text{sign}(\omega_i - vk_i) = \text{sign}(\omega'_i); \quad (3.24)$$

while the real-valued RR mode will have positive frequency in the comoving frame, i.e. $\omega'_{\text{RR}} > 0$, the real-valued NRR mode will always have a negative comoving frequency, $\omega'_{\text{NRR}} < 0$. Hence, Eq. (3.23) assumes the following interesting form:

$$|\text{RR}|^2 - |\text{NRR}|^2 = 1. \quad (3.25)$$

So the *difference* between the normalized number of output photons has to be equal to the photon number in the input mode. As a consequence, the total output photon number,

$$|\text{RR}|^2 + |\text{NRR}|^2 > 1, \quad (3.26)$$

i.e. we have *amplification*. The scattering process mediated by the travelling DP will amplify photons as a result of the coupling between the positive and negative frequency modes. We note that these are the same relations that hold for a $\chi^{(2)}$ optical *parametric amplifier*: photon sum is increased at the expense of the δn .

In the Chapter 4 we shall verify this important theoretical prediction with numerical simulations based on the UPPE model presented in Section 2.3.1.

Chapter 4

Linear and nonlinear moving inhomogeneity

We verified our predictions by numerically simulating the one dimensional propagation of a scalar, real valued, field propagating along the z direction in a transparent and isotropic dielectric medium (diamond and fused silica) that is arranged to scatter from a co-propagating inhomogeneity (DP). The code is a 1D, Unidirectional Pulse Propagation Equation solver [60]. Details of the code are given in Section 2.3.1. We recall that, in order to capture the coupling between positive and negative frequencies, the model equation (and especially the source term), must be correctly implemented by calculating the ω -frequency component of the *real* polarization $P(z, t)$. This is achieved for each propagation step by means of back and forth Fourier transforms allowing for an evaluation of the real electric field $E(z, t)$ from its complex spectral components $E_\omega(z)$. In this Chapter we consider three separate cases: (i) the underlying physics are first exemplified by taking a “toy-model” situation in which the DP is simply a variation in the linear refractive index (Sec. 4.1); (ii) the DP is generated by an actual soliton-like laser pulse through the nonlinear Kerr effect and light from the soliton itself is self-scattered (Sec. 4.2); (iii) the DP is generated by a soliton-like pulse and a second, very weak probe pulse is scattered by the soliton (Sec. 4.2.1). Moreover, in Section 4.3 we generalize the results to a 2-dimensional scattering in a planar waveguide. The whole output angular spectrum (which comprises the IN, RR and NRR modes) is very precisely described by the conical X-wave dispersion relation Eq. (1.24). Finally, in

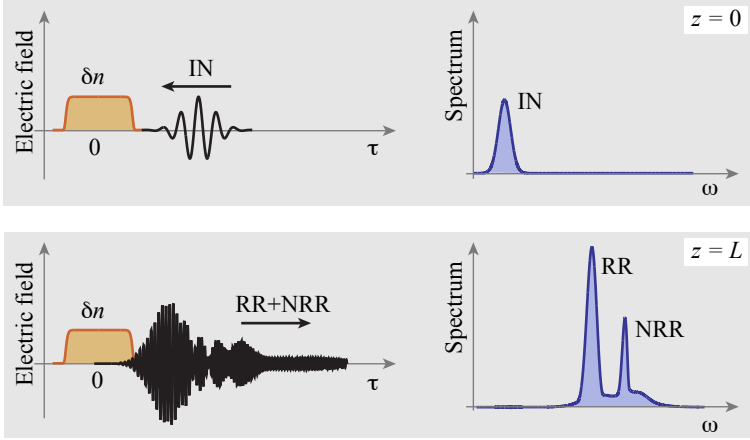


Figure 4.1: Schematic representation of scattering from a dielectric inhomogeneity: an incoming laser pulse, IN, interacts with a co-propagating DP, or scatterer (δn) that transfers energy into two output blue-shifted modes, RR and NRR. Electric field E (left-hand side) and power spectrum (right-hand side), at the input ($z = 0$) and at the end of the interaction after a propagation distance $z = L$. The retarded time is $\tau = t - z/v$, where v is the δn velocity.

the last Section we evaluate the efficiency (gain) of the linear scattering process as a function of the input comoving frequency.

4.1 Toy-model DP

A schematic representation of the specific process we are considering is shown in Fig. 4.1. An incoming laser pulse, IN, with group velocity v_g , interacts with a co-propagating inhomogeneity, or scatterer (δn), with a slightly slower velocity, $v \lesssim v_g$. The momentum conservation law that governs the scattering process (3.4) predicts that light may resonantly scatter into two blue-shifted modes. After some propagation distance $z = L$ (bottom row in Fig. 4.1) the IN mode is fully converted in the two output modes, RR and NRR. Due to dispersion the two blue-shifted modes both travels slower than the input mode and eventually detach from the perturbation: i.e., in the DP reference frame they appear to travel backwards.

The moving perturbation is simulated as a *linear* propagating refractive index inhomogeneity that moves with a speed $v = 1.23 \times 10^8$ m/s that is just slightly slower than the group velocity of an input probe pulse in the medium, $v_g = 1.25 \times 10^8$ m/s. In this case, as a dielectric medium we choose

diamond, which does not exhibit any resonances over a very broad bandwidth (from less than one Terahertz through to ultraviolet wavelengths) as can be seen from the Sellmeier coefficients reported in Table 1.1. The probe pulse is very weak so that no nonlinear effects are excited and the physics are dominated solely by linear scattering from the DP. Figures 4.2(a)-(b) show the evolution along propagation of the envelope (plotted in the frame moving at the DP velocity) and of the spectrum, respectively. We launch an input Gaussian probe pulse (carrier wavelength $2 \mu\text{m}$, pulse width 20 fs), together with a super-Gaussian shaped DP as defined by Eq. (2.19),

$$\delta n(\tau) = \delta n_0 \exp[-(\tau - t_0)^m / \sigma^m],$$

with amplitude $\delta n_0 = 0.08$, $t_0 = -60$ fs, $\sigma = 50$ fs and super-Gaussian order $m = 40$ corresponding to a rising time ~ 3 fs. This ensures a wide DP Fourier spectrum $\widehat{\delta n}(\omega)$, so as to meet both conditions (3.21) and (3.22). After ~ 0.2 mm the probe pulse reaches the moving DP [whose position is highlighted in Fig. 4.2(a) by the vertical black dotted lines] and slows down due to the DP increase of refractive index. Scattering occurs towards *two* blue-shifted resonant modes, RR and NRR, which due to dispersion both travel slower than the DP. The medium dispersion relation is shown in Fig. 4.2(f) in (ω', ω) coordinates where the comoving frequency ω' is given by the Doppler shift (3.1). As explained in Sec. 3.1.1, the absolute value of scattered mode frequencies are determined in the comoving frame by the input mode comoving frequency ($\omega' = \omega'_{\text{IN}}$, blue horizontal solid line and $\omega' = -\omega'_{\text{IN}}$, blue dashed line): the corresponding laboratory reference frame frequencies can be seen to be in perfect agreement with the numerically observed values of Fig. 4.2(b).

We note that, as predicted by the first Born approximation model, NRR is a few orders of magnitude weaker than RR since the spectral amplitude of the scattering potential is weaker at higher frequencies. This is clearly visible in Figure 4.2(d) that shows, in Log-scale, the numerically evaluated DP Fourier spectrum, $\widehat{\delta n}(\omega)$ (blue curve). Two other curves in the figure represent the Fourier spectrum for a higher ($m = 200$, red curve) and lower ($m = 4$, black curve) inhomogeneity steepness, corresponding to rise times from the background refractive index to the maximum of the DP of ~ 0.7 fs and ~ 20 fs, respectively.

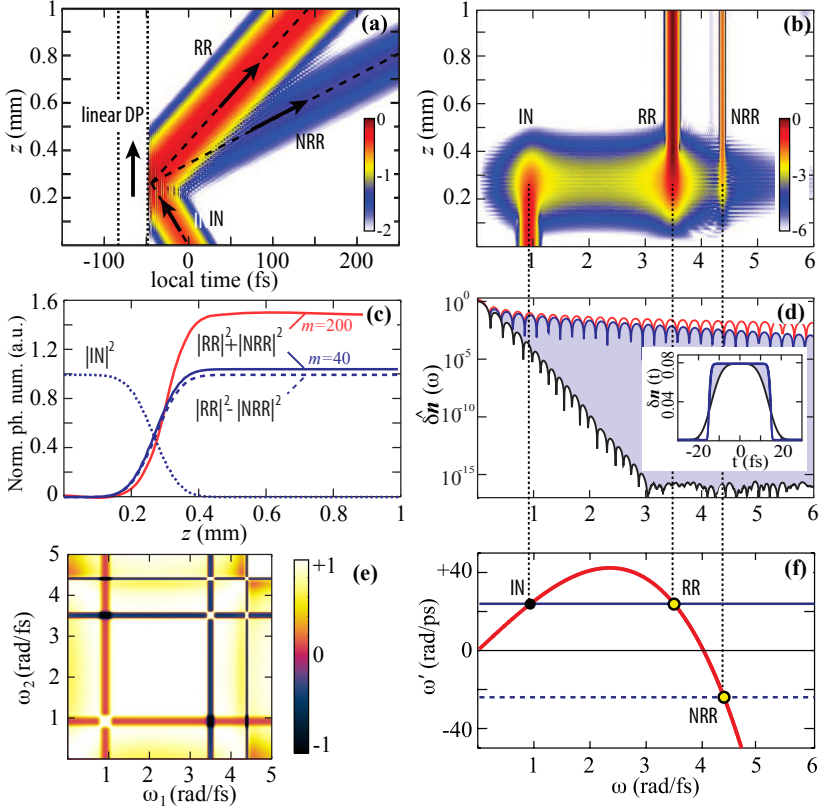


Figure 4.2: Scattering from a “toy-model” DP in diamond: IN pulse at $2 \mu\text{m}$; super-Gaussian moving DP with $m = 40$ (3 fs rise-time), $\delta n_0 = 0.08$. Envelope (a) and spectral (b) evolution along propagation, in Log-scale. (c) Photon number evolution along propagation: the total sum (photon number amplification) increases with increasing DP steepness (increasing parameter m). (d) Fourier spectrum of the DP, $\hat{\delta n}(\omega)$, for three steepness values, i.e., $m = 4$ (black), $m = 40$ (blue) and $m = 200$ (red); inset shows the corresponding DP temporal profiles. (e) Propagation cross-correlation. (f) Comoving dispersion curve with indicated the allowed optical modes.

4.1.1 Photon number amplification

In order to verify the photon number amplification predicted by the Manley-Rowe relation (3.25), we evaluated the photon number evolution, as shown in Fig. 4.2(c) for the two highest DP gradients, obtained by varying the order of the super-Gaussian function that describes the DP, i.e., $m = 40$ and $m = 200$. Dotted, solid and dashed lines correspond to the normalized photon numbers in the IN mode, total output photons $|\text{RR}|^2 + |\text{NRR}|^2$ and output photon difference $|\text{RR}|^2 - |\text{NRR}|^2$, respectively. As can be seen, the difference in photon numbers is conserved while the sum of photon numbers is larger than 1 (amplification) and increases with increasing DP steepness. This simplified “toy-model” therefore gives a direct confirmation of the predictions based on the first Born approximation model.

As a closing remark, we note that in this simulation we have specifically chosen the velocity v and the amplitude δn_0 of the DP to be such that the local increase in refractive index experienced by the approaching IN mode is sufficient to slow it down and achieve a group velocity equal to v . Similar mode-conversion is observed also when the *group velocity matching condition* is not met however with a much reduced efficiency: in this case, the *transmitted* (un-converted) part of the input mode undergoes common cross-phase modulation while passing through the δn , and then escape with unaffected frequency.

4.1.2 Propagation cross-correlation

In Figure 4.2(e) we plot the propagation cross-correlation map as described in [76]. This correlation is positive if frequencies are created simultaneously, i.e. at the same propagation distance z , and negative if one frequency is used to create the other. For each pair of frequencies the propagation cross-correlation is defined as:

$$C(\omega_1, \omega_2) = \frac{\text{Cov}\{I(\omega_1), I(\omega_2)\}}{\sqrt{\text{Cov}\{I(\omega_1), I(\omega_1)\} \text{Cov}\{I(\omega_2), I(\omega_2)\}}}, \quad (4.1)$$

where,

$$\text{Cov}\{I(\omega_1), I(\omega_2)\} = \langle [I(\omega_1, z) - \langle I(\omega_1, z) \rangle] [I(\omega_2, z) - \langle I(\omega_2, z) \rangle] \rangle, \quad (4.2)$$

where $\langle \cdot \rangle$ indicates the expectation value, i.e. the average evaluated over the propagation distance z . The two resonant modes, RR and NRR, are

perfectly correlated (correlation equal to +1), implying that they are born together, whereas they are both anti-correlated with the input mode. This provides further confirmation that indeed the RR and NRR modes are the result of the same scattering process seeded by the IN mode.

4.2 Soliton-induced DP

In this Section we consider the case in which the DP is physically generated by an intense soliton-like laser pulse through the nonlinear Kerr effect, i.e. $\delta n = n_2 I$, where I is the peak intensity and n_2 the nonlinear Kerr coefficient (as described elsewhere in this thesis). The soliton interacts with the self-induced refractive index variation and scatters into new output modes. As a Kerr medium we choose common fused silica glass, whose dispersion relation and Kerr coefficient n_2 are given in Tables 1.1 and 1.2, respectively. We launch a soliton-like mode in the anomalous dispersion region, with central wavelength $2 \mu\text{m}$, pulse width 7 fs and input intensity 10 TW/cm^2 . Figures 4.3(a)-(b) show the envelope and spectral evolution, respectively, along propagation over a distance $z = 0.4 \text{ cm}$. The input pulse initially self-steepens, forms a shock front and, concomitantly, the spectrum starts to broaden towards higher frequencies, exhibiting the typical super-continuum [indicated with SC in Fig. 4.3(a)]. At $z \sim 0.3 \text{ mm}$, when conditions (3.21)-(3.22) are met, energy starts to resonantly transfer from the input mode towards two blue-shifted modes, RR and NRR, both travelling slower with respect to the input soliton. At the end of the interaction the soliton frequency is red-shifted due to the spectral recoil effect and subsequently emerges with a slightly lower propagation velocity. The frequencies of these modes are, again, in perfect agreement with the theoretical predictions as shown in Fig. 4.3(f).

In Figure 4.3(c)-(d) we compare the nonlinear propagation with a numerical simulation in which the nonlinear source term has been replaced with a DP in the *linear* polarization with the same amplitude, steepness and propagation velocity of the soliton induced perturbation of Figs. 4.3(a)-(b). We observe a nearly perfect agreement with the nonlinear case confirming that soliton shedding of RR and NRR modes is nothing more than a specific realization of the more general linear scattering process. The “toy-model” DP scattering is indeed able to capture all the essential features of the resonant energy transfer, and coupling between positive and negative frequency

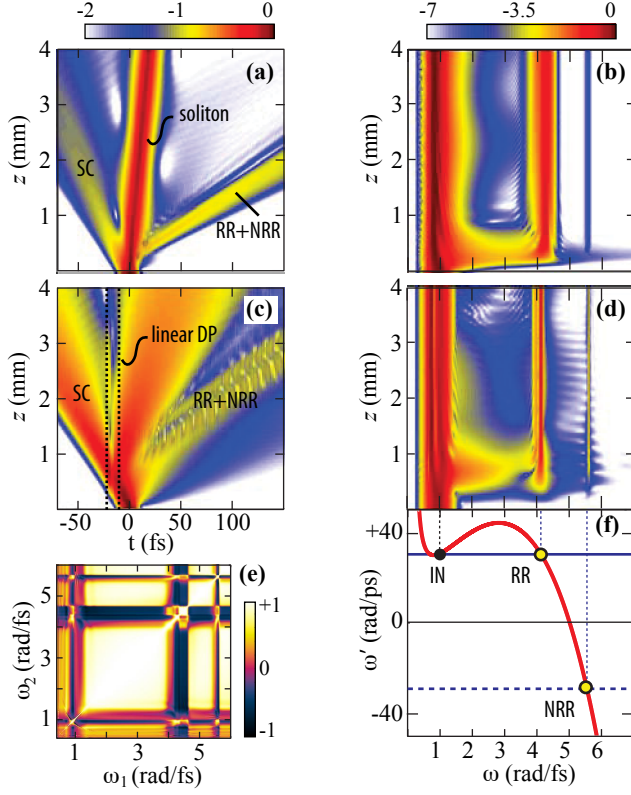


Figure 4.3: Soliton-induced scattering dynamics in fused silica. Comparison between a soliton-induced (via the *nonlinear* Kerr effect) DP (a)-(b) and the “toy-model” DP with the same shape as the soliton-induced inhomogeneity, in a purely linear medium (c)-(d). Envelope (left hand side), and spectral (right hand side) evolution in propagation. Propagation cross-correlation map for the nonlinear case (e). Theoretical positions of input (IN) and resonant (RR, NRR) modes on the comoving dispersion curve $\omega' = \omega'(\omega)$, indicated with filled circles (f).

modes. Figure 4.3(e) shows the propagation cross-correlation Eq. (4.1) for the nonlinear case. Here too, the map shows obvious signs of correlation between the resonant modes. The not so perfect anti-correlation with the input mode may be explained as due to the soliton spectral recoil towards redder frequencies.

4.2.1 Probe scattering from a soliton-induced DP

Finally, we consider the case in which the soliton is accompanied by a second, delayed probe pulse. This second pulse is much weaker and therefore

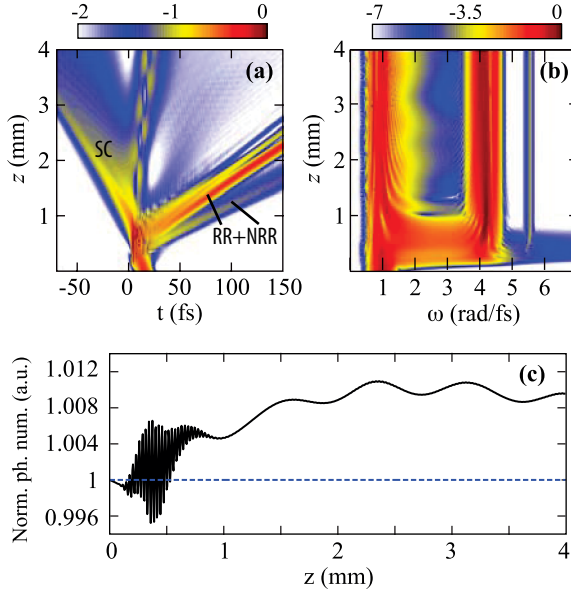


Figure 4.4: Weak probe scattering in fused silica, from the soliton-induced DP of Fig. 4.3(a)-(b). Probe envelope (a) and spectral evolution in propagation (b). Normalised photon number evolution (c) for the probe (black solid curve) and for the soliton (blue dashed curve).

does not form a soliton or excite any nonlinear Kerr effects. Figure 4.4 shows the results for a $1.9 \mu\text{m}$ central wavelength probe pulse, pulse width 8 fs and input intensity $5 \times 10^9 \text{ W/cm}^2$. The probe pulse is scattered by the soliton induced DP shown in Fig. 4.3(a)-(b). The initial probe pulse delay, $t_0 = 15$ fs, is adjusted such that it encounters the soliton when it forms the steepest shock-front and is then scattered relatively efficiently, simultaneously spectrally recoiling to a slightly red-shifted wavelength and emitting two blue-shifted RR and NRR modes.

In Fig. 4.4(c) we show the overall photon number evolution for the probe pulse (black solid line) and for the soliton pulse (blue dashed curve). In order to highlight the cross-scattering dynamics, the two curves have been normalized at each propagation distance with respect to two independent simulations for the probe and soliton pulses alone. We thus note that the overall probe pulse photon number increases by nearly 1%, followed by some weaker oscillations that are originating from a remnant of the probe pulse that is trapped and thus continuously interacts with the soliton [see

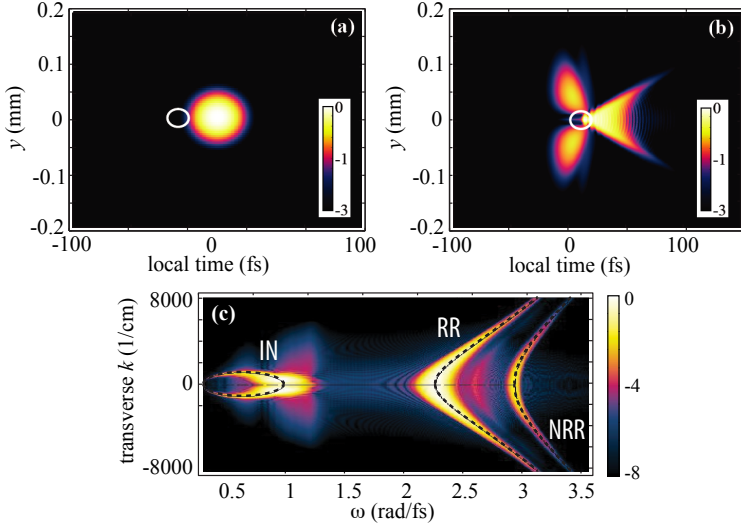


Figure 4.5: 2D numerics of linear scattering from a spatially localized DP. Near field (z, y) profiles of the electric field amplitude at the input (a) and (b) and after $z = 3$ mm propagation (in logarithmic scale). The white circle indicates the position and dimensions of the scatterer ($\delta n = 0.005$, $v = 0.995 c/n$.) The angular spectrum (ω, k_{\perp}) in (c) clearly shows that light concentrates around three distinct spectral features that correspond very precisely to the ω_{IN} , ω_{RR} and ω_{NRR} modes, as predicted by the theory (dashed lines).

Fig. 4.4(a), trapped light is visible for $z > 1.5$ mm, around $t \sim 0$ fs]. This clear photon number increase thus indicates that soliton-induced scattering in this regime, very differently from standard cross-phase modulation, may lead to true amplification of the weaker pulse.

4.3 Two-dimensional scattering numerics

Although the results presented so far were limited to the 1-dimensional case, they are far more general and apply also to higher dimensions. For example in Fig. 4.5 we show a numerical result for a linear scattering process in 2-dimensional space, e.g. a planar waveguide. The host medium is diamond. With respect to the 1D simulations, a single transverse spatial dimension, y is also included. The input pulse has a Gaussian profile with $1/e^2$ width, $\sigma_y = 34 \mu\text{m}$ and input wavelength $2.5 \mu\text{m}$. The scatterer has speed $v = 0.995 c/n(\omega_{\text{IN}})$, is also taken with a Gaussian profile with $1/e^2$ width $\sim 10 \mu\text{m}$ and maximum δn amplitude of 0.005.

Figure 4.5 shows the spatio-temporal near field profiles of the laser pulse at the input (a) and after 3 mm propagation (b). The white circle indicates the position and shape of the DP. The angular spectrum (c) is shown after 3 mm of propagation in (ω, k_{\perp}) coordinates, where k_{\perp} is the transverse wave-vector (proportional to the emission or scattering angle). A precise relation is predicted between ω and k_{\perp} , namely the conical X-wave dispersion relation Eq. (1.24). This is based on the simple identity $k_{\perp} = \sqrt{k(\omega)^2 - k_z^2}$ and $k_z(\omega) = k(\omega_{\text{IN}}) + (\omega - \omega_{\text{IN}})/v$, i.e. the momentum conservation relation that must be satisfied along the z -propagation direction [53]. These relations are plotted, for the parameters given, as dashed lines in Fig. 4.5(d). As for the 1D case, the output frequency ω is allowed to run over both positive and negative values. Alongside the positive valued hyperbolic branch, a second branch is found also at negative frequencies (corresponding to the single NRR point in the 1D case) that matches perfectly with the observed spectrum.

4.4 Gain

From the Manley-Rowe relation Eq. (3.25) derived in this thesis, we found that the resonant scattering from a moving DP contemplates photon number amplification for the total output photons, i.e., $|\text{RR}|^2 + |\text{NRR}|^2 > 1$. It is therefore natural to evaluate the *gain* of the process as a function, e.g., of the input frequency. To this end we set up a series of numerical linear “toy-model” simulations in a diamond-like medium, for different input wavelengths. All the other input parameters, e.g. DP velocity v , steepness m and amplitude δn_0 are fixed.

Figure 4.6(a) shows the diamond-like comoving dispersion curve with highlighted the positions of the IN, RR and NRR modes, for different input wavelengths, ranging from 2 – 40 μm (only a few points are plot for clarity). The output spectra are shown in Fig. 4.6(b) for increasing input wavelengths. We note that, for $\lambda \rightarrow \infty$, which means for ω or $\omega' \rightarrow 0$, the output modes come closer and the efficiency of the process seems increasing. In order to quantitatively evaluate this efficiency we define the gain as:

$$\mathcal{G} = |\text{RR}|^2 + |\text{NRR}|^2, \quad (4.3)$$

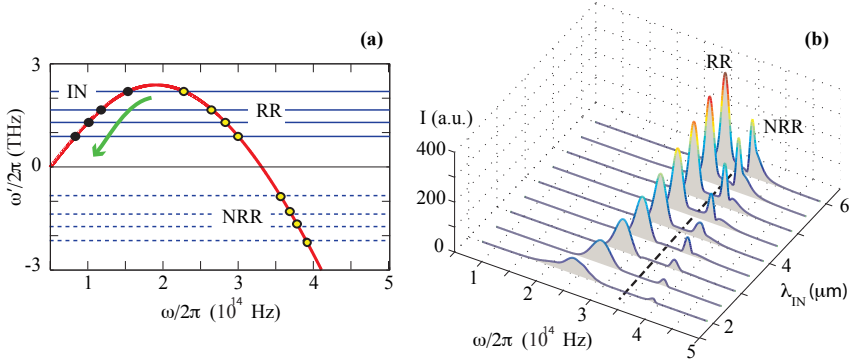


Figure 4.6: Diamond-like comoving dispersion (a) and output spectra for increasing input wavelengths (b). Gain increases in the direction of the green arrow, i.e. for $\omega' \rightarrow 0$.

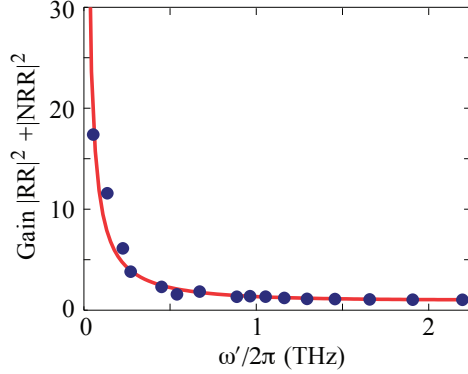


Figure 4.7: Gain \mathcal{G} versus comoving input frequency, evaluated from the linear numerics of Fig. 4.6 (blue circles) with superimposed the fit $y \sim 1/x$ (red curve).

being $|RR|^2$ and $|NRR|^2$ the output photon numbers of each resonant mode, normalized to the input photon number $|IN|^2$. In Figure 4.7 we plot the gain $\mathcal{G}(\omega')$ as a function of the input comoving frequency. Surprisingly we find that the gain diverges for $\omega' \rightarrow 0$, i.e.,

$$\mathcal{G} \sim \frac{1}{\omega'},$$

as demonstrated also by the best fit (red curve) superimposed to numerical data (blue circles).

Summarizing, we have shown that moving DPs scatter light to higher frequencies in an unusual way: they amplify light by the mixing of positive

and negative frequencies, as we describe using a first Born approximation and numerical simulations. Likewise, if the probe pulse were to be reduced to the level of quantum fluctuations, we may expect to see the DP excites the vacuum states. In Chapter 6 we shall demonstrate that the motion of photons in the vicinity of a moving DP may also be described in terms of an effective *curved space-time metric* [77, 78]. We therefore expect that measurements of vacuum fluctuations excited by a DP would give an experimental direct window into the physics of the quantum vacuum in curved space-times [68, 12, 13]. These results therefore open the perspective for novel all-optical control schemes that may be implemented in a wide variety of geometries and applications together with a novel numerical and experimental approach for the investigation of fundamental phenomena.

Chapter 5

Experiments: Negative Resonant Radiation

In this Chapter we shall present direct experimental confirmations of the negative frequency mode generation that we have theoretically and numerically investigated in the previous chapters. The negative RR mode is predicted to arise, alongside the RR mode, from a linear scattering process fed by a moving perturbation. In Sec. 5.1 we describe possible experimental realizations of the moving DP. We performed two sets of experiments in order to capture the formation of the NRR mode: in a bulk medium (Sec. 5.2) and in a few-millimeter-long photonic crystal fiber (Sec. 5.3). In Sec. 5.4 we reports on preliminary measurements in diamond, where we seed the resonant scattering process with THz radiation which is expected to enhance the photon number amplification. The measurements reported in this Chapter were taken in the following laboratories: at the Heriot-Watt University of Edinburgh (Sec. 5.2), at the University of S. Andrews (UK) by the group of Prof. Ulf Leonhardt (Sec. 5.3) and at INRS-EMT of Montreal (Canada) in the UOP group of Prof. Roberto Morandotti (Sec. 5.4).

5.1 Creating an effective moving medium with light pulses

There are various methods by which the Kerr medium may be excited to induce a moving DP. However, successful measurements of negative resonant

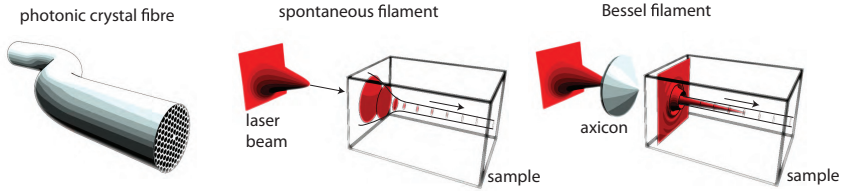


Figure 5.1: Sketch of three different methods employed to generate intense laser pulses with quasi-stationary propagation over long distances. Photonic crystal fibers have micro-structured cores that allow to both tightly confine light and control the material dispersion. Spontaneous filaments are obtained by loosely focusing an intense laser pulse in a bulk Kerr medium, e.g. fused silica glass, while Bessel filaments are generated by pre-shaping the input Gaussian pulse with an axicon.

radiation do impose some additional constraints:

- The intensity profile should be stationary during propagation in order to recreate stationary excitation conditions. This is not a trivial requirement due to the fact that the same Kerr effect that generates the perturbation also leads to back-reaction on the pump laser pulse and detrimental effects such as pulse splitting, self-focusing and white light generation;
- Similarly to the RR mode, the negative mode will only be excited if a sufficiently steep shock front is formed within the pump pulse, as predicted by the “revisited first Born approximation” Eq. (3.22). This condition guarantees that the pulse contains spectral components at sufficiently blue-shifted frequencies to actually seed both RR and NRR generation. The NRR, which is even further blue-shifted with respect to RR, thus requires even steeper shock fronts;
- The velocity of the perturbation, v , plays an important role in the momentum conservation condition, Eq. (3.4), that selects the spectral position of the resonant frequencies, thus, ideally, we would also like to control it.

Bearing this in mind, a few experimental setups have been proposed and are summarized in Fig. 5.1.

5.1.1 Soliton in photonic crystal fibers

The simplest scenario in which these effects may be observed is within the initial stages of optical soliton propagation in highly nonlinear photonic crystal fibers (PCF): a steep shock front develops that may efficiently scatter into relatively intense positive and negative RR. PCFs are fibers with micro-structured cores that on the one hand allow one to tightly confine light within the core region, so as to increase the pulse intensity and amplitude of the perturbation and on the other allow to engineer the dispersion relation and thus the group velocity of the stationary soliton. The maximum perturbation amplitude, δn_0 , generated by these solitons is usually of the order of 10^{-4} . NRR generation in PCF is reported in Sec. 5.3.

5.1.2 Spontaneous filaments

Another option is to attempt to harness the nonlinear propagation of laser pulses in bulk media, e.g. the *spontaneous filament*, whose properties have been extensively described in Section 1.3. In fused silica the self-steepened trailing daughter pulse may generate a perturbation of amplitude $\delta n_0 \sim 10^{-3}$. In Chapter 6 we shall report on spontaneous photon emission from ultrashort laser pulse filamentation in Kerr media.

5.1.3 Bessel filament

A further possibility is the use of *Bessel filaments*. In this case the transverse profile of the input Gaussian laser beam is re-shaped into a Bessel-like pattern using a conical lens (also called axicon). The axicon transforms the laser beam by redirecting light along a cone at an azimuthally symmetric angle θ towards the optical axis, z . The angle θ of the output Bessel beam is related to the axicon base angle α by Snell's law of refraction that gives the relation $n_{\text{air}} \sin(\theta + \alpha) = n_{\text{axicon}} \sin \alpha$, where n_{air} and n_{axicon} are the refractive indices of the surrounding medium (usually air) and of the axicon material (typically fused silica), respectively. Light propagating towards the axis will therefore interfere and the resulting interference pattern will be a non-diffracting Bessel pattern (see the sketch in Fig. 5.2). Using the fact that the input pulse is Gaussian, it is also possible to determine the evolution of the peak intensity along the propagation direction z [79]:

$$I(z) = I_0 2\pi k_0 z \tan^2 \theta e^{(z^2 \tan^2 \theta)/w_0^2} \quad (5.1)$$

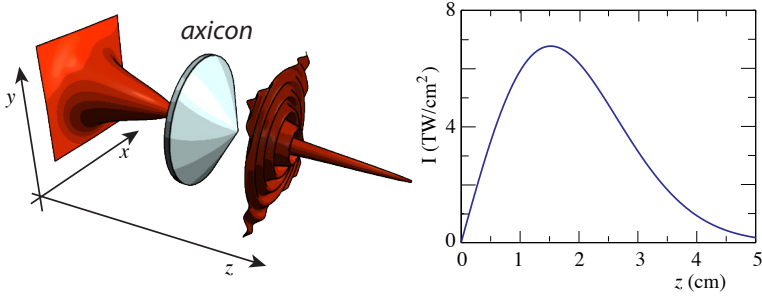


Figure 5.2: Sketch of Bessel beam generation with an axicon (left) and a Bessel intensity profile $I(z)$ along propagation (right).

where I_0 and $\sqrt{2}w_0$ are the input Gaussian peak intensity and radius at $1/e^2$. A plot of Eq. (5.1) is shown in Fig. 5.2 which gives the peak intensity for an input Gaussian pulse of 1 ps duration, $w_0 = 5$ mm and $I_0 = 1$ GW/cm^2 . Moreover, simple geometric considerations show that the high intensity interference peak propagates along the z -axis with velocity

$$v = \frac{v_g}{\cos \theta},$$

where v_g is the input Gaussian pulse group velocity. Therefore, by simply changing the angle of the axicon, it is possible to control the propagation velocity of the Bessel pulse. Contrary to the spontaneous filament, the Bessel filament allows direct control of both pulse velocity and peak intensity. However, if the Bessel filament is generated with an axicon, v may only be made larger than v_g whilst the spontaneous filament delivers two pulses, one faster and the other slower than v_g . Finally, an important feature of Bessel pulses is the possibility to strongly suppress or even completely eliminate the modulation instability and the formation of supercontinuum [81].

As an example (see Ref. [80]), in Fig. 5.3 we show the real (δn , left-hand side) and imaginary ($\delta \kappa$, right-hand side) components of the total refractive index variation induced by an high-angle Bessel beam (cone angle $\theta = 7$ deg in water), for different input pulse energy conditions, and compared with a Gaussian pulse, focused (in water) with the same numerical aperture of the axicon ($\text{N.A.} \sim 0.11$). Plasma generation was characterized by a holographic microscopy technique. We observe that the Gaussian pulse

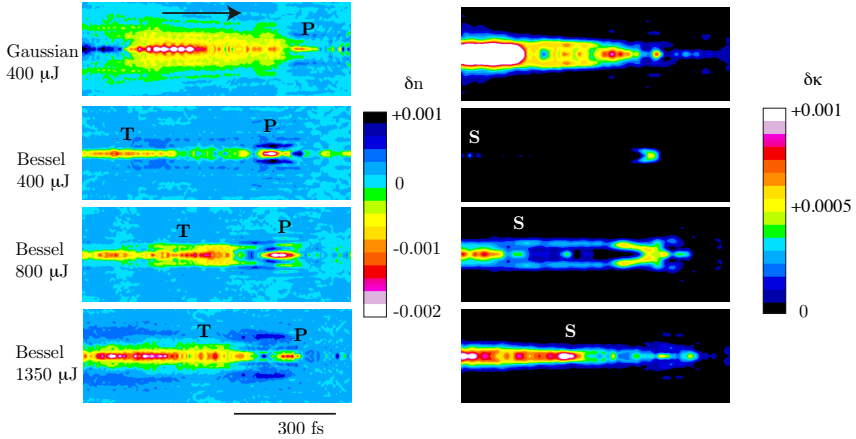


Figure 5.3: Measured refractive-index variations (real part, δn , in the left hand panel; imaginary part, $\delta \kappa$, in the right hand panel) induced by the laser pulse under the input conditions (beam profile and energy) as indicated in the figure. P indicates the pulse position, T the solvated electron tail and S the position of the onset of thermalized solvated electron-induced absorption. Figure from Ref. [80].

generates very intense white light, even at the lowest energies, while the axicon focusing generates no observable spectral broadening even at the high 1 mJ energies, indicating a strong suppression of the Kerr-induced temporal and spectral dynamics (e.g., self-phase-modulation and self-focusing). Moreover we find the Bessel beam induces a δn that is roughly two times larger than that of the Gaussian beam.

For the experiments reported in this Chapter, the ability to suppress any background or spurious radiation is extremely important in order to measure background-free signals. This suppression is obtained by placing the nonlinear Kerr medium as close as possible to the axicon so as to enter the medium with as low an intensity as possible. The Bessel peak intensity then grows slowly inside the sample and modulation instabilities are not amplified so that the pulse propagates without significant spectral or temporal distortion [82]. This specific propagation regime was adopted for the experiments reported in both Sec. 5.2 and Chapter 6.

5.2 NRR in bulk calcium fluoride

In the first experiment, we chose a 2-cm-long bulk calcium fluoride sample (CaF_2) as host material (the nonlinear Kerr coefficient is reported in Table

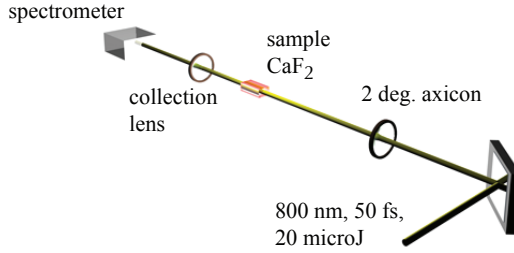


Figure 5.4: Experimental setup for NRR generation in CaF₂.

1.2). This material was specifically chosen due to the significantly lower dispersion with respect to common fused silica glass [19]. Indeed this allows a wider spectral broadening in the UV spectral region and consequently the formation of steeper shock fronts which is an important requirement for efficient NRR generation, derived by the first Born approximation analysis of Section 3.2. We hence find that the use of low-dispersion media was beneficial for these measurements.

5.2.1 Experimental setup

The experimental layout for the Bessel-pulse measurements is shown in Fig. 5.4. Light pulses of 60 fs duration and 800 nm carrier wavelength are provided by an amplified Ti:sapphire laser system of 1 kHz repetition rate. Under these conditions (3D geometry), we do not excite a soliton, but the nonlinearity will nevertheless excite a resonant instability that is governed by the same physics — and by Eq. (3.4) — as RR in optical fiber solitons. We reshape the pulses into Bessel beams with a cone angle (in the medium) of $\theta = 0.6$ degrees, using a fused silica axicon with $\alpha = 2$ deg base angle. The Bessel-beam geometry plays an important role in the sense that it creates a localized and extended high-intensity interaction region. The spectrum at the output of the sample is collected with a lens and a fiber-based spectrometer. A filter with a flat response in the visible-near-UV region is placed before the spectrometer in order to reduce the input pump intensity without affecting the shape of the spectrum between 300 – 720 nm. The input pulse energy is varied from 10 – 50 μJ , at which point the input pulse is in a strongly nonlinear regime and develops a complex and structured spectrum. Generation of negative RR modes is observed at intermediate energies $\sim 15 \mu\text{J}$, where the maximum amplitude of the

DP, estimated from the nonlinear Kerr index of CaF_2 is $\delta n = n_2 I \sim 0.002$. The IN mode is supplied by the pump pulse itself, which scatters from the self-induced perturbation towards the resonant modes RR and NRR.

5.2.2 Experimental data and numerics

Examples of the resulting spectra for varying input energies are shown in Fig. 5.5. The spectra are vertically displaced in order to render them visible. At lower energies ($12\text{--}14\ \mu\text{J}$) the output spectrum shows a distinct single peak that shifts to shorter wavelengths with increasing input energy. This process has been described in detail [54] in similar conditions and is a direct manifestation of the formation of a steep shock front on the trailing edge of the pump pulse. As energy is increased, the shock front steepens and the spectral peak shifts toward shorter wavelengths. Between 15 and $20\ \mu\text{J}$ input energy, a different regime sets in, characterized by two distinct peaks in the spectrum that do not shift with increasing energy. The first peak is located around $620\ \text{nm}$; the second is much weaker and is located around $341\ \text{nm}$ wavelength. Examples of these spectra (15 and $16\ \mu\text{J}$) are shaded in red in the figure. At higher input energies, the pulse starts to develop complex dynamics, typical of the filamentation regime, during which the pulse breaks up and creates a broad-band, highly structured spectrum known as supercontinuum [26].

We focus our attention, for example, on the spectrum measured for an input energy of $16\ \mu\text{J}$: the spectrum is not substantially modified if we account for the filter response, as shown in the inset to Fig. 5.5(a). Three clear peaks are indicated with λ_{IN} , λ_{RR} and λ_{NRR} , and we identify these with the IN, RR, and negative RR modes, respectively. Indeed, these peaks correspond exactly to the positions for the RR and NRR modes given the IN mode and the dispersion relation for CaF_2 , as shown in Fig. 5.5(b). We note that attempts to generate similar features in other glasses or media (e.g., BK7, fused silica, and water) failed. Spectral broadening through self-phase-modulation and the steepness of Kerr-induced shock fronts are both strongly limited by dispersion. Our experiments in fused silica and water (data not shown) showed that even at the highest input energies, spectral broadening exhibited a sharp cutoff around $\sim 450\ \text{nm}$, whereas the negative RR peak was, in all cases, predicted to appear at shorter wavelengths. On the other hand CaF_2 (as other fluoride glasses) is quite

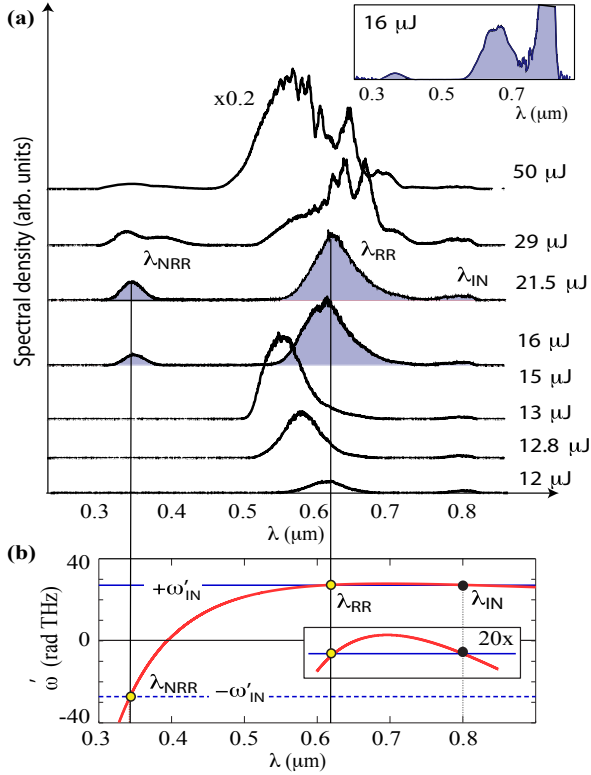


Figure 5.5: Experimental results for NRR generation in bulk CaF_2 . (a) Measured spectra for increasing input energies (indicated next to each curve). The spectra are vertically displaced to increase visibility. The inset shows a sample spectrum (16 μJ input energy) corrected for the filter response. (b) CaF_2 dispersion relation in the comoving frequency versus laboratory-frame wavelength coordinates (ω' , λ), with the predicted positions of the RR and NRR spectral peaks. The inset is a 20 \times enlargement of the curve around the RR wavelength.

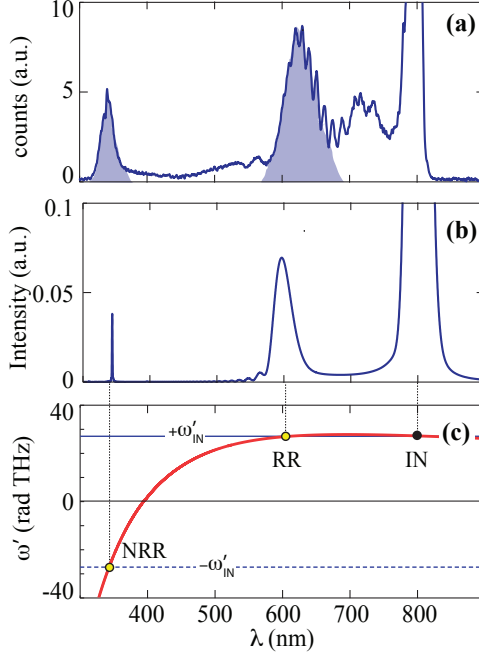


Figure 5.6: Experimental measurements from Fig. 5.5, input energy $\sim 15 \mu\text{J}$ (a) and comparison with numerics (b) and theory (c).

unique, as it exhibits significantly lower dispersion [19], in particular in the UV spectral region, and thus allows the formation of steeper shock fronts and broader continua. In this specific case, it allows a relatively efficient excitation of the NRR peak in the ultraviolet region.

In Figure 5.6 we compare the experimental data of Fig. 5.5, input energy $\sim 15 \mu\text{J}$, with a 1D+1 (time t and propagation coordinate z) *linear* numerical simulation, as described in Section 4.1, using a quadratic dispersion relation that fits the dispersion curve of CaF_2 in the relevant experimental spectral range. We underline that a perfect agreement cannot be expected due to the fact that the numerical simulations do not account for the full 3D+1 geometry of the experiment nor do they account for any nonlinear effects such as cross-phase modulation between the pump pulse and the newly generated RR and NRR modes [21]. Nevertheless, the “toy-model” based on linear propagation in 1D+1 geometry is able to capture the essential features of the frequency conversion process observed in the experiments, thus lending further evidence of negative frequency generation.

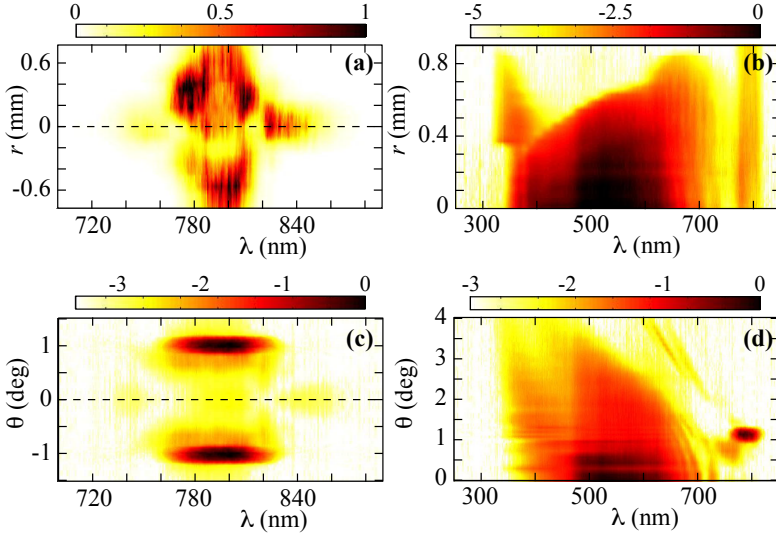


Figure 5.7: Near-field (r, λ) and far-field (θ, λ) spectra (external angles) of Bessel pump and RR in CaF_2 . Near-field spectra for pump, lin-scale (a), and resonant radiation, log-scale (b), with the corresponding far-field spectra for pump and RR, log-scale (c)-(d), respectively.

5.2.3 Far-field spectra

As a further analysis, we want to study the spatial and angular distribution of the resonant radiation (RR+NRR) generated by the Bessel pump in the 2-cm-long CaF_2 sample. Figure 5.7 shows the experimental data for pump (left-hand) and resonant modes (right-hand), for a pump input energy of $\sim 20 \mu\text{J}$. The near-field (r, λ) spectra were acquired with the fiber spectrometer in the image plane of a 100-mm-long focal length lens, by manually scanning the fiber transverse r -position (scan step $\sim 20 \mu\text{m}$). A series of neutral density filters were employed to avoid damage of the fiber. The set of spectra at different r -positions were then processed together to obtain the image of Fig. 5.7(a)-(b). The same procedure was adopted for the angularly resolved (θ, λ) spectra of Fig. 5.7(c)-(d), acquired in the focal plane of the 100-mm focal length lens, in the far-field configuration with respect to the output facet of the CaF_2 sample. Angles θ in the Figure are to be understood as external angles (i.e. in air), which are linked to the internal propagation angles θ_i by the Snell law of refraction: $\theta = \arcsin(n_{\text{caf}} \sin \theta_i / n_{\text{air}})$. With $n_{\text{air}} = 1$, $n_{\text{caf}} = 1.4305$ (at 800 nm) and

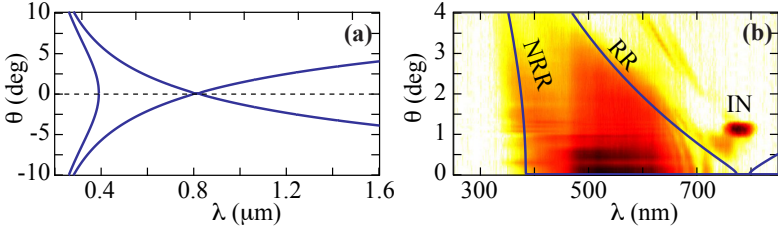


Figure 5.8: Resonant radiation X-wave fit. (a) Best fit with the X-wave relation (1.24) for $v = 2.0838 \times 10^8$ m/s, and (b) superimposed to the measured far-field spectra of Fig. 5.7(d).

$\theta_i = 0.65$ deg, $\theta \sim 1$ deg, as visible in both Figures 5.7(c)-(d). We note that the internal cone angle θ_i is slightly larger than the nominal value (~ 0.6 deg) derived from the base angle of the fused silica axicon adopted to generate the Bessel pulse, as discussed above.

The pump spectra show, in both the (r, λ) and (θ, λ) domains, clear evidence of *unbalanced* Bessel filamentation, as reported by Polesana et al. in [81, 82]. In particular the presence of the two side-bands peaks (at ~ 745 and ~ 840 nm) reveals phase-matching on-axis due to the Bessel pulse nonlinear propagation regime. Interestingly, the spatially resolved spectrum in Fig. 5.7(b) reveals that for a fixed position, e.g. $r = 700$ μm , only the NRR peak at ~ 350 nm is clearly distinguishable from the supercontinuum.

Finally, in Figure 5.8 we tried to fit the (θ, λ) spectrum of Fig. 5.7(d) with the theoretical X-wave dispersion relation Eq. (1.24),

$$k_{\perp}(\omega)^2 = k^2(\omega) - \left(\beta + \frac{\omega - \omega_0}{v} \right)^2,$$

with ω spanning from negative to positive values and where the propagation angle θ is linked to the transverse wave vector component as $k_{\perp}(\omega) = k(\omega) \sin \theta(\omega)$. The best fit in Fig. 5.8(a) is superimposed to the measured angular spectrum in (b). The perturbation velocity v was derived by the measured external angle, i.e. $v = v_g / \cos \theta \sim 2.0838 \times 10^8$ m/s, being v_g the Gaussian pulse group velocity at 800 nm, $v_g = 2.0835 \times 10^8$ m/s. We note that the fit is not perfectly superimposed to the measured spectrum; nevertheless, work in this direction is still ongoing in order to acquire more precise angular spectra. Even so, the far-field measurements presented

here provide a very good idea of the spatial and angular distributions of the resonant radiation generated by a Bessel-like pump.

5.3 NRR in photonic crystal fiber

In a second experiment, we sent 7 fs light pulses, centered around 800 nm, with a 77 MHz repetition rate, into a fused silica photonic-crystal fiber (that has anomalous dispersion at 800 nm). PCFs have the advantage of enhanced nonlinear effects due to tight mode confinement, combined with a remarkable flexibility in tailoring the waveguide dispersion, that can therefore strongly modify the corresponding bulk medium dispersion and, thus, allow observation and control of a variety of novel effects. We selected fibers where the spectrum of the incident light lies in a region of anomalous group-velocity dispersion such that it can propagate as a soliton-like pulse.

Figure 5.9 shows the output spectrum after 5 mm of fiber for three different input energies (246, 324, and 366 pJ). The UV part of the spectrum [Fig. 5.9(a)] was measured with a monochromator and a photomultiplier tube. It shows a clear peak that we identify with the negative RR mode. The part of the output spectrum that lies in the visible range, shown in Fig. 5.9(b), was measured with a compact CCD spectrometer. The peak observed here corresponds to the RR: the frequency of this mode shifts to shorter wavelengths with increased input pulse energy due to the nonlinear modification of the refractive index from the pulse, Eq. 2.9. Figure 5.9(c) shows the predicted RR and negative RR frequencies based on the dispersion relation for the PCF. The measured peaks at λ_{RR} and λ_{NRR} are, similarly to the bulk measurements, the main spectral features in the whole spectrum and both correspond very precisely to the predictions. We note that the NRR peak does not shift noticeably with input energy because the nonlinear refractive index change from the pulse is negligible compared to the dispersive index changes in the UV. Experiments were also repeated for a series of PCFs, with different dispersions, and in each case the measured resonant peaks correspond precisely with the theoretical predictions.

In closing, we note that the NRR measurements in both bulk and PCF may not be explained in terms of four-wave mixing (FWM) between the RR and IN modes, as a simple calculation shows that this would generate a blue peak at 230 nm and 180 nm in the bulk and fiber case, respectively.

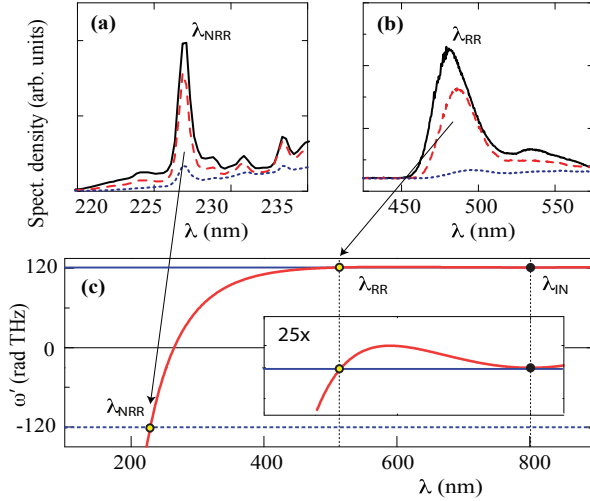


Figure 5.9: Experimental results for NRR generation in a photonic-crystal fiber. (a)–(b) Measured spectra in the visible and UV regions for three different input energies: 246 pJ (dotted line), 324 pJ (dashed line), and 366 pJ (solid line). (c) Full fiber dispersion relation: positions of the predicted λ_{RR} and negative λ_{NRR} spectral peaks are indicated. The inset is a $25\times$ enlargement of the curve around the RR wavelength.

5.4 NRR seeded with THz

So far we have studied only the “self-seeded” resonant scattering mechanism, in which an intense laser pump is scattered by a self-induced moving perturbation of the refractive index, and we have reported on efficient NRR generation in both bulk CaF_2 sample and in photonic crystal fibers. Now we want to move a step forward in the study and understanding of the resonant scattering process.

In this third experiment (carried on at the ALLS facility of the INRS-EMT research center of Montreal, Canada) we probe the scattering process with an external weak seed, as described in Sec. 4.2.1. We decide to probe the process as close as possible to the “zero-frequency” mode as, in this regime, maximum gain is predicted by the preliminary numerical studies presented in Sec. 4.4. Diamond is the perfect candidate, showing negligible absorption both in the terahertz and in the far-infrared bandwidth. Indeed diamond dispersion, contrary to e.g. fused silica or CaF_2 , exhibits no resonances in the IR spectral region and passes through the $(\omega', \omega) = (0, 0)$

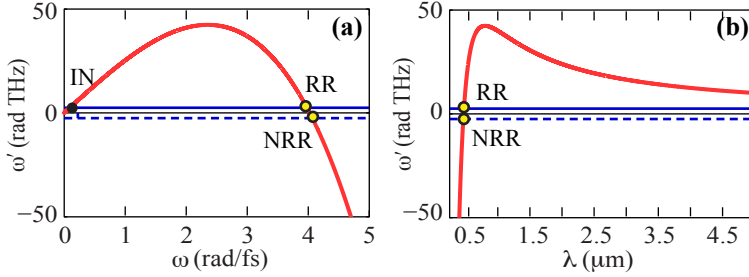


Figure 5.10: Diamond dispersion curves in (ω', ω) coordinates (a) and (ω', λ) coordinates (b), in the reference frame comoving with a perturbation travelling at $v = 1.2286 \times 10^8$ m/s, which is the group velocity of an 800 nm carrier wavelength Gaussian pulse in diamond. The two resonant modes (RR and NRR) would be generated around $\lambda_0 = 468$ nm.

point, thus allowing efficient seeding for $\omega' \rightarrow 0$ [see Figure 5.10(a)-(b)].

5.4.1 Experimental setup

A sketch of the experimental setup is depicted in Fig. 5.11. We generate the moving perturbation, DP, with an intense 800 nm Gaussian pump pulse (pulse duration 70 fs, input energy $1 \mu\text{J}$), focused over an area of radius $\sigma_x \sim 10 \mu\text{m}$ into a $500 \mu\text{m}$ long diamond sample. The Kerr induced variation of the refractive index, $\delta n = n_2 I$, is estimated to be of the order of ~ 0.005 , being $n_2 = 12.6 \times 10^{-16} \text{ cm}^2/\text{W}$ the nonlinear index of diamond (Table 1.2). The moving scatterer is then probed with a co-propagating THz radiation, which has been slightly focused in the sample so as to enhance spatial overlap with the pump. The temporal overlap is ensured with a remotely controlled delay-line on the pump path. After the filter, the output resonant radiation is collected with the spectrometer. The theoretical positions of the resonant frequencies are predicted from the diamond comoving dispersion curve in Fig. 5.10(a)-(b), for a perturbation velocity $v = v_g$ with v_g the 800-nm-carrier-wavelength Gaussian pump group velocity in diamond: $v_g = 1.2286 \times 10^8$ m/s. Since the two resonant modes (RR and NRR) are so close to each other (spectral separation ~ 9 nm), we expect to actually measure a single intense resonant peak around the zero-comoving-frequency, i.e. at $\lambda_0 = 468$ nm.

As a THz pulse source we employ the setup developed by Clerici et al. and explained in detail in [83]. The $1.8 \mu\text{m}$ output wavelength from a com-

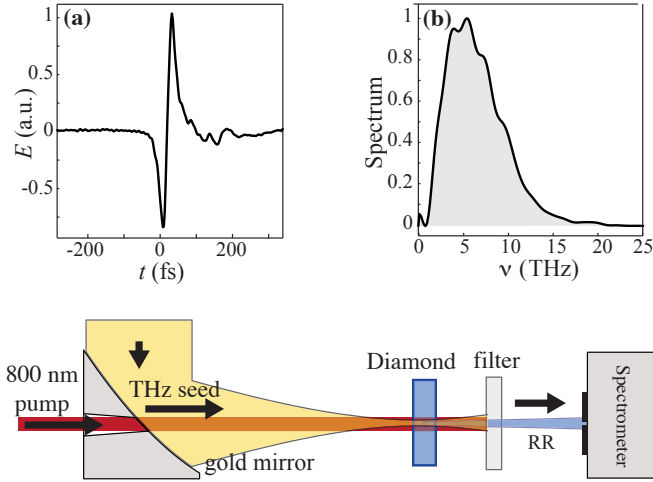


Figure 5.11: THz pulse seeding for NRR generation in diamond. (a) Instantaneous electric field and (b) power spectral density for the terahertz pulse employed as seed in our experiments; sketch of the experimental setup below. Figure adapted from Ref. [84].

mercial optical parametric amplifier (OPA) is focused in air together with its second harmonic generated by a frequency doubling crystal. Figures 5.11(a)-(b) show the THz instantaneous electric field and power spectral density, respectively, delivered by the terahertz source and employed as seed in our experiments. We note that the THz spectrum is peaked at $\nu_{\text{IN}} = 6$ THz (corresponding to a $\lambda_{\text{IN}} = 50 \mu\text{m}$) with a bandwidth sustaining a pulse of ~ 90 fs duration.

5.4.2 Experimental results

Figure 5.12 shows the measured output spectrum in logarithmic-scale with (red curve) and without (blue curve) the THz seed. The spectral broadening of the pump (SC) reaches 500 nm, while generation of radiation (RR) seeded by the THz pulse is evident around 430 nm. The peak at ~ 400 nm is the so-called electric field induced second harmonic (EFISH), resulting from a four-wave mixing interaction between the 800 nm pump pulse and the THz wave (see e.g. [84] and references therein). The new peak at 430 nm may not be explained as electric field induced SH generation, being too far from the phase-matching condition of this process. Still, we note that

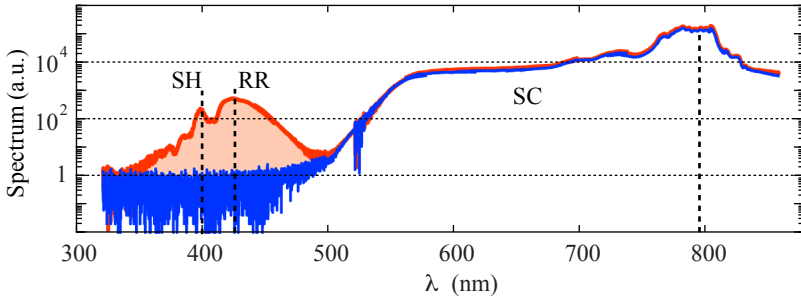


Figure 5.12: Measurements in diamond: overall spectrum (log-scale) from pump pulse at 800 nm down to the ultraviolet spectral region, with (red curve) and without (blue curve) THz seed. SH is the electric-field-induced second harmonic and RR is the resonant radiation at ~ 430 nm, seeded by the THz pulse. SC is the supercontinuum generation from the pump.

the spectral position of the RR peak is further blue-shifted with respect to the theoretical prediction of Fig. 5.10, which was expected to be around 468 nm. We explain this shift as due to the highly nonlinear propagation dynamics of the intense Gaussian pump, which may form a steep shock front that slows down till $v \sim 1.222 \times 10^8$ m/s. Preliminary 1D UPPE numerical simulations (see Sec.5.4.3) go in this direction, although a full 3D theoretical model for nonlinear propagation in diamond (which accounts, e.g., also for plasma effects and nonlinear absorption) is still missing.

In Figure 5.13 we report additional measurements for characterizing the resonant peak. Fig. 5.13(a) shows the spectrogram, namely the delay-resolved spectrum, between 405 and 465 nm. We note that the peak around 430 nm is a truly different feature with respect to the electric-field-induced SH which lasts for longer delays (until ~ 1 ps) being enhanced by a THz backward-propagation interaction, as demonstrated in [84]. On the contrary, the intense RR peak close to delay zero lasts for ~ 30 fs FWHM, as highlighted by the line-out of the spectrogram at fixed wavelength, $\lambda_0 = 430$ nm, plotted in Fig. 5.13(c). A line-out of the spectrogram at delay zero is shown in Fig. 5.13(d) with highlighted the SH and RR components. As a last analysis, in Fig. 5.13(b) we show the polarization behavior of the resonant radiation (obtained by varying the angle of a polarizer on the beam path), which appears to be polarized as the SH component.

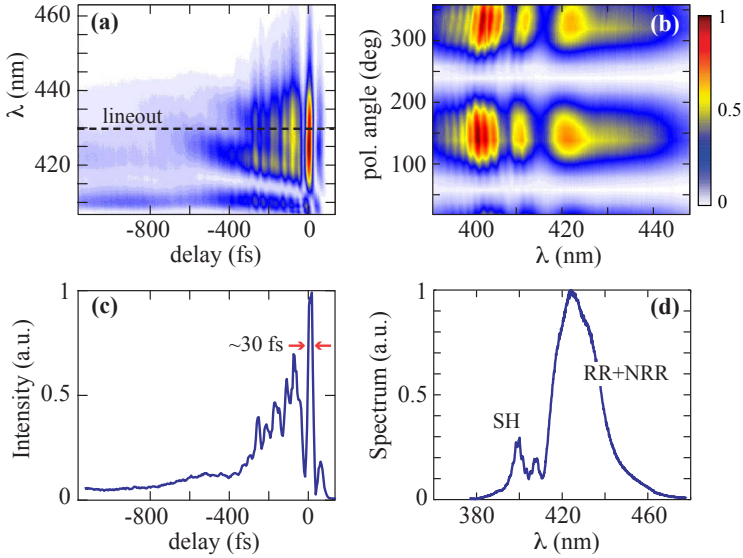


Figure 5.13: Measurements in diamond: spectrogram (a) and polarization of SH and RR (b). Line-out of the spectrogram at fixed wavelength, 430 nm (c), and spectrum at delay zero (d).

5.4.3 Numerics

Finally, we compare the measurements with a linear “toy-model” simulation based on the same UPPE solver used for the numerical results of Chapter 4. The THz pulse is modeled as a single-cycle pulse having $\phi_0 = \pi/2$ carrier-envelope phase (CEP):

$$E = \sqrt{I_0} e^{-(t/t_0)^2} \cos(\omega_{\text{IN}} t - \phi_0),$$

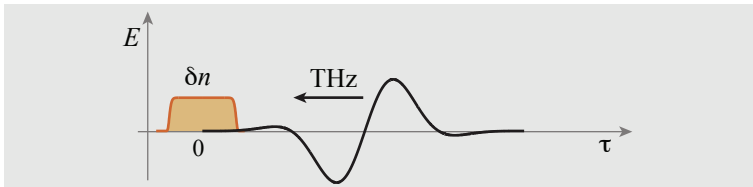


Figure 5.14: Sketch for the configuration adopted in the toy-model numerics of Fig. 5.15: the THz seed is scattered by a co-propagating linear inhomogeneity, δn , having super-Gaussian temporal profile. The local time is $\tau = t - z/v$, with v the perturbation velocity.

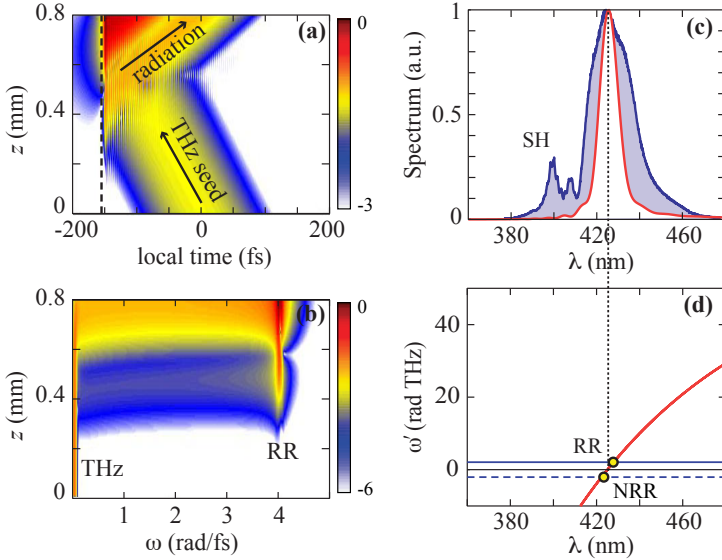


Figure 5.15: Linear numerics for pump-probe scattering in diamond. Envelope (a) and spectral evolution (b) along propagation in log-scale. The input THz pulse is centered at $\lambda_{\text{IN}} = 30 \mu\text{m}$ with pulse duration 40 fs. Comparison between the experimental spectrum of Fig. 5.13(d) (blue shaded area) and the numerical one (red-curve), evaluated at propagation distance $z = 500 \mu\text{m}$. Diamond comoving dispersion curve with the theoretical position of the modes (RR and NRR), predicted for a perturbation velocity $v = 1.22175 \times 10^8 \text{ m/s}$.

with input pulse duration $t_0 = 40 \text{ fs}$ and input wavelength $\lambda_{\text{IN}} = 2\pi c/\omega_{\text{IN}} = 30 \mu\text{m}$. The THz field is launched together with a super-Gaussian shaped DP, $\delta n(t - z/v)$, as defined by Eq. (2.19), moving at velocity $v = 1.22175 \times 10^8 \text{ m/s}$. Figure 5.14 shows a sketch of the scattering configuration at the beginning of the interaction.

The envelope and spectral evolution (log-scale) are shown in Fig. 5.15(a)-(b), respectively, over a propagation distance of $800 \mu\text{m}$ in diamond. In Fig. 5.15(c) we compare the numerically evaluated spectrum (red curve) with the experimental result of Fig. 5.13(d) (blue shaded area). Comparison with the theoretical predictions for the resonant modes (RR and NRR) is plot in Fig. 5.15(d) on the diamond comoving dispersion curve (ω', λ).

Although in a very simplified setting and with slightly different input conditions, the position of the numerically evaluated resonant peak is in perfect agreement with the measured spectrum. The toy-model numerics thus confirm to be able to capture the essential features of the resonant

scattering and transfer of energy. Nevertheless we recall that a full 3D theoretical model is needed which would describe the complete spatio-temporal dynamics occurring during nonlinear propagation in diamond.

Summarizing, we have shown how the same frequency-conversion process that leads to a resonant transfer of energy from an input laser pulse to a typically blue-shifted peak (RR mode), generates a second, so far unnoticed, peak that corresponds to a resonant transfer of energy to the negative-frequency branch of the dispersion relation (NRR mode). The energy transfer is favored in the presence of steep shock fronts or, more generically, by a “nonadiabatic” variation within the pump pulse as also predicted by the first Born approximation developed in this thesis and by the numerical results of Chapter 4. Here we performed experiments in both bulk media and waveguides with optimized dispersion landscapes so as to allow the process to occur with a relatively high efficiency. In the last Section we have reported also on efficient seeding close to $\omega' \rightarrow 0$ regime, experimentally realized with a pump-and-probe experiment in diamond, using THz radiation as seed.

Chapter 6

Implications: optical analogue for gravity

Laser physics and optics in general have the ability to reproduce, even if to a limited extent, many features of the physics of completely different systems. We mention, among others, semiconductor physics and electrons quantum behavior reproduced in photonic crystals and periodic optical waveguides [85, 86]. This also implies that the behavior of light may be understood or reinterpreted using the tools developed in very different fields. In this Chapter we show how the physics of the resonant scattering from a moving DP may be reinterpreted as the classical-limit of the *analogue Hawking radiation* from an optically-induced *event horizon* [11]. We can therefore describe it using the tools of the so-called transformation optics, which describes the optical systems in terms of curved space-time geometries, and general relativity. The Chapter is organized as follows: a very general introduction with an overview of the theoretically predicted features of the analogue Hawking radiation (Sec. 6.1), followed by numerical studies which allow us to verify the predicted *thermality* behavior of the *stimulated* Hawking emission (Sec. 6.2). The last Section 6.3 is devoted to direct experimental evidences of *spontaneous* emission of photons [12, 13] from ultrashort laser pulse filamentation in Kerr media, that are in quantitative agreement with the Hawking model, although have stimulated an ongoing discussion regarding the precise origin of the emission [87, 88, 89].

6.1 Analogue gravity in moving media

“Analogue gravity” is the study of phenomena traditionally associated to gravitation and general relativity, by means of analogue models that can be realized in very different physical systems and that do not directly rely on gravity at all [77]. In the case of the optical analogue, the underlying idea is that the refractive index of a given medium in which light is propagating, acts as a “transformation medium”, i.e. it “transforms” the euclidean space-time in which light rays propagate, into some other *effective curved space-time*. The result is that the light paths followed by the rays appear to be bent and this is a consequence of the effective space-time curvature induced by the medium [90]. A very simple example of this is the optical mirage which also finds a precise mathematical description in terms of Fermat’s principle and which may therefore be considered as a precursor of transformation optics.

When the refractive index perturbation (DP) is set in motion, the propagation of light rays inside the medium can be described, using the tools of general relativity, in terms of an effective metric for which the light ray paths are the null geodesics [77, 11, 91, 92], without any further reference to the original picture involving Maxwell equations. All relevant dielectric properties are reabsorbed in the effective metric which is actually seen by photons. This is in analogy with the description of light rays in the presence of a metric induced by a gravitational body.

Notably, these features also apply to the *quantized* electromagnetic field [93]. In other words, there are certain, fundamental aspects of quantum field theory in the presence of curved space-times [68] that may be investigated using transformation optics [77, 90, 94]. According to a milestone prediction in this sense, astrophysical black holes evaporate, i.e. they emit particles and photons with a blackbody spectrum known as *Hawking radiation* [9, 10]. In 1974 Hawking predicted that the space-time curvature at the event horizon of a black hole is sufficient to excite photons out of the vacuum and induce a continuous flux. In a simplified description of the process, vacuum fluctuation pairs close to the horizon are split so that the inner photon falls in and the outside photon escapes away from the black hole. As the outgoing photon cannot return to the vacuum, it necessarily becomes a real entity, gaining energy at the expense of the black hole.

The particularity of Hawking radiation is that it is predicted to exhibit a *blackbody spectrum* with a temperature given by [10, 95],

$$T_H = \frac{\hbar\kappa}{2\pi ck_B}, \quad (6.1)$$

where \hbar is the reduced Planck constant, c the speed of light in vacuum and k_B the Boltzmann's constant. The *surface gravity* κ may be interpreted as the gravitational acceleration experienced at the horizon. For a black hole $\kappa = c^4/4GM \sim 3 \times 10^{43}/M \text{ m/s}^2$, where G is the gravitational constant and M the mass of the black hole. Therefore, for a solar-mass black hole the temperature is extremely low, of the order of 10 nK, and Hawking radiation has little hope of being detected. On the other hand, it is now widely accepted that Hawking radiation does not actually require a gravitational mass but rather the essential ingredients are a *quantum field*, e.g. density perturbations in a fluid, or the electromagnetic field and an *event horizon* associated with a curved space-time metric that blocks the quanta of this field, namely phonons or photons [77, 96].

Many physical systems that may exhibit event horizons have been proposed as analogue models. We recall, e.g., flowing water [66, 70], Bose-Einstein condensates (BECs) [71, 97, 98], or moving perturbations of the refractive index in a dielectric medium [11, 12, 13] (see also the review paper [77]). All these analogue gravity models are based on the formation of a kinematic horizon induced by a moving background that can be interpreted in terms of a *flow* according to the so-called “river model”, which is based on the fact that the speed of light v_ϕ in a uniform and flowing medium depends on the flow velocity v [99]. The “river model” also provides a direct link with the space-time metric in the presence of an astrophysical black-hole [100, 99]. In 1981 Unruh was the first who proposed an acoustic analogue in order to probe the existence of Hawking radiation in the laboratory [96]. He studied sound waves in a flowing medium which is accelerated so as to pass from a subsonic to a supersonic region. The point at which the flow velocity equals the speed of sound is the sonic event horizon for the sound waves that will be blocked by the counterflow [71].

On the contrary, in the “moving dielectrics” analogue model, that we study here, the medium itself is not flowing at all; rather, all that is necessary is a localized perturbation of the refractive index that travels at speeds close to c . The idea is based on nonlinear and transformation optics and

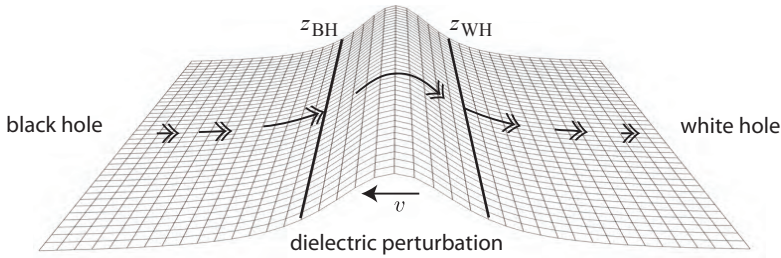


Figure 6.1: The “flowing river” of space for the effective geometry induced by a 1-dimensional DP moving from right to left. In the frame comoving with the perturbation, space flows as shown by the arrows (longer arrows indicate larger velocities). The black hole, z_{BH} , and white hole, z_{WH} , horizons are the points at which space flow becomes equal to $c/(n_0 + \delta n)$. Figure from Ref. [99].

was originally proposed by Leonhardt, Philbin et al. in 2008 [11]. They suggested to use an intense optical soliton pulse propagating in a fiber. As we saw in the first introductory Chapter (and in more detail in Section 1.4), the soliton intensity is sufficient to induce a DP in the fiber medium, through the nonlinear Kerr effect Eq. (1.17),

$$\delta n(z - vt) = n_2 I(z - vt),$$

which is moving at velocity v that is very close to the speed of light in the medium c/n_0 . This in turn acts as a space-time curvature of the metric as seen by the quantum electromagnetic vacuum. Due to material dispersion, the DP will become *superluminal* in the sense that it will move faster than the velocity of sufficiently blue-shifted wavelengths. These wavelengths will therefore be blocked by the DP, i.e. a blocking horizon is formed. Moreover, theoretical predictions suggest extremely high Hawking temperatures in the range of thousands of Kelvins and many orders of magnitude higher than in any other physical system proposed to date.

According to the “river model” an increase in the local refractive index, from a background value $n = n_0$ up to a maximum value $n = n_0 + \delta n$, is equally perceived by light as a local increase in the flow velocity, i.e. both lead to a slowing down of the light pulse. Figure 6.1 illustrates the geometry of a one-dimensional δn perturbation. The arrows indicate the equivalent flow of space: interestingly, the flow of space is such that a single perturbation may recreate the analogue of both a black hole (BH), on the leading edge, and a white hole (WH) on the trailing edge. Indeed light approaching from behind the trailing edge of a perturbation (with

$v \lesssim c/n_0$) will reach the DP and consequently slowed down by the higher refractive index or, equivalently, by the faster space flow. The pulse will then be blocked at the point z_{WH} for which $v = c/(n_0 + \delta n_{\text{WH}})$. In our optical analogue model we will always considered this time-reversed version of a black hole horizon, i.e. the analogue of a *white hole horizon*. We moreover proposed an alternative approach for generating controllable DPs in Kerr media, namely ultrashort laser pulse filamentation (see Sec. 1.3), that we use in the experiments presented in Section 6.3.

6.1.1 Dielectric metrics and white hole horizons

In the dielectric analogue context, the relevant metric is the Gordon metric [100] that has been derived in detail in [101, 102] by Cacciatori, Belgiorno and co-workers and is associated with the eikonal (“plane-wave”) approximation of the field Equation (1.11). Here we recall that the metric in the laboratory frame can be written as [101]:

$$g_{\mu\nu} = \text{diag}\left(\frac{c^2}{n^2}, -1, -1, -1\right), \quad (6.2)$$

where $n \cong \sqrt{1 + \chi^{(1)} + \chi^{(3)}|E|^2}$ is the effective medium refractive index, accounting also for the nonlinear Kerr term. The two-dimensional (one spatial dimension + time) version of this metric is obtained by neglecting any dependence on the transverse (x, y) coordinates with respect to the DP propagation direction, z and reads,

$$ds^2 = \frac{c^2}{[n(z - vt)]^2} dt^2 - dz^2. \quad (6.3)$$

where the DP is induced by the laser pulse on top of a uniform background refractive index, n_0 , and is travelling along the z direction with velocity v :

$$n(z - vt) = n_0 + \delta n(z - vt), \quad \text{being} \quad \delta n(z - vt) = n_2 I(z - vt).$$

For simplicity, the perturbation δn is considered smooth and with a Gaussian profile. We then pass from the laboratory frame to the pulse (perturbation) comoving frame by means of a boost,

$$\begin{aligned} t' &= \gamma\left(t - \frac{v}{c^2}z\right), \\ z' &= \gamma(z - vt), \end{aligned}$$

being $\gamma = 1/\sqrt{1 - (v/c)^2}$, so that Eq. (6.3) becomes,

$$ds^2 = \gamma^2 \frac{c^2}{n^2} \left[1 - \left(\frac{nv}{c} \right)^2 \right] dt'^2 + 2\gamma^2 \frac{v}{n^2} (1 - n^2) dt' dz' - \gamma^2 \left[1 - \left(\frac{v}{nc} \right)^2 \right] dz'^2, \quad (6.4)$$

where primed coordinates indicate comoving coordinates. There is an *ergosurface* defined by $g_{00} = 0$, i.e. for $1 - nv/c = 0$, which corresponds to an *horizon* in the 1D+1 case [102], and exists when

$$\frac{c}{n_0 + \delta n} < v < \frac{c}{n_0}. \quad (6.5)$$

The external region corresponds to $z < z_{\text{WH}}$ and to $z > z_{\text{BH}}$. The leading horizon $z = z_{\text{BH}}$ is a black hole horizon, whereas the trailing one $z = z_{\text{WH}}$ is a white hole horizon. These points are indicated also in Figure 6.1.

Although relation (6.5) was not originally derived from a dispersive theory, recent models that account also for dispersion, i.e. $n_0 = n_0(\omega)$, arrive at exactly the same equation [93]. Equation (6.5) may be read in two different ways: for a given background index and DP amplitude, only perturbations with a certain velocity will give rise to an analogue horizon. Alternatively, for a given perturbation velocity and amplitude, only those frequencies that propagate with a refractive index that satisfies Eq. (6.5) will experience the effect of the horizon. Therefore, in presence of dispersion, relation (6.5) defines a precise spectral window of frequencies for which a *phase* horizon exists.

6.1.2 A comment on the horizon condition

To avoid confusion, we briefly analyze the existence and features of different kinds of horizons that may appear in analogue models for gravity. We will first introduce the general concepts of “phase” and “group” velocity horizons and then discuss in more detail the dispersion landscapes in our experiments reported in Section 6.3. In particular we discuss the case of DPs generated by a “superluminal” Bessel filament, or by a “subluminal” spontaneous filament.

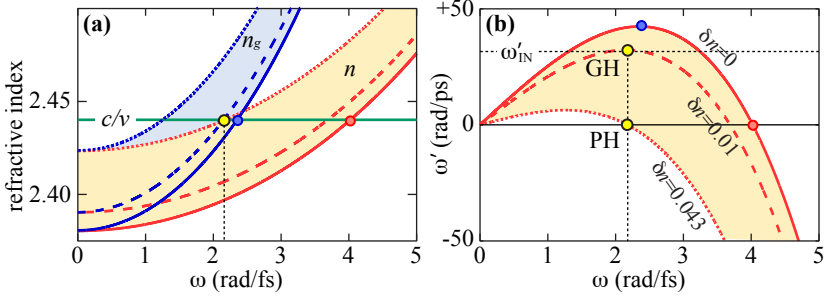


Figure 6.2: Phase and group horizon on the diamond dispersion curve: laboratory (a) and comoving frame (b), for different perturbation amplitudes, δn , as indicated in the figure. Red curves represent the refractive index, n , while blue curves represent the group index, n_g . For $\delta n = 0$ the positions of the the phase and the group horizons are indicated with red and blue circles, respectively. The frequency $\omega \cong 2.15$ rad/fs encounters a group horizon (GH) for $\delta n = 0.01$ and a phase horizon (PH) for $\delta n = 0.043$, indicated with yellow circles in (a)-(b).

- *Phase velocity horizons:* the phase velocity horizon (PH) is defined as the point within the perturbation, i.e. at δn_{PH} with $0 < \delta n_{\text{PH}} < \delta n_{\text{max}}$, at which the phase velocity is slowed down to zero in the comoving frame. The comoving phase velocity is given by $v'_\phi = \omega'/k'$, the condition $v'_\phi = 0$ means $\omega' = 0$ and hence $\omega/k = v_\phi = v$, where $k(\omega) = \omega/c(n_0 + \delta n_{\text{PH}})$;
- *Group velocity horizons:* the group velocity horizon (GH) is the point within the perturbation, i.e. at δn_{GH} with $0 < \delta n_{\text{GH}} < \delta n_{\text{max}}$, at which the group velocity, $v'_g = d\omega'/dk'$, of a wave is slowed down to zero in the comoving frame. In the laboratory frame, the group velocity thus equals the perturbation velocity, $v_g = v$. At the group horizon the incoming pulse will be completely blocked and thus this kind of horizon is also referred to as *blocking* horizon.

In normal dispersive media we have $v_g < v_\phi$ (see e.g. Fig 1.1). The consequence of this is that the same frequency will in general feel different “kinds” of horizons for different perturbation amplitudes and in particular it has $\delta n_{\text{GH}} < \delta n_{\text{PH}}$. In Figure 6.2 we exemplify this on the diamond dispersion curve (refractive index, n , in red; group index, n_g , in blue) in the laboratory (a) and comoving frame (b), for a perturbation velocity $v = 1.2286 \times 10^8$ m/s. We note that the geometry of the comoving dispersion curve changes with increasing perturbation amplitudes, from $\delta n = 0$ up to $\delta n = 0.043$, as indicated in the figure. For example, we see that the

frequency $\omega \sim 2.15$ rad/fs encounters a group horizon (GH) for $\delta n = 0.01$ and a phase horizon (PH) for $\delta n = 0.043$, where its comoving frequency is $\omega' = 0$. The two points are indicated with yellow circles in Fig. 6.2(a)-(b).

On the other hand, recalling the terminology of the *resonant scattering* model adopted in the previous Chapters, we may note that, as the comoving dispersion curve is bent down, longer and longer wavelengths (namely when both $\omega'_{\text{IN}}, \omega_{\text{IN}} \rightarrow 0$) would be blocked at the group horizon and would therefore be efficiently scattered towards blue-shifted resonant modes. In this case, far from the perturbation (asymptotic states) input and output modes would anyway lie on the same dispersion curve with $\delta n = 0$ (red solid curve). Hence, the GH condition is a condition for the *input* mode that, as approaching the perturbation, experiences an increase in the local refractive index, is consequently slowed down and, possibly, frequency-converted towards blue-shifted output modes.

“Superluminal” Bessel filament

It is also generally believed that a GH at the input frequency is strictly required in order to observe Hawking emission and mode conversion. In Figure 6.3 we show the dispersion relation for fused silica (solid curve) in the frame comoving with a DP generated by a 1055 nm carrier wavelength Bessel pulse with cone angle $\theta \sim 7^\circ$, as in the experiments described below (Section 6.3). The Bessel pulse velocity $v_B = v_g / \cos \theta \sim 2.065 \times 10^8$ is such as to predict a PH around 850 nm (at $\omega \sim 2.22$ rad/fs in the figure). The lack of an extremum in this curve implies the absence of a blocking horizon, in the sense that a light pulse approaching from $-\infty$ will never catch up with the *superluminal* DP. However, the Sellmeier relations used

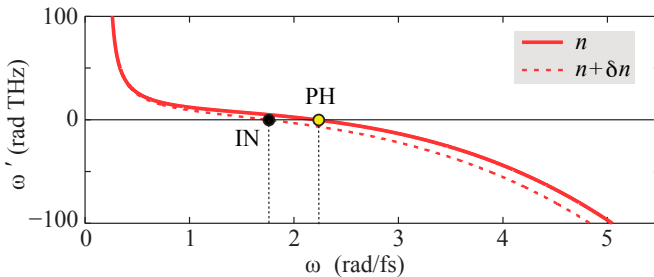


Figure 6.3: Fused silica dispersion relation in the comoving frame of a *superluminal* perturbation generated by a 7° Bessel filament. Solid curve refers to $\delta n = 0$ while dashed curve refers to $\delta n = 0.003$

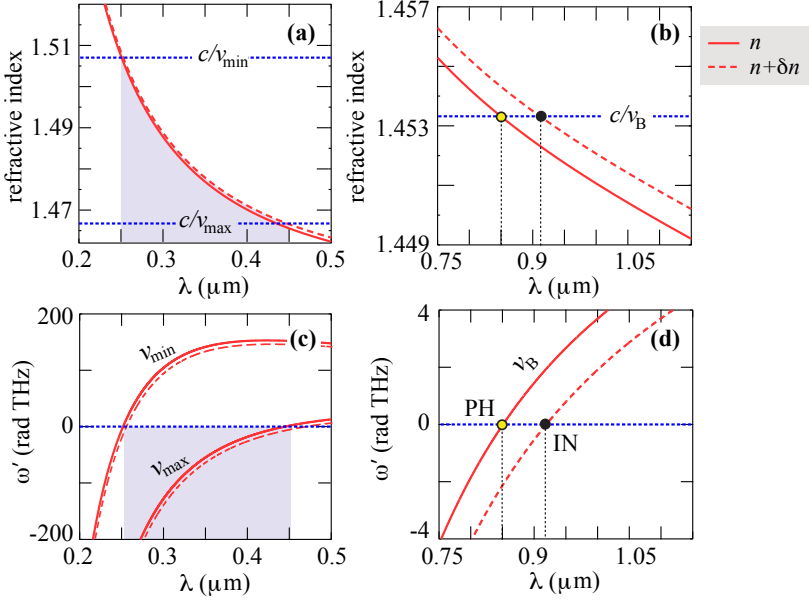


Figure 6.4: Prediction of the Hawking emission spectral range according to Eq. (6.5) for the spontaneous (a)-(c) and Bessel filament (b)-(d). The fused silica dispersion curve is plotted in the laboratory (top row) and in the comoving frame (bottom row). Solid red curves represent the background refractive index $n_0(\lambda)$, while dashed red curves represent $n_0(\lambda) + \delta n$ with $\delta n = 0.001$. Horizontal dotted lines select the points for which $n = c/v$, being v the perturbation velocity, or alternatively the points for which $\omega' = 0$.

to derive Fig. 6.3 are valid only in a limited frequency range. We can therefore imagine two different scenarios for the photon emission measured in the experiments of Fig. 6.13: either (i) the modes generated around the PH are seeded by very long wavelengths, beyond the infrared fused silica resonance ($10 \mu\text{m}$), which we may expect to encounter a group horizon; or (ii) the emission at the PH is seeded from waves propagating *inside* the perturbation and that are gradually converted at the trailing DP boundary, as they propagate with a group velocity smaller than the DP velocity ($v_g < v$, or $v'_g = d\omega'/dk' < 0$ in the comoving frame). In this case input and output modes would lie on two different dispersion curves (in Figure 6.3 red dashed and red solid curves, respectively). In Section 6.3.3 we report on linear, 1D+1 numerical simulations which confirm the possibility of this kind of mode conversion.

“Subluminal” spontaneous filament

For the case of the spontaneous filament we consider the DP induced by the trailing daughter pulse which is travelling slower with respect to the input laser pulse. Moreover, the trailing pulse develops an high intensity peak and a steep shock front (see Section 1.3). Figure 1.5 of the first Chapter shows the numerically evaluated pulse splitting dynamics for input parameters that reproduce those of the experiments presented below (Section 6.3). As shown in Fig. 1.5(b), the trailing pulse velocity varies in propagation, so that a certain range of velocity values is covered during propagation, with low velocity at the beginning of the filament and higher velocity at the end. This has the effect of broadening the emission window, which is predicted from our model (6.5) to be between 270 and 450 nm.

In Figure 6.4 we summarize the PH conditions predicted for the DP induced by the spontaneous (a)-(c) and Bessel (b)-(d) filament adopted in the experiments, as described in the caption. These predictions have to be compared with the experimental data of Figures 6.12 and 6.13, respectively.

6.1.3 Analogue Hawking temperature

From the comoving frame metric (6.4) of the dispersionless model, we may deduce the equivalent of a surface gravity at the horizon which is found to be [12]:

$$\kappa = \gamma^2 v^2 \left. \frac{dn}{dz'} \right|_{\text{PH}} \quad (6.6)$$

where $n = n_0 + \delta n$ and the DP gradient is evaluated at the phase horizon (PH), i.e.,

$$\left. \frac{dn}{dz'} \right|_{\text{PH}} = \frac{dn}{dz'}(z'_{\text{PH}}), \quad \text{with } z' = \gamma(z - vt).$$

Equation (6.6) may thus be substituted into Eq. (6.1) to obtain the actual temperature in the comoving frame, T' , for the Hawking radiation emitted from the optical analogue horizon, i.e.,

$$T' = \gamma^2 v^2 \frac{\hbar}{2\pi c k_B} \left. \frac{dn}{dz'} \right|_{\text{PH}} \quad (6.7)$$

Laser pulse induced perturbations may be extremely steep, with a rise from n_0 to $n_0 + \delta n$ over a distance of the order or $1 \mu\text{m}$ or even less. This leads to temperatures, measured in the comoving frame, that are easily of the order

of $1 - 30$ K, i.e. many orders of magnitude higher than in any other system proposed to date. The corresponding temperature, T , in the laboratory frame reads,

$$T = \frac{1}{\gamma} \frac{1}{1 - (v/c)n_0 \cos \theta} T', \quad (6.8)$$

where θ is the angle of the observation direction with respect to the propagation axis of the perturbation. The multiplicative γ factor in Eq. (6.8) is simply the Doppler shift that transforms the temperature from the co-moving to the laboratory frame. When viewed from the forward direction, $\theta = 0$ deg, the temperature measured in the laboratory frame is therefore predicted to be of the order ~ 1000 K or more [11, 12, 13].

These formulas only show that *if* Hawking radiation is emitted by the analogue horizon, then it is expected to have a certain temperature. A full quantum electrodynamical model of the moving DP accounting for the interaction with quantum vacuum, has been developed in Ref. [102]. The model starts by considering the electromagnetic vacuum state in the absence of any perturbation and then compares this with that in the presence of the travelling DP. From a physical point of view, compared to the common **S**-matrix approach of quantum field theory, the scheme does not rely on perturbation theory and is associated with linear maps, called Bogoliubov transformations, which relate the input creation and annihilation operators to the output ones. The so-called *Bogoliubov coefficients* can be used to directly evaluate the number of photons produced in such a scenario. The results clearly show a *logarithmic phase divergence* of the electromagnetic field under conditions identical to Eq. (6.5) and the spectral emission is found to follow the expected blackbody dependence, with temperature given by Eq. (6.8) [102].

In the absence of dispersion the phase divergence will be infinite and eventually leads to trans-Planckian wavelengths (the so-called “transPlanckian” problem). However, dispersion limits this divergence before unknown physical regimes are reached. Indeed, as the electromagnetic wave is blue-shifted by the phase increase at the horizon, it also slows down due to the increasing refractive index. The wave will be slowed down so much that it will be left behind the DP and eventually detaches from the horizon.

6.2 Stimulated Hawking emission and amplification

Hawking radiation is “seeded” by the vacuum state and this therefore implies that information regarding the features of the emission process may be gained by directly seeding the conversion process with a large amplitude, classical pulse. We refer to this as *stimulated Hawking emission* (SHE). Analogue systems that cannot resort to the study of quantum vacuum have successfully investigated SHE demonstrating remarkable results related to Hawking emission.

SHE is predicted to lead to mode conversion from the input (IN) wave to two output waves that have *positive* (P-mode) and *negative* (N-mode) frequencies in the comoving reference frame, exactly in the same way in which positive (RR) and negative (NRR) resonant modes are scattered by a moving DP in nonlinear Kerr media. In the optical analogue, the SHE mode conversion is thus just a different way to name the resonant shedding of light from the input pump pulse towards the blue-shifted modes [8, 7]. The condition for the output frequencies is given by imposing a conservation of the comoving frequency. Indeed, by deriving the hamiltonian for a space-time varying medium it can be demonstrated that ω' is a constant of motion [96]. The “frequency-matching” conditions are thus identical to Eqs. (3.6)-(3.7), i.e.,

$$\omega' = +\omega'_{\text{IN}}, \quad (6.9)$$

for the P-mode and

$$\omega' = -\omega'_{\text{IN}}, \quad (6.10)$$

for the N-mode. We note that the two output modes are generated at the either sides of the PH condition $\omega' = 0$, as shown in Figure 6.5 on the diamond comoving dispersion curve of Fig. 4.2(f).

The P and N modes together form the classical analogues of the Hawking pairs emitted from an horizon. The existence of these modes is a very general feature and is related only to the form of the dispersion relation and to the existence of a natural comoving frame in which frequency conservation leads to the excitation of negative frequencies. In Chapter 3 we saw that the first observation of the generation of negative-frequency waves in water was given by Rousseaux and co-workers [66] and more recently the process was shown by Weinfurtner, Unruh et al. to also exhibit

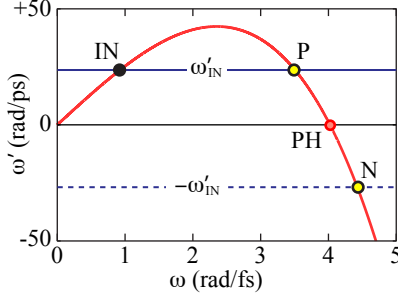


Figure 6.5: Diamond comoving dispersion curve [from Fig. 4.2(f)] with the positions of the modes, named with the terminology adopted for the SHE in the analogue gravity context, namely IN, P and N. PH indicates the position of the phase horizon, i.e. $\omega' = 0$.

a thermal-like behavior [70]. This highlights the importance of these studies. Hawking radiation in both the gravitational and analogue context is characterized by precise relations that link the norms (photon numbers, or numbers of particles in the astrophysical case) of the emitted waves to the norm of the input wave $|IN|^2$ [9, 10, 96]:

$$|P|^2 - |N|^2 = 1 \quad (6.11)$$

$$\frac{|N|^2}{|P|^2} = e^{-\alpha\omega'}, \quad (6.12)$$

where $|P|^2$ and $|N|^2$ are normalized to the norm of the input wave. Equation (6.11) is identical to the generalized Manley-Rowe relation derived for the scattering model Eq. (3.25) and, like that, implies

$$|P|^2 + |N|^2 > 1,$$

The Hawking effect will thus lead to amplification. Moreover (6.11) and (6.12) allow to directly evaluate the nature of the Hawking emission, also in the spontaneous regime and imply a *thermal* emission for the N mode,

$$|N|^2 = \frac{1}{e^{\alpha\omega'} - 1}, \quad (6.13)$$

where α may be linked to the blackbody temperature:

$$T' = \frac{\hbar}{\alpha k_B}, \quad (6.14)$$

where in our case the Hawking temperature is given by (6.7) and is proportional to the DP gradient evaluated at the horizon. Thermal emission

is a standard result of the Hawking emission process and is often regarded as one of its fundamental traits. However, it is important to point out that this result was originally derived without dispersion.

Gerlach gave a description of the black hole horizon in terms of a *parametric amplifier* [103]. In the absence of a probe pulse the horizon will amplify vacuum fluctuations but it will of course likewise convert and amplify any classical probe pulse that is sent onto it [95]. Parametric amplification is a well studied phenomenon in wave physics, in particular in the context of nonlinear optics. Very efficient excitation and amplification of vacuum states is achieved for example using crystals with a second order, $\chi^{(2)}$ nonlinearity [21]. The photon distribution of the radiation excited by these optical methods is also thermal. However the thermal emission obtained by standard nonlinear optical parametric processes is thermal with a *different* temperature characterizing each mode (i.e. frequency in the monochromatic limit) [104, 105]. Conversely, Hawking emission is composed of radiation that has exactly the same temperature over the whole spectrum [103, 105].

In the following Section we present 1D+1 (one spatial coordinate and time) numerical simulations of SHE, based on the numerical solution of Maxwell equations by means of a Finite-Difference-Time-Domain (FDTD) code [61]. Numerics confirm the thermal behavior for the emitted radiation with a temperature that is in close agreement with our perturbative model (6.7).

6.2.1 Numerical results: thermality

We performed numerical simulations of SHE with the aim of explicitly evaluating the ratio $\mathcal{R} = |N|^2/|P|^2$ and thus the characteristics of the spectral emission in the presence of dispersion in our system.

In Fig. 6.6 we show the result of a typical simulation example obtained with the FDTD code. We note that Fig. 6.6 describes exactly the same process shown in Fig. 4.2 for the linear “toy-model” of the resonant scattering event. The input (IN) wavelength is $4 \mu\text{m}$ and the super-Gaussian DP (2.19) is moving with velocity $v = 0.996 c$, which is slightly smaller than the group velocity of the input pulse, i.e. $v_g = c/n_g > v$. The DP steepness parameter is $m = 26$, corresponding to a rise time of 4 fs ($\sim 1.2 \mu\text{m}$). Figures 6.6(a)-(d) show the electric field evolution of the input pulse

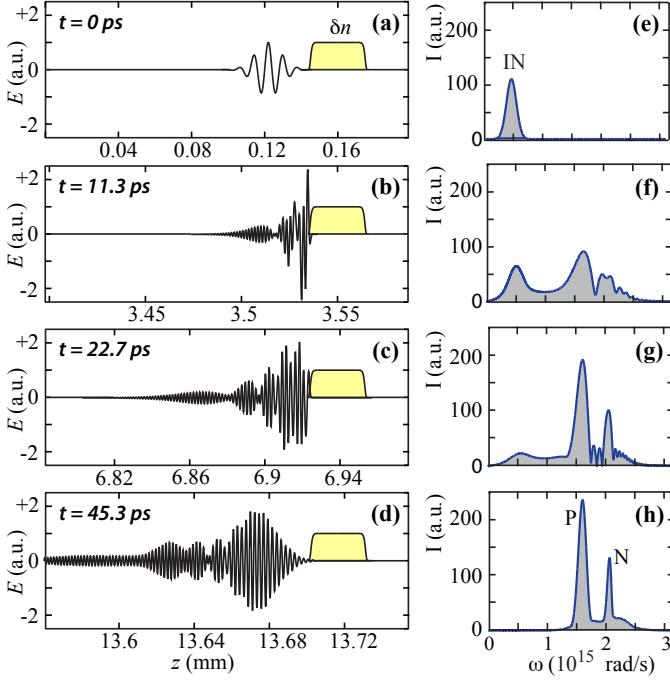


Figure 6.6: Evolution of the electric field in presence of a perturbation δn which is moving with velocity $v = 0.996 c$ (from left to right). Panels (a)-(d) show the field profile at different times, while panels (e)-(h) show the corresponding spectra. The yellow shaded area in (a)-(d) shows the DP (scaled so as to render it clearly visible). The input spectrum IN is fully converted into the blue-shifted P and N-modes.

at four different times. As it approaches the DP it is slowed down by the local increase of the refractive index until it is completely blocked at the point in which $c/v = n_g + \delta n_{\text{GH}}$, i.e., at the group horizon. This group velocity matching is essential to enhance the efficiency of the mode conversion process as the input pulse and the DP propagate at the same speed. At the end of the interaction (d)-(h), the IN mode is fully converted into the output modes (P and N) according to relations (6.9)-(6.10) and, due to dispersion, they will finally lag behind the DP. Photon numbers evolutions corresponding to the numerics of Fig. 6.6 are reported in Figure 6.7. As expected from (6.11), at the end of the interaction photon difference is conserved (red dashed curve), while photon sum is amplified (blue solid curve).

In the same way in which we have evaluated the gain $\mathcal{G} = |\text{RR}|^2 + |\text{NRR}|^2$

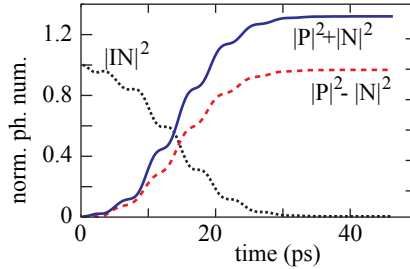


Figure 6.7: Photon number evolution normalized to the photon number at $t = 0$. Photon number in the input (IN) mode (black dotted curve), photon difference $|P|^2 - |N|^2$ (red dashed curve) and total output photons $|P|^2 + |N|^2$ (blue solid curve).

for the resonant scattering process (Section 4.4), we now want to directly evaluate the ratio $\mathcal{R} = |N|^2/|P|^2$ to demonstrate the predicted thermal behavior for the emitted radiation (6.12). Figure 6.8 shows the spectral dependence of the ratio \mathcal{R} as a function of the input comoving frequency ω'_{IN} . This set of simulations was performed with a fixed DP velocity $v = 0.97c$ and a varying input wavelength λ_{IN} , thus ensuring that the whole output spectrum experiences the same horizon and, from relation (6.7), would be amplified at the same temperature T' . We found that the blue circles in Figure 6.8 follow an exponential law with best fit (red solid curve) given by $\mathcal{R} = 0.99 \exp(-18.2 \times 10^{-14} \omega')$.

We note that for $\omega'_{\text{IN}} \rightarrow 0$, we have $\mathcal{R} \rightarrow 1$ to a very good approximation, as should be expected. This is consistent with the numerical results of Fig. 4.7 in which we found that $\mathcal{G} \rightarrow \infty$ for $\omega'_{\text{IN}} \rightarrow 0$: this means that efficiency of the emission is higher when the P and N modes approach the zero-comoving frequency (phase horizon). We may therefore expect that successful measurements of *spontaneous* analogue Hawking emission should account for this important finding and look for photon emission close to the PH condition, namely in the spectral region predicted by relation (6.5). Indeed in the absence of a narrowband IN pulse, we should consider vacuum fluctuations as a source for seeding the Hawking process: the IN state now has a “white” spectrum and high-gain spectral regions will be favored over low-gain regions. This is the rationale behind the experiments in [12, 13], presented in Section 6.3.

Moreover, from the decay constant of the exponential fit, we may estimate the Hawking temperature T' , by substituting into relation (6.14).

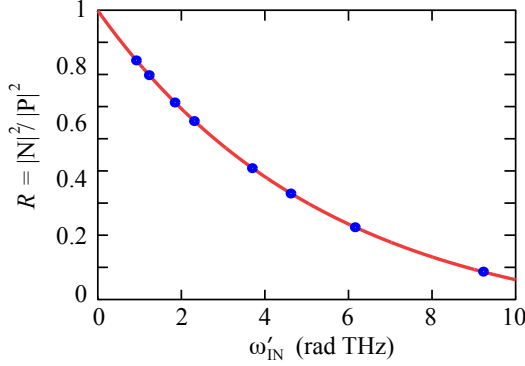


Figure 6.8: Ratio $\mathcal{R} = |N|^2/|P|^2$ versus input comoving frequency, by varying λ_{IN} between 2 and 20 μm . The numerical data (blue circles) show a clear exponential dependence with best fit (red curve) $\mathcal{R} = 0.99 \exp(-18.2 \times 10^{-14} \omega')$, corresponding to a blackbody emission with temperature $T' \sim 263$ kelvin. DP velocity $v = 0.97c$ and DP amplitude $\delta n_{\text{max}} = 0.09$.

This corresponds to a blackbody emission with temperature $T' \sim 263$ K. Impressively, this numerical evaluation results is in perfect agreement with the prediction of the perturbative model, Eq. (6.7), where the gradient of the perturbation is evaluated for a position of the horizon corresponding to $\delta n_{\text{PH}} \sim 0.032$.

What remains to study is how the Hawking temperature varies as a function of the DP amplitude so as to verify the accuracy of the perturbative model for smaller values of δn_{max} . To this end we repeat the set of simulations above to evaluate T' for different values of δn_{max} . Figure 6.9

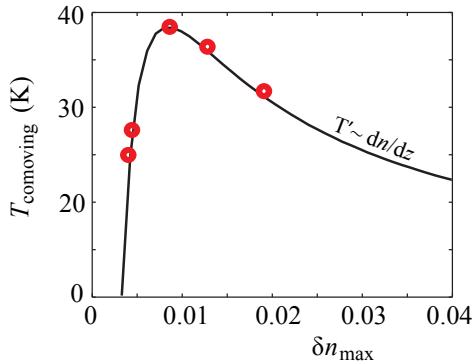


Figure 6.9: Comoving Hawking temperature dependence on DP amplitude δn_{max} . Numerical data (red circles) compared to the theoretical model (black curve) of Eq. (6.7).

shows the numerical data (red circles), retrieved by the exponential fit of the ratio \mathcal{R} versus ω'_{IN} as in Fig. 6.8, compared to the theoretical model (6.7) which is proportional to the perturbation gradient evaluated at the horizon (in this set of simulations $\delta n_{\text{PH}} \sim 0.005$). The agreement between theory and numerics is impressive. We also note that the maximum temperature is achieved for $\delta n_{\text{max}} \sim 2 \delta n_{\text{PH}}$ and for smaller DP amplitudes the temperature depends linearly on δn_{max} .

6.3 Experiments: analogue Hawking radiation

In this Section we report the experimental verification of spontaneous emission of radiation at the horizon associated with moving dielectric perturbations [12, 13]. We extended the original idea by Philbin et al. [11], who proposed to employ a soliton-induced perturbation in photonic crystal fibers, to filament-induced DP. An overview of the Kerr nonlinearity and of the ultrashort laser pulse filamentation is reported in Section 1.2, while the requirements and issues for generating a moving medium with light pulses are reported in Section 5.1.

6.3.1 Experimental setup

The experimental layout is depicted in Fig. 6.10: the input laser pulse is provided by a regeneratively amplified, 10 Hz repetition rate Nd:glass laser. The pulse duration is 1 ps and energy is varied between $\sim 50 \mu\text{J}$ and 1.2 mJ. The input pulse (carrier wavelength 1055 nm) is sent on to a 2 cm long sample of pure fused silica glass after a reshaping of the beam by means of the focusing element (lens or axicon). Indeed filaments were formed by either loosely focusing the input pulse with a 20 cm focal length lens (spontaneous filaments) or by replacing the lens with a 20° fused silica axicon so as to generate a Bessel filament with cone angle $\theta = 7^\circ$. Light emitted in the forward direction is extremely intense with an average photon number of the order 10^{15} photons/pulse. Considering that Hawking radiation is unlikely to provide more than 1 photon/pulse, a huge and extremely challenging suppression of the laser pump pulse radiation is required. The photons emitted from the sample were therefore collected at 90° rather than in the forward direction. The spectrum is then recorded

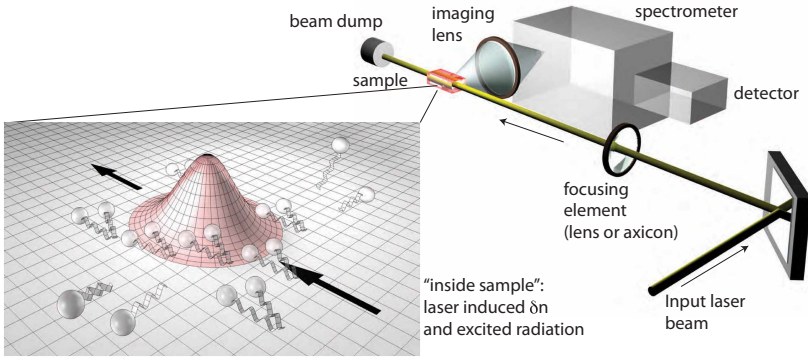


Figure 6.10: Sketch of the experimental layout. The input laser beam is focused into the Kerr sample (fused silica glass) using either a 20 cm focal length lens (to induce spontaneous filamentation) or an axicon with a 20° base angle (to create a Bessel filament). The inset shows a schematic representation of the laser induced δn : the perturbation propagates following the arrows and photon pairs, corresponding to the negative and positive Hawking pairs, are excited.

with an imaging spectrometer coupled to a 16 bit, cooled CCD camera. This arrangement was chosen in order to strongly suppress or eliminate any additional nonlinear effects (e.g. four wave mixing and self phase modulation). Moreover, by using horizontally polarized pump pulses, Rayleigh scattering is effectively suppressed so that scattered photons at wavelengths in the predicted Hawking emission range are below 0.001 photons/pulse. By employing both spontaneous and Bessel filaments in separate measurements it was possible to measure radiation emitted from DPs with various velocities.

Finally, another spurious effect that could affect any measurements of spontaneous photon emission is the presence of fluorescences from material defects. We experimentally characterized fluorescences excitation via multiphoton absorption from an infrared laser source in fused silica. Figure 6.11 shows the output spectrum at 90 degrees over the whole UV to near infrared spectral range. We identified three main contributions: R is the spontaneous Raman scattering, centered at the laser pump wavelength; F1 is the fluorescence due to non-bridging oxygen hole centers (NBOHC), while F2 is due to oxygen-deficient centers (ODC) and has a cumulative nature. These fluorescence peaks are well documented features of fused silica [106, 107]. This therefore allows us to fit the peaks with Gaussian functions (in the frequency domain) and subsequently subtract out the

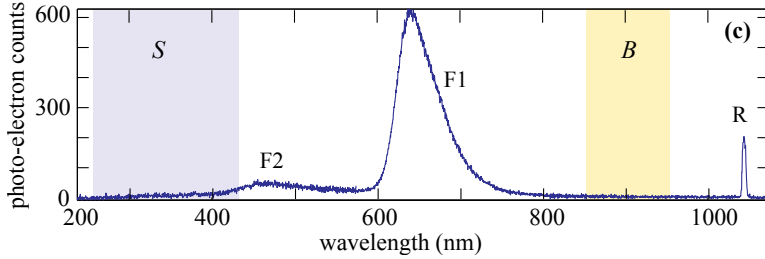


Figure 6.11: Fused silica fluorescences induced by a spontaneous filament. R denotes Raman scattering from the 1055 nm pump pulse; F1 and F2 are denote fluorescence peaks at 650 and 470 nm. Shaded areas indicate the expected spectral emission from the spontaneous (S) and Bessel (B) filaments.

fluorescence signals, thus leading to greatly improved contrast and cleaner spectra. The shaded areas in Fig. 6.11 highlight the spectral regions in which we expect to observe the analogue Hawking radiation as summarized in Figure 6.4: i.e., around ~ 350 nm for the spontaneous filament and at ~ 850 nm for the Bessel filament. Notice that we intentionally tune the Bessel velocity $v_B = v_g / \cos \theta \sim 2.065 \times 10^8$ m/s so as to excite Hawking-like radiation in a spectral region which is free from fluorescences.

6.3.2 Experimental results

The results for the spontaneous filament, adapted from Refs. [12, 13], are shown in Figure 6.12. In particular, Fig. 6.12(a) shows the full spectrum (black curve), integrated over 3600 laser shots, obtained by keeping the input slit of the spectrometer fully open, in order to collect photons emitted from the whole filament. The filament, imaged at 90° , is shown in Fig. 6.12(b). The colored areas in 6.12(a) indicate spectra measured for two different positions of the imaging spectrometer input slit, i.e. when collecting light from either the i)-*beginning*, or the ii)-*end* region of the filament, highlighted also in (b) by the vertical lines. The measured spectrum agrees well with the predicted emission region that is indicated by the shaded region in Figure 6.4(a)-(c). Remarkably, different sections of the filament emit only at selected portions of the overall spectrum, and this peculiar behavior is in quantitative agreement with the predictions (6.5).

Figure 6.13 shows the results for the Bessel filament. In this case there is no spread of the perturbation velocity and it was possible to probe the emis-

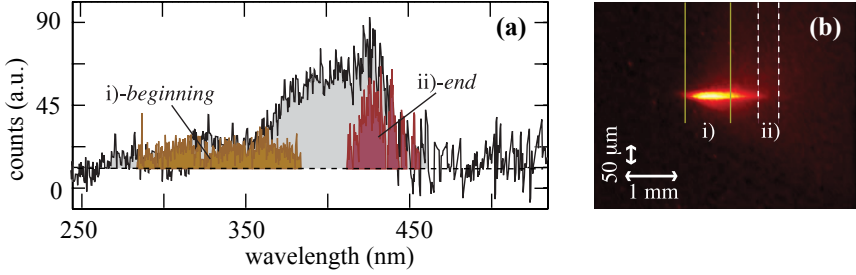


Figure 6.12: Spectra generated by the spontaneous filament (a) and image of the filament from the side, at 90° (b). The colored areas in (a) indicate spectra measured for two different positions of the imaging spectrometer input slit, i.e., i)-*beginning* and ii)-*end* section of the filament, highlighted also in (b) by the vertical lines. The black curve in (a) shows the spectrum measured with the input slit fully open.

sion for increasing peak intensities, i.e. increasing δn amplitudes, which produce higher DP gradients and consequently, higher Hawking temperatures, Eq.(6.8). The bandwidth of the emitted radiation increases with intensity and increases predominantly to longer wavelengths. This is precisely in agreement, also at a quantitative level with Eq. (6.5).

On the basis of these results, these measurements have been proposed as the first experimental evidence of Hawking-like emission from an analogue horizon [12, 13]. However, this is not generally considered to be conclusive

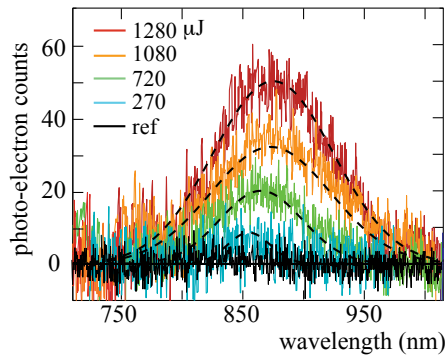


Figure 6.13: Spectra generated by the Bessel filament. Five different curves are shown corresponding to a reference spectrum obtained with a Gaussian pulse (black line) and indicated Bessel energies (in μJ). Dashed lines are guides for the eye.

evidence and further measurements are called for in order to verify some open issues: the measured photon numbers, of the order of 0.1 – 0.01 photons/pulse appear to be too high to be accounted for on the basis of a blackbody emission. Yet other models [93] appear to give predictions that confirm the measurements. Moreover, the theory predicts that photons will be generated in correlated pairs. The photons collected at 90 degrees are likely to have suffered strong scattering after emission in the forward direction and it will therefore be very unlikely to observe any kind of pair-correlation with such a setup. Other experimental layouts, e.g. based on fibers which will confine the photon pairs along the same direction, are therefore required.

6.3.3 “Superluminal” dispersion: numerics

As a conclusive remark, in this Section we try to better understand the origin of the photon emission in the case of the *superluminal* DP generated by the Bessel filament (Fig. 6.13). In Section 6.1.2 (and precisely in Figure 6.3) we proposed a *naïve* interpretation based on the possibility that the PH frequencies were excited by input vacuum modes propagating inside the dielectric perturbation. During the mode conversion process, energy is transferred from the IN mode, which lies on the dispersion curve with $\delta n = \delta n_{max}$, towards the output zero-frequency mode, which lies on the background dispersion curve (with $\delta n = 0$).

In the spontaneous Hawking radiation, the emission at the horizon PH is seeded by the vacuum state which has a broadband (white) spectrum, we therefore numerically study the mode conversion for classical, narrowband, input pulses having different carrier wavelengths centered around the zero comoving frequency. In Figure 6.14 we show the comoving fused silica dispersion curve for the numerics of Fig. 6.15. The perturbation velocity is close to the experimental value, namely $v = 2.064 \times 10^8$ m/s. We estimate the theoretical positions of the output (P and N) modes for three different input wavelengths around the zero comoving frequency (points A, B, C) as indicated in the caption. Notice that the IN modes lie on the dispersion curve with $n = n_0 + 0.08$.

Figure 6.15 show the numerical results (envelope and spectra) for a linear, super-Gaussian DP having amplitude $\delta n_{max} = 0.08$ and input wavelengths given by points A, B and C: i.e., 2.8 μm (a)-(b), 1.501 μm (c)-(d)

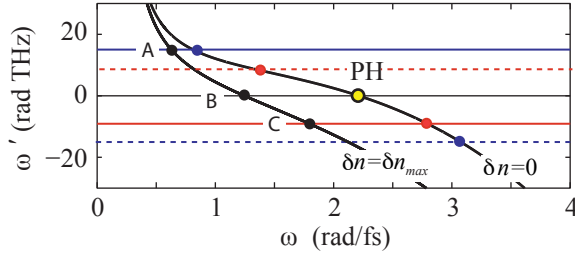


Figure 6.14: Prediction of the modes position on the fused silica dispersion curve in the frame comoving with the superluminal DP ($v = 2.064 \times 10^8$ m/s). Points A, B, and C (black circles) refer to $\lambda_{\text{IN}} = 2.8, 1.51$ and $1 \mu\text{m}$, respectively. The IN modes lie on the dispersion curve having $n = n_0 + \delta n_{\text{max}}$, with $\delta n_{\text{max}} = 0.08$, while output modes lie on the background dispersion curve ($\delta n = 0$).

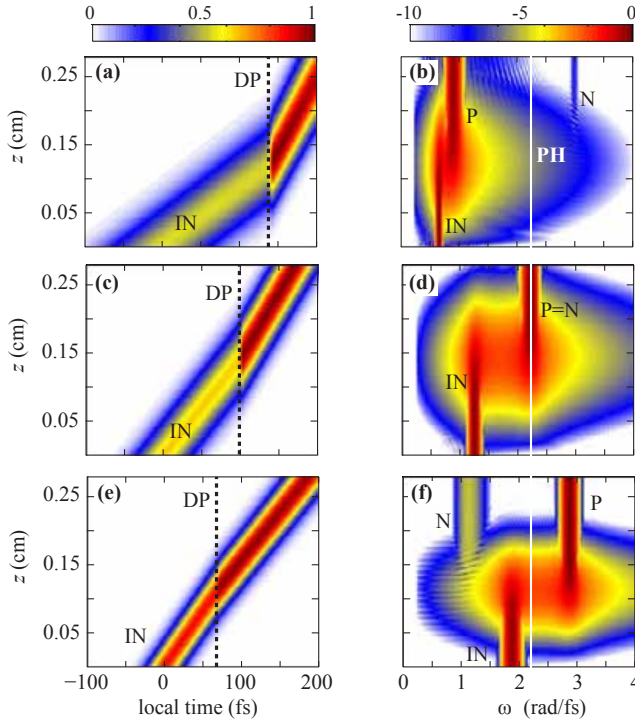


Figure 6.15: Linear 1D+1 numerics for the superluminal dispersion scenario of Fig. 6.14. Envelope (left-hand side) and spectral (right-hand side) evolution along propagation for three input wavelengths λ_{IN} around the zero-frequency condition: $2.8 \mu\text{m}$ (a)-(b), $1.501 \mu\text{m}$ (c)-(d) and $1 \mu\text{m}$ (e)-(f). The vertical white solid line on the right indicates the position of the PH (yellow circle in Fig. 6.14).

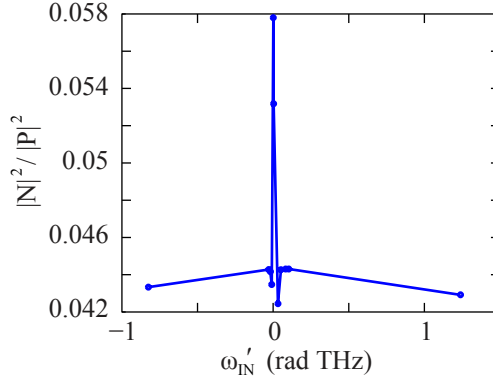


Figure 6.16: Ratio $\mathcal{R} = |N|^2/|P|^2$ versus input comoving frequency, by varying λ_{IN} around $\sim 1.501 \mu\text{m}$ which corresponds to the zero comoving frequency as in Fig. 6.15. Figure courtesy of N. Westerberg.

and $1 \mu\text{m}$ (e)-(f), respectively. At the beginning of the interaction the input mode is “under” the DP [whose trailing boundary is indicated by the vertical black dotted lines in Fig. 6.15(a)-(c)-(e)] and during propagation it gradually slides out having group velocity $v_g < v$. At the boundary it scatters towards the predicted P and N modes. We note that passing from the input condition $\omega'_{\text{IN}} > 0$ (a)-(b), to $\omega'_{\text{IN}} < 0$ (e)-(f), the P and N modes exchange positions and are indistinguishable exactly when seeded at the PH, $\omega'_{\text{IN}} = 0$ (c)-(d).

Finally, in Figure 6.16 we verify that the ratio $\mathcal{R} = |N|^2/|P|^2$ between the photon numbers in the N and P mode, Eq. (6.12), develops a divergence for $\omega' \rightarrow 0$ as already found for the subluminal case in Fig. 6.8. More importantly, in this case we found that the divergence exists also when approaching the condition $\omega' = 0$ from negative frequencies, i.e.,

$$\lim_{\omega' \rightarrow 0^\pm} \mathcal{R} = 1. \quad (6.15)$$

This thus further corroborates the interpretation presented so far, according to which spontaneous Hawking-like emission may more likely be detected close to the region of maximum gain, i.e. close to the PH condition.

These results are part of a work not yet completed and numerical studies in this direction are still in progress. We recall that, strictly speaking, a “group” horizon does not exist in the superluminal case. Therefore, it is still an open question whether this can be called Hawking radiation or

not. Nevertheless, these preliminary studies have provided a secondary, yet surprising, outcome: contrary to the subluminal case, here a blocking horizon is not really required in order to have full (100%) conversion from the input to the output modes.

Chapter 7

Conclusions

Laser pulses have been demonstrated in a variety of settings to generate analogue white holes and horizons that transform light according to the predictions of models that are derived within the context of general relativity. On the other hand, analogies between black hole kinematics and flowing media are extending the limits of our understanding across various disciplines, e.g. waves in fluids, acoustics and optics. In this thesis we have reported on experimental evidence of Hawking-like emission at the analogue of a white hole horizon, induced by a moving perturbation of the refractive index (DP) [12, 13]. The spontaneous photon emission is found to be in quantitative agreement with the Hawking model, although there is an ongoing discussion regarding the precise origin of the emission, especially for the superluminal Bessel filament case [87, 88, 89]. Here we provided also a *naive* interpretation for the superluminal dispersion landscape, corroborated by preliminary one-dimensional numerical results. We moreover numerically verify important theoretical predictions such as mode conversion from positive to negative-frequencies wave and thermality of the stimulated Hawking emission (SHE) with a temperature which is in close agreement with our perturbative model.

From a purely optical point of view, we have shown that phenomena arising from the curved space-time metric induced by the moving DP may as well be interpreted as linear scattering events within the context of the “revisited” first Born approximation. We indeed extended the theory in order to include the possibility of scattering also on the negative-frequency branch of the material dispersion relation. This powerful tool allows us

to directly predict the existence of the so-called negative-frequency resonant radiation (NRR) alongside the usual RR peak, which is well known in literature to arise from the soliton resonant shedding of light towards the blue-shifted normal GVD spectral region. Moreover, we found that coupling among positive and negative frequencies leads to amplification (at the expense of the DP) of the output photon numbers, as predicted in the analogue context for the norms of the positive (P) and negative (N) modes, i.e.,

$$|P|^2 - |N|^2 = 1 \quad \Rightarrow \quad |P|^2 + |N|^2 > 1.$$

In the optical context, this has been mathematically derived from a Manley-Rowe relation, generalized to the case of a moving DP,

$$|\text{RR}|^2 - |\text{NRR}|^2 = 1 \quad \Rightarrow \quad |\text{RR}|^2 + |\text{NRR}|^2 > 1.$$

In the thesis we have reported on experimental [8] and numerical [7] verification of NRR generation and photon number amplification. Moreover, in close analogy with the gravitational context, we numerically found that maximum gain is achieved close to the zero comoving frequency, i.e. at the phase horizon:

$$|\text{RR}|^2 + |\text{NRR}|^2 \rightarrow \infty \quad \text{for} \quad \omega' \rightarrow 0.$$

For this reason, we reported also on the first experimental evidence of resonant radiation seeded at the horizon by a long-wavelength THz probe pulse.

Although the optical analogue is still in its infancy, technologies which require the presence of an horizon have already been proposed. For example, Demircan et al. have recently studied an optical transistor that acts through a soliton-induced event horizon [108]. Moreover, the resonant scattering mediated by a soliton-induced DP [7], or the stimulated Hawking mode conversion [13] presented here, represents a novel kind of optical *amplifier* which is still awaiting a conclusive experimental demonstration. Such an amplification mechanism could in turn lead to the first “black hole laser”: a wave is trapped between two horizons that form a cavity and at each reflection from the white hole horizon light is amplified through a stimulated Hawking process with a resulting laser-like behavior [63].

Appendix A

Publications and conferences

A.1 Publications

1. Book chapter: **Laser pulse analogues for gravity**. Book title: *Analogue Gravity*, in publication (Canopus-Springer).
2. M. Clerici, L. Caspani, E. Rubino, M. Peccianti, M. Cassataro, A. Busacca, T. Ozaki, D. Faccio, R. Morandotti, **Counter-propagating frequency mixing with Terahertz waves in diamond**, *Opt. Lett.* 38, 178–180 (2013).
3. E. Rubino, A. Lotti, F. Belgiorno, S.L. Cacciatori, A. Couairon, U. Leonhardt, D. Faccio, **Soliton-induced relativistic-scattering and amplification**, *Scient. Rep.* 2, 932 (2012).
4. D. Faccio, G. Tamosauskas, E. Rubino, J. Darginavicius, D.G. Papazoglou, S. Tzortzakis, A. Couairon, A. Dubietis, **Cavitation dynamics and directional microbubble ejection induced by intense femtosecond laser pulses in liquids**, *Phys. Rev. E* 86, 036304 (2012).
5. E. Rubino, J. McLenaghan, S.C. Kehr, F. Belgiorno, D. Townsend, S. Rohr, C.E. Kuklewicz, U. Leonhardt, F. König, D. Faccio, **Negative frequency resonant radiation**. *Phys. Rev. Lett.* 108, 253901 (2012).
6. D. Faccio, E. Rubino, A. Lotti, A. Couairon, A. Dubietis, G. Tamosauskas, D.G. Papazoglou, S. Tzortzakis, **Nonlinear light-matter interaction with femtosecond high-angle Bessel beams**, *Phys. Rev. A* 85, 033829

- (2012).
7. R. Bowman, V. D'Ambrosio, E. Rubino, O. Jedrkiewicz, P. Di Trapani, and M.J. Padgett, **Optimisation of a low cost SLM for diffraction efficiency and ghost order suppression**, *Eur. Phys. J. Special Topics* 199, 149-158 (2011).
 8. E. Rubino, F. Belgiorno, S.L. Cacciatori, M. Clerici, V. Gorini, G. Ortenzi, L. Rizzi, V.G. Sala, M. Kolesik and D. Faccio, **Experimental evidence of analogue Hawking radiation from ultrashort laser pulse filaments**, *New J. Phys.* 13, 085005 (2011).
 9. G. Valiulis, V. Jukna, O. Jedrkiewicz, M. Clerici, E. Rubino and P. Di Trapani, **Propagation dynamics and X-pulse formation in phase-mismatched second-harmonic generation**, *Phys. Rev. A* 83, 043834 (2011).
 10. E. Rubino, J. Darginavičius, D. Faccio, P. Di Trapani, A. Piskarskas and A. Dubietis, **Generation of broadly tunable sub-30-fs infrared pulses by four-wave optical parametric amplification**, *Opt. Lett.* 36, 382 (2011).
 11. D. Faccio, F. Belgiorno, S.L. Cacciatori, M. Clerici, V. Gorini, G. Ortenzi, L. Rizzi, E. Rubino, V.G. Sala, **Analogue gravity and ultrashort laser pulse filamentation**, *Proc. SPIE* 7728, Nonlinear Optics and Applications IV, 77280M (June 04, 2010).
 12. F. Belgiorno, S.L. Cacciatori, M. Clerici, V. Gorini, G. Ortenzi, L. Rizzi, E. Rubino, V.G. Sala and D. Faccio, **Hawking Radiation from Ultrashort Laser Pulse Filaments**, *Phys. Rev. Lett.* 105, 203901 (2010).
 13. M. Clerici, D. Faccio, E. Rubino, A. Lotti, A. Couairon and P. Di Trapani, **Space-time focusing of Bessel-like pulses**, *Opt. Lett.* 35, 3267 (2010).
 14. E. Rubino, D. Faccio, L. Tartara, P.K. Bates, O. Chalus, M. Clerici, F. Bonaretti, J. Biegert and P. Di Trapani, **Spatiotemporal amplitude and phase retrieval of space-time coupled ultrashort pulses using the Shackled-FROG technique**, *Opt. Lett.* 34, 3854 (2009).
 15. M. Clerici, O. Jedrkiewicz, E. Rubino and P. Di Trapani, **Generation and control of phase-locked conical wavepackets in type I seeded optical parametric amplification**, *Phys. Rev. A* 80, 033813 (2009).

16. M. Clerici, O. Jedrkiewicz, E. Rubino, D. Faccio, L. Tartara, V. Degiorgio, P. Di Trapani, **Generation and amplification of pulsed Bessel beams by seeding an optical parametric amplifier**, *Opt. Lett.*, 33, 2296 (2008).
17. M. Clerici, D. Faccio, A. Lotti, E. Rubino, O. Jedrkiewicz, J. Biegert and P. Di Trapani, **Finite-energy, accelerating Bessel pulses**, *Opt. Express*. 16, 19807 (2008).
18. A. Averchi, D. Faccio, E. Rubino, H. Valtna Lukner, P. Panagiotopoulos, P. A. Loukakos, S. Tzortzakis, A. Couairon and P. Di Trapani, **Linear X-wave generation by means of Cross Phase Modulation in Kerr media**, *Opt. Lett.* 33, 3028 (2008).

A.2 Contributions at international conferences

1. E. Rubino, D. Faccio, S.L. Cacciatori, F. Belgiorno, G. Ortenzi, V. Gorini, **Laser-pulse induced event horizons and Hawking emission**, *Italian Physical Society XCVII National Congress*, L'Aquila, 26-30 September 2011 - INVITED.
2. E. Rubino, F. Belgiorno, S. Cacciatori, G. Ortenzi, L. Rizzi, V. Gorini, V.G. Sala, M. Clerici, D. Faccio, **Hawking emission from horizons in the laboratory**, *SIGRAV School, IX Edition on Analogue Gravity*, Villa Olmo, Como, 16-21 May 2011 - INVITED.
3. D. Faccio, S. Cacciatori, F. Belgiorno, G. Ortenzi, V.G. Sala, V. Gorini, M. Clerici, L. Rizzi, E. Rubino, **Curved space-time geometries in ultrashort Laser pulse Filaments and excitation of Hawking Radiation**, *COFIL 2010 - 3rd international symposium on filamentation*, 31 may-05 june 2010, Crete - INVITED.
4. D. Faccio, F. Belgiorno, S. Cacciatori, M. Clerici, V. Gorini, G. Ortenzi, L. Rizzi, E. Rubino, V.G. Sala, **Analogue gravity and ultrashort laser pulse filamentation: from Hawking radiation to the dynamical Casimir effect**, *SPIE Photonics Europe*, Brussels, 12-16 April 2010 - INVITED.
5. M. Clerici, O. Jedrkiewicz, D. Faccio, A. Averchi, A. Lotti, E. Rubino, G. Valiulis, L. Tartara, V. Degiorgio, A. Couairon, M. Kolesik, P. Di Trapani, **Controlled X wave formation in bulk quadratic and cubic nonlinear media**, *IEEE LEOS annual meeting'08*, California, USA (November 2008) - INVITED.

6. M. Clerici, O. Jedrkiewicz, E. Rubino, L. Tartara, D. Faccio, V. Degiorgio, P. Di Trapani, **Spatiotemporal pulse shaping via seeded optical parametric amplification**, *EOS annual meeting'08*, Paris, France (October 2008).

List of Figures

1	Different visions for the resonant transfer of energy mediated by a moving perturbation in dielectric media.	2
1.1	Schematic representation of phase and group velocity.	6
1.2	Optical pulse dispersion: numerical simulation.	7
1.3	Sellmeier dispersion curve for SiO ₂ (silica) glass	10
1.4	Refractive index, n , and group index, n_g , for SiO ₂ and diamond.	10
1.5	Pulse-splitting: numerics.	18
1.6	Self-steepening: numerics.	19
1.7	Conical emission.	20
1.8	Farfield (θ, λ) spectra from filamentation regimes.	22
1.9	Numerics: 1D propagation of a sech ² -soliton.	23
1.10	Numerics: Soliton and dispersive wave at the ZDW.	25
2.1	Resonant radiation emitted at the “Cherenkov angle”.	29
2.2	Scattering in the first Born approximation.	31
3.1	Negative-frequency waves in water.	38
3.2	Negative frequencies in a type-I seeded OPA process.	39
3.3	Dispersion curves in the laboratory and in the comoving frame.	41
3.4	Dispersion curves and RR phase-matching condition.	42
3.5	Numerically evaluated phase-fronts of the RR and NRR modes.	44
4.1	Schematic representation of scattering from a DP.	50
4.2	Scattering from a “toy-model” DP in diamond.	52
4.3	Soliton-induced scattering dynamics in fused silica.	55
4.4	Weak probe scattering in fused silica, from the soliton-induced DP.	56
4.5	2D numerics of linear scattering from a spatially localized DP.	57
4.6	Dispersion and output spectra for increasing input wavelengths.	59

4.7	Gain versus comoving input frequency.	59
5.1	How to generate a moving DP	62
5.2	Bessel beam.	64
5.3	Measured refractive-index variations: real and imaginary part. . .	65
5.4	Experimental setup for NRR generation in CaF_2	66
5.5	Experimental results for NRR generation in bulk CaF_2	68
5.6	NRR generation in CaF_2 and comparison with numerics.	69
5.7	Near-field and far-field spectra of Bessel pump and RR in CaF_2 . .	70
5.8	Resonant radiation X-wave fit.	71
5.9	Experimental results for NRR generation in a PCF.	73
5.10	Diamond comoving dispersion curves.	74
5.11	Sketch for the THz seeding for NRR generation in diamond.	75
5.12	RR spectrum in diamond seeded by THz radiation.	76
5.13	Spectrogram and RR polarization.	77
5.14	Sketch for the configuration adopted in the linear numerics.	77
5.15	Linear numerics for pump-probe scattering in diamond.	78
6.1	The “flowing river” of space.	84
6.2	Phase and group horizon on the diamond dispersion curve.	87
6.3	Fused silica dispersion relation a superluminal DP.	88
6.4	Prediction of the Hawking emission spectral range in fused silica. .	89
6.5	IN, P and N modes on the comoving dispersion curve.	93
6.6	Electric field and spectrum in presence of a moving DP.	95
6.7	Photon number evolution.	96
6.8	Ratio $\mathcal{R} = N ^2/ P ^2$ versus input comoving frequency.	97
6.9	Comoving Hawking temperature dependence on DP amplitude. . .	97
6.10	Experimental layout for detection of the analogue Hawking radiation.	99
6.11	Fused silica fluorescences induced by a spontaneous filament. . . .	100
6.12	Spectra generated by the spontaneous filament.	101
6.13	Spectra generated by the Bessel filament.	101
6.14	Prediction of the modes position for the superluminal case.	103
6.15	Linear 1D+1 numerics for the superluminal dispersion scenario. . .	103
6.16	Ratio $\mathcal{R} = N ^2/ P ^2$ for the superluminal case.	104

List of Tables

1.1	Sellmeier coefficients for various materials.	9
1.2	Nonlinear Kerr coefficient, n_2 , for various materials.	12

References

- [1] J.T. Mendonça, **Theory of photon acceleration**, Series in Plasma Physics, Institute of Physics, Bristol, 2001. Cited on page 1.
- [2] N.N. Rosanov, **Radiation Reflection from Inhomogeneities Moving in a Medium with a Plasma Dispersion Law**, *Opt. Spectr.* **106**, 742–747, 2009. Cited on page 1.
- [3] R.L. Savage, C. Joshi, and W.B. Mori, **Frequency upconversion of electromagnetic radiation upon transmission into an ionization front**, *Phys. Rev. Lett.* **68**, 946–949, 1992. Cited on page 1.
- [4] Z. Gaburro, M. Ghulinyan, F. Riboli, L. Pavesi, A. Recati, and I. Carusotto, **Photon energy lifter**, *Opt. Express* **14**, 7270–7278, 2006. Cited on page 1.
- [5] S.F. Preble, Q. Xu, and M. Lipson, **Changing the colour of light in a silicon resonator**, *Nature Photon.* **1**, 293–296, 2007. Cited on page 1.
- [6] T. Kampfrath, D.M. Beggs, T.P. White, A. Melloni, T.F. Krauss, and L. Kuipers, **Ultrafast adiabatic manipulation of slow light in a photonic crystal**, *Phys. Rev. A* **81**, 043837, 2010. Cited on page 1.
- [7] E. Rubino, A. Lotti, F. Belgiorno, S.L. Cacciatori, A. Couairon, U. Leonhardt, and D. Faccio, **Soliton-induced relativistic-scattering and amplification.**, *Scient. Rep.* **2**, 932, January 2012. Cited on pages 1, 2, 32, 34, 37, 38, 92 and 108.
- [8] E. Rubino, J. McLenaghan, S. Kehr, F. Belgiorno, D. Townsend, S. Rohr, C. Kuklewicz, U. Leonhardt, F. König, and D. Faccio, **Negative-Frequency Resonant Radiation**, *Phys. Rev. Lett.* **108**, 1–5, June 2012. Cited on pages 1, 2, 32, 37, 38, 43, 92 and 108.
- [9] S.W. Hawking, **Black hole explosions?**, *Nature* **248**, 30–31, 1974. Cited on pages 2, 82 and 93.
- [10] S. Hawking, **Particle production by black holes**, *Comm. Math. Phys* **43**, 199–220, 1975. Cited on pages 2, 82, 83 and 93.

- [11] T.G. Philbin, C. Kuklewicz, S. Robertson, S. Hill, F. Konig, and U. Leonhardt, **Fiber-optical analog of the event horizon**, *Science* **319**, 1367, 2008. Cited on pages 2, 81, 82, 83, 84, 91 and 98.
- [12] F. Belgiorno, S. Cacciatori, M. Clerici, V. Gorini, G. Ortenzi, L. Rizzi, E. Rubino, V. Sala, and D. Faccio, **Hawking Radiation from Ultrashort Laser Pulse Filaments**, *Phys. Rev. Lett.* **105**, 1–4, November 2010. Cited on pages 2, 60, 81, 83, 90, 91, 96, 98, 100, 101 and 107.
- [13] E. Rubino, F. Belgiorno, S.L. Cacciatori, M. Clerici, V. Gorini, G. Ortenzi, L. Rizzi, V.G. Sala, M. Kolesik, and D. Faccio, **Experimental evidence of analogue Hawking radiation from ultrashort laser pulse filaments**, *New Journal of Physics* **13**, 085005, August 2011. Cited on pages 2, 35, 60, 81, 83, 91, 96, 98, 100, 101, 107 and 108.
- [14] F.A. Jenkins and H.E. White, **Fundamentals of Optics**, 4th ed., McGraw-Hill, Inc., 1981. Cited on page 6.
- [15] J. Simmons and K.S. Potter, **Optical Materials**, Electronics & Electrical, Elsevier Science, 1999. Cited on pages 7, 8 and 9.
- [16] J.C. Diels and P. Wolfgang Rudolph, **Ultrashort Laser Pulse Phenomena: Fundamentals, Techniques, and Applications on a Femtosecond Time Scale**, Optics and photonics, Acad. Press, 2006. Cited on pages 7 and 8.
- [17] Sellmeier, **Zur Erklärung der abnormen Farbenfolge im Spectrum einiger Substanzen**, *Ann. Phys.* **219**, 272–282, 1871. Cited on page 9.
- [18] I.H. Malitson, **Interspecimen comparison of the refractive index of Fused Silica**, *J. Opt. Soc. Am.* **55**, 1205–1208, 1965. Cited on page 9.
- [19] I.H. Malitson, **A redetermination of some optical properties of Calcium Fluoride**, *Applied Optics* **2**, 1103–1107, 1963. Cited on pages 9, 66 and 69.
- [20] M. Bass, C. DeCusatis, J.M. Enoch, V. Lakshminarayanan, G. Li, C. MacDonald, V.N. Mahajan, and E. Van Stryland, **Handbook of Optics, Third Edition Volume IV: Optical Properties of Materials, Nonlinear Optics, Quantum Optics (set)**, Handbook of Optics, McGraw-Hill, 2009. Cited on page 9.
- [21] R.W. Boyd, **Nonlinear Optics**, Academic Press, 3 edition, 2008. Cited on pages 11, 16, 23, 30, 39, 47, 69 and 94.
- [22] R. Adair, L.L. Chase, and S.A. Payne, **Nonlinear refractive index of optical crystals**, *Phys. Rev. B* **39**, 3337, 1989. Cited on page 12.
- [23] M.J. Weber, **Handbook of Optical Materials**, CRC Press Laser & Optical Science & Technology, CRC PressINC, 2003. Cited on page 12.

- [24] Y.P. Kim and M.H.R. Hutchinson, **Intensity-induced nonlinear effects in UV window materials**, *Appl. Phys. B* **49**, 469, 1989. Cited on page 12.
- [25] M.D. Levenson and N. Bloembergen, **Dispersion of the nonlinear optical susceptibility tensor in centrosymmetric media**, *Phys. Rev. B* **10**, 4447, 1974. Cited on page 12.
- [26] A Couairon and A Mysyrowicz, **Femtosecond filamentation in transparent media**, *Physics Reports* **441**, 47–189, 2007. Cited on pages 15, 16, 17 and 67.
- [27] F. DeMartini, C.H. Townes, Gustafson T.K., and Kelley P.L., **Self-steepening of light pulses**, *Phys. Rev.* **164**, 312–323, 1967. Cited on page 18.
- [28] S.L. Chin, **The physics and the challenge of the propagation of powerful femtosecond laser pulses in optical media**, *Phys. Can.* **60**, 273–281, 2004. Cited on page 20.
- [29] E.T.J. Nibbering, P.F. Curley, G. Grillon, B.S. Prade, M.A. Franco, F. Salin, and A. Mysyrowicz, **Conical emission from self-guided femtosecond pulses in air.**, *Opt. Lett.* **21**, 62–65, 1996. Cited on page 20.
- [30] O.G. Kosareva, V.P. Kandidov, A. Brodeur, C.Y. Chien, and S.L. Chin, **Conical emission from laser-plasma interactions in the filamentation of powerful ultrashort laser pulses in air.**, *Opt. Lett.* **22**, 1332–1334, 1997. Cited on page 20.
- [31] P. Di Trapani, G. Valiulis, a. Piskarskas, O. Jedrkiewicz, J. Trull, C. Conti, and S. Trillo, **Spontaneously Generated X-Shaped Light Bullets**, *Phys. Rev. Lett.* **91**, 093904, 2003. Cited on pages 20 and 21.
- [32] C. Conti, S. Trillo, P. Di Trapani, G. Valiulis, A. Piskarskas, O. Jedrkiewicz, and J. Trull, **Nonlinear electromagnetic X-waves.**, *Phys. Rev. Lett.* **90**, 170406, 2003. Cited on page 20.
- [33] M. Kolesik, E. Wright, and J. Moloney, **Dynamic Nonlinear X Waves for Femtosecond Pulse Propagation in Water**, *Phys. Rev. Lett.* **92**, 253901, 2004. Cited on pages 20, 21, 26 and 30.
- [34] D. Faccio, M. Porras, A. Dubietis, F. Bragheri, A. Couairon, and P. Di Trapani, **Conical emission, pulse splitting and X-wave parametric amplification in nonlinear dynamics of ultrashort light pulses.**, *Phys. Rev. Lett.* **96**, 193901, 2006. Cited on pages 20 and 21.
- [35] H. Sonajalg, M. Ratsep, and P. Saari, **Demonstration of the Bessel-X pulse propagating with strong lateral and longitudinal localization in a dispersive medium**, *Opt. Lett.* **22**, 310, 1997. Cited on page 20.
- [36] P. Saari and K. Reivelt, **Evidence of X-shaped propagation-invariant localized light waves**, *Phys. Rev. Lett.* **79**, 4135, 1997. Cited on page 20.

- [37] M. Porras, G. Valiulis, and P. Di Trapani, **Unified description of Bessel X waves with cone dispersion and tilted pulses**, *Phys. Rev. E* **68**, 016613, 2003. Cited on page 20.
- [38] H.E. Hernandez-Figueroa, M. Zamboni-Rached, and E. Recami, **Localized Waves**, Wiley-Interscience, New York, 2008. Cited on page 20.
- [39] J. Durnin, J.J. Miceli, and J.H. Eberly, **Diffraction-free beams**, *Phys. Rev. Lett.* **58**, 1499, 1987. Cited on page 20.
- [40] D. Faccio, P. Di Trapani, S. Minardi, A. Bramati, F. Bragheri, C. Liberale, V. Degiorgio, A. Dubietis, and A. Matijosius, **Far-field spectral characterization of conical emission and filamentation in Kerr media**, *J. Opt. Soc. Am. B* **22**, 862–869, 2005. Cited on page 21.
- [41] A. Lotti, **Pulse shaping and ultrashort laser pulse filamentation for applications in extreme nonlinear optics**, Ph.D. thesis, Università degli Studi dell’Insubria, 2012. Cited on page 22.
- [42] G. Agrawal, **Nonlinear Fiber Optics**, Optics and Photonics, Elsevier Science, 2001. Cited on page 22.
- [43] John M. Dudley, Goëry Genty, and Stéphane Coen, **Supercontinuum generation in photonic crystal fiber**, *Rev. Mod. Phys.* **78**, 1135–1184, Oct 2006. Cited on pages 22, 24 and 31.
- [44] J.M. Dudley and J.R. Taylor, **Supercontinuum Generation in Optical Fibers**, Cambridge books online, Cambridge University Press, 2010. Cited on pages 22 and 24.
- [45] P. K. A. Wai, C. R. Menyuk, H. H. Chen, and Y. C. Lee, **Soliton at the zero-group-dispersion wavelength of a single-model fiber**, *Opt. Lett.* **12**, 628–630, Aug 1987. Cited on page 24.
- [46] L. Tartara, I. Cristiani, and V. Degiorgio, **Blue light and infrared continuum generation by soliton fission in a microstructured fiber**, *Applied Physics B* **77**, 307–311, 2003. Cited on pages 24 and 25.
- [47] Nail Akhmediev and Magnus Karlsson, **Cherenkov radiation emitted by solitons in optical fibers**, *Phys. Rev. A* **51**, 1995. Cited on pages 24, 25, 27, 29 and 30.
- [48] a S Gouveia-Neto, M E Faldon, and J R Taylor, **Solitons in the region of the minimum group-velocity dispersion of single-mode optical fibers.**, *Optics letters* **13**, 770–2, September 1988. Cited on page 24.
- [49] D V Skryabin, F Luan, J C Knight, and P St J Russell, **Soliton self-frequency shift cancellation in photonic crystal fibers.**, *Science (New York, N. Y.)* **301**, 1705–8, 2003. Cited on page 25.
- [50] F. Biancalana, D. V. Skryabin, and a. V. Yulin, **Theory of the soliton self-frequency shift compensation by the resonant radiationin**

- photonic crystal fibers**, *Physical Review E* **70**, 016615, July 2004. Cited on page 25.
- [51] M. Kolesik, L. Tartara, and Moloney J.V., **Effective three-wave-mixing picture and first Born approximation for femtosecond supercontinua from microstructured fibers**, *Phys. Rev. A* **82**, 045802, 2010. Cited on pages 26, 27, 30, 31, 32 and 44.
- [52] M. Kolesik, E.M. Wright, and J.V. Moloney, **Interpretation of the spectrally resolved far field of femtosecond pulses propagating in bulk nonlinear dispersive media.**, *Opt. Express* **13**, 10729–41, December 2005. Cited on pages 26 and 30.
- [53] D. Faccio, A. Averchi, A. Couairon, M. Kolesik, J.V. Moloney, A. Dubietis, G. Tamosauskas, P. Polesana, A. Piskarskas, and P. Di Trapani, **Spatio-temporal reshaping and X Wave dynamics in optical filaments.**, *Optics express* **15**, 13077–95, October 2007. Cited on pages 26 and 58.
- [54] D. Faccio, A. Averchi, A. Lotti, P. Di Trapani, A. Couairon, D. Papazoglou, and S. Tzortzakis, **Ultrashort laser pulse filamentation from spontaneous X-Wave formation in air.**, *Opt. Express* **16**, 1565–70, February 2008. Cited on pages 26, 31 and 67.
- [55] D. Faccio, A. Averchi, A. Lotti, M. Kolesik, J. Moloney, A. Couairon, and P. Di Trapani, **Generation and control of extreme blueshifted continuum peaks in optical Kerr media**, *Phys. Rev. A* **78**, 033825, September 2008. Cited on pages 26 and 31.
- [56] B.M. Bolotovskii and V.L. Ginzburg, **The Vavilov-Cerenkov Effect and the Doppler Effect in the Motion of Sources with Superluminal Velocity in Vacuum**, *Physics-Uspekhì* **15**, 184–192, 1972. Cited on page 29.
- [57] P.K. Tien, R. Ulrich, and R.J. Martin, **Optical second harmonic generation in form of a coherent Cerenkov radiation from a thin-film waveguide** . Cited on page 29.
- [58] M. Kolesik, D. Faccio, E.M. Wright, P. Di Trapani, and J.V. Moloney, **Supercontinuum generation in planar glass membrane fibers: comparison with bulk media.**, *Optics letters* **34**, 286–8, February 2009. Cited on page 30.
- [59] A. V. Husakou and J. Herrmann, **Supercontinuum Generation of Higher-Order Solitons by Fission in Photonic Crystal Fibers**, *Phys. Rev. Lett.* **87**, 203901, Oct 2001. Cited on page 31.
- [60] M. Kolesik and J. V. Moloney, **Nonlinear optical pulse propagation simulation: From Maxwell’s to unidirectional equations**, *Phys. Rev. E* **70**, 036604, Sep 2004. Cited on pages 32, 33 and 49.

- [61] K. Yee, **Numerical solution of initial boundary value problems involving Maxwell's equations in isotropic media**, *IEEE Trans. Antennas Propag.* **14**, 302–307, 1966. Cited on pages 35 and 94.
- [62] J.C.A. Tyrrell, P. Kinsler, and G.H.C. New, **Pseudospectral spatial-domain: a new method for nonlinear pulse propagation in the few-cycle regime with arbitrary dispersion**, *J. Mod. Opt.* **52**, 973–986, 2005. Cited on page 35.
- [63] Daniele Faccio, Tal Arane, Marco Lamperti, and Ulf Leonhardt, **Optical black hole lasers**, *Classical and Quantum Gravity* **29**, 224009, November 2012. Cited on pages 35 and 108.
- [64] M. Born and E. Wolf, **Principles of Optics**, Cambridge University Press, Cambridge, England, 1999. Cited on page 38.
- [65] L. Mandel and E. Wolf, **Optical Coherence and Quantum Optics**, Cambridge University Press, Cambridge, England, 1995. Cited on page 38.
- [66] G. Rousseaux, C. Mathis, P. Maïssa, T. G. Philbin, and U. Leonhardt, **Observation of negative-frequency waves in a water tank: a classical analogue to the Hawking effect?**, *New Journal of Physics* **10**, 053015, May 2008. Cited on pages 38, 39, 43, 83 and 92.
- [67] O. Jedrkiewicz, M. Clerici, E. Rubino, and P. Di Trapani, **Generation and control of phase-locked conical wave packets in type-I seeded optical parametric amplification**, *Physical Review A* **80**, 033813, 2009. Cited on page 39.
- [68] N.D. Birrell and P.C.W. Davies, **Quantum fields in curved space**, Cambridge University Press, Cambridge, 1982. Cited on pages 38, 60 and 82.
- [69] R. Brout, S. Massar, R. Parentani, and Ph. Spindel, **A primer for black hole quantum physics**, *Physics Reports* **260**, 329 – 446, 1995. Cited on page 38.
- [70] Silke Weinfurtnner, Edmund W. Tedford, Matthew C. J. Penrice, William G. Unruh, and Gregory A. Lawrence, **Measurement of Stimulated Hawking Emission in an Analogue System**, *Phys. Rev. Lett.* **106**, 021302, Jan 2011. Cited on pages 39, 83 and 93.
- [71] Oren Lahav, Amir Itah, Alex Blumkin, Carmit Gordon, Shahar Rinott, Alona Zayats, and Jeff Steinhauer, **Realization of a Sonic Black Hole Analog in a Bose-Einstein Condensate**, *Phys. Rev. Lett.* **105**, 240401, Dec 2010. Cited on pages 39 and 83.
- [72] Dmitry V. Skryabin and Andrey V. Gorbach, **Colloquium: Looking at a soliton through the prism of optical supercontinuum**, *Rev. Mod. Phys.* **82**, 1287–1299, Apr 2010. Cited on page 40.

- [73] L. A. Ostrovskii, **Some general relations for waves at the moving boundary between two media**, *Soviet Phys. JETP* **34**, 293, 1972. Cited on page 47.
- [74] Yu. M. Sorokin, **Some general relations for waves at the moving boundary between two media**, *Radiophysics and Quantum Electronics* **15**, 36, 1972. Cited on page 47.
- [75] Yu. A. Kravtsov, L. A. Ostrovskii, and N. S. Stepanov, **Some general relations for waves at the moving boundary between two media**, *Proc. IEEE* **62**, 1492, 1974. Cited on page 47.
- [76] Pierre B ejot, Christophe Bonnet, V eronique Boutou, and Jean-Pierre Wolf, **Laser noise compression by filamentation at 400 nm in argon.**, *Optics express* **15**, 13295–309, October 2007. Cited on page 53.
- [77] C. Barcel o, S. Liberati, and M. Visser, **Analogue Gravity**, *Living Reviews in Relativity* **14**, 1–179, 2011. Cited on pages 60, 82 and 83.
- [78] D. Faccio, **Laser pulse analogues for gravity and analogue Hawking radiation.**, *Contemp. Phys.* **53**, 2012. Cited on page 60.
- [79] Ari T. Friberg, **Stationary-phase analysis of generalized axicons**, *J. Opt. Soc. Am. A* **13**, 743–750, Apr 1996. Cited on page 63.
- [80] D. Faccio, E. Rubino, A. Lotti, A. Couairon, A. Dubietis, G. Tamo sauskas, D. Papazoglou, and S. Tzortzakis, **Nonlinear light-matter interaction with femtosecond high-angle Bessel beams**, *Physical Review A* **85**, 1–6, March 2012. Cited on pages 64 and 65.
- [81] P. Polesana, A. Couairon, D. Faccio, A. Parola, M. A. Porras, A. Dubietis, A. Piskarskas, and P. Di Trapani, **Observation of Conical Waves in Focusing, Dispersive, and Dissipative Kerr Media**, *Phys. Rev. Lett.* **99**, 223902, Nov 2007. Cited on pages 64 and 71.
- [82] P. Polesana, A. Dubietis, M. A. Porras, E. Ku cinskas, D. Faccio, A. Couairon, and P. Di Trapani, **Near-field dynamics of ultrashort pulsed Bessel beams in media with Kerr nonlinearity**, *Phys. Rev. E* **73**, 056612, May 2006. Cited on pages 65 and 71.
- [83] M. Clerici, M. Peccianti, B.E. Schmidt, L. Caspani, M. Shalaby, M. Gigu ere, A. Lotti, A. Couairon, F. L egar e, T. Ozaki, D. Faccio, and R. Morandotti, **Scaling mechanism for efficient wavelength conversion in laser plasmas**, *ArXiv* page 1207.4754, 2012. Cited on page 74.
- [84] Matteo Clerici, Lucia Caspani, Eleonora Rubino, Marco Peccianti, Marco Cassataro, Alessandro Busacca, Tsuneyuki Ozaki, Daniele Faccio, and Roberto Morandotti, **Counterpropagating frequency mixing with terahertz waves in diamond**, *Opt. Lett.* **38**, 178–180, Jan 2013. Cited on pages 75 and 76.

- [85] U. Peschel, T. Pertsch, and F. Lederer, **Optical Bloch oscillations in waveguide arrays**, *Opt. Lett.* **23**, 1701–1703, Nov 1998. Cited on page 81.
- [86] J.D. Joannopoulos, S.G. Johnson, J.N. Winn, and R.D. Meade, **Photonic Crystals: Molding the Flow of Light**, Princeton University Press, New Jersey, ii edition, 2008. Cited on page 81.
- [87] R. Schützhold and W.G. Unruh, **Comment on “Hawking radiation from ultrashort laser pulse filaments”**, *Phys. Rev. Lett.* **107**, 149401, 2011. Cited on pages 81 and 107.
- [88] F. Belgiorno, S. Cacciatori, M. Clerici, V. Gorini, G. Ortenzi, L. Rizzi, E. Rubino, V.G. Sala, and D. Faccio, **Belgiorno et al. reply**, *Phys. Rev. Lett.* **107**, 149402, 2011. Cited on pages 81 and 107.
- [89] S. Liberati, A. Prain, and M. Visser, **Belgiorno et al. reply**, *Phys. Rev. D.* **85**, 084014, 2012. Cited on pages 81 and 107.
- [90] U. Leonhardt and T.G. Philbin, **Transformation optics and the geometry of light**, *Prog. Opt* **53**, 69–152, 2009. Cited on page 82.
- [91] R. Schützhold, **Recreating Fundamental Effects in the Laboratory?**, *Advanced Science Letters* **2**, 121–132, 2009. Cited on page 82.
- [92] V. A. De Lorenci, R. Klippert, and Yu. N. Obukhov, **Optical black holes in moving dielectrics**, *Phys. Rev. D* **68**, 061502, Sep 2003. Cited on page 82.
- [93] A. Guerreiro, A. Ferreira, and J.T. Mendonça, **Production of bright entangled photons from moving optical boundaries**, *Phys. Rev. A* **83**, 0523025, 2011. Cited on pages 82, 86 and 102.
- [94] M. Novello, M. Visser, and G. E. Volovik, **Artificial black holes**, World Scientific, 2002. Cited on page 82.
- [95] J.D. Bekenstein, **Black Holes and Entropy**, *Phys. Rev. D* **7**, 1973. Cited on pages 83 and 94.
- [96] W. G. Unruh, **Experimental black-hole evaporation?**, *Phys. Rev. Lett.* **46**, 1351–1353, 1981. Cited on pages 83, 92 and 93.
- [97] R. Balbinot, A. Fabbri, S. Fagnocchi, A. Recati, and I. Carusotto, **Nonlocal density correlations as a signature of Hawking radiation from acoustic black holes**, *Phys. Rev. A* **78**, 021603, Aug 2008. Cited on page 83.
- [98] I. Carusotto, S. Fagnocchi, A. Recati, R. Balbinot, and A. Fabbri, **Numerical observation of Hawking radiation from acoustic black holes in atomic Bose Einstein condensates**, *New J. Phys.* **10**, 103001, October 2008. Cited on page 83.

- [99] Daniele Faccio, **Laser pulse analogues for gravity and analogue Hawking radiation**, *Contemporary Physics* **53**, 37–41, 2012. Cited on pages 83 and 84.
- [100] W. Gordon, **Zur Lichtfortpflanzung nach der Relativitätstheorie**, *Annalen der Physik* **377**, 421, 1923. Cited on pages 83 and 85.
- [101] S.L. Cacciatori, F. Belgiorno, V. Gorini, G. Ortenzi, L. Rizzi, V.G. Sala, and D. Faccio, **Spacetime geometries and light trapping in travelling refractive index perturbations**, *New Journal of Physics* **12**, 095021, September 2010. Cited on page 85.
- [102] F. Belgiorno, S.L. Cacciatori, G. Ortenzi, L. Rizzi, V. Gorini, and D. Faccio, **Dielectric black holes induced by a refractive index perturbation and the Hawking effect**, *Physical Review D* **83**, 024015, January 2011. Cited on pages 85, 86 and 91.
- [103] U.H. Gerlach, **The mechanism of blackbody radiation from an incipient black hole**, *Phys. Rev. D* **14**, 1479–1508, 1976. Cited on page 94.
- [104] D.F. Walls and G.J. Milburn, **Quantum Optics**, Springer, Berlin, i edition, 1994. Cited on page 94.
- [105] U. Leonhardt, **Quantum Optics**, Cambridge University Press, Cambridge, i edition, 2010. Cited on page 94.
- [106] Arnaud Zoubir, Clara Rivero, Rachel Grodsky, Kathleen Richardson, Martin Richardson, Thierry Cardinal, and Michel Couzi, **Laser-induced defects in fused silica by femtosecond IR irradiation**, *Phys. Rev. B* **73**, 224117, Jun 2006. Cited on page 99.
- [107] Linards Skuja, **Optically active oxygen-deficiency-related centers in amorphous silicon dioxide**, *Journal of Non-Crystalline Solids* **239**, 16 – 48, 1998. Cited on page 99.
- [108] A. Demircan, Sh. Amiranashvili, and G. Steinmeyer, **Controlling Light by Light with an Optical Event Horizon**, *Phys. Rev. Lett.* **106**, 163901, 2011. Cited on page 108.

